Catalytic Properties of Nitrogen- and Oxygen-Modified Earth-Abundant Materials

Steven Robert Denny

Submitted in partial fulfillment of the
requirements for the degree of
Doctor of Philosophy
under the Executive Committee
of the Graduate School of Arts and Sciences

COLUMBIA UNIVERSITY

2021

Abstract

Catalytic Properties of Nitrogen- and Oxygen-Modified Earth-Abundant Materials

Steven Robert Denny

The replacement or loading-reduction of precious metal catalysts with low-cost, earth-abundant materials is an important step for the development of next-generation industrial chemical processes. By decreasing the potential cost of an electrolyzer device or enabling new pathways of upgrading biomass-derived oxygenates (BDOs), the nitrides and oxides of earth-abundant transition metals may be strategically utilized for the modular use of renewable power or the transition of conventional chemical feedstocks to renewable sources. This thesis uses a combination of electrochemical and surface science techniques to study the catalytic properties of nitrogen- and oxygen-modified earth-abundant materials for the electrolysis of water, and the surface reactions of three BDOs: ethanol, glycerol, and tetrahydrofurfuryl alcohol (THFA).

The development of stable, active, and low-cost electrocatalysts with reduced platinum group metal (PGM) loading for the hydrogen evolution reaction (HER) is an important step towards the grid-level implementation of electrolyzers. In this thesis, the electrochemical stability of tungsten nitride (WN) and niobium nitride (NbN) was characterized over broad pH-potential regimes, from which pseudo-Pourbaix diagrams were developed. In addition, unmodified and platinum-modified WN and NbN thin films were assessed for HER, where monolayer (ML) Pt-modification led to Pt-like HER activity in acid electrolyte.

The selective bond scission of oxygen-rich and functionally complex biomass-derived oxygenates offers a unique opportunity to convert renewable biomass, as opposed to fossil fuels,

into important industrial feedstocks. The fundamental surface reactions of three BDOs, either lignin-derived or biofuel-derived, was studied in this thesis.

Ethanol reforming was studied on unmodified and Pt-modified Mo_2N thin film surfaces for the production of synthesis gas, or syngas, a CO and H_2 gas feedstock for Fischer-Tropsch synthesis. Mo_2N, and the Mo_2C carbide analogue, have exhibited strong oxophilicity for the reaction of simple and complex alcohols that results in unselective C-O bond scission. Pt-modification was used to selectively conserve the C-O bond for CO production, and cleave the C-H and C-C bonds for H_2 generation. Pt-modification shifted the reaction pathway from undesired decomposition on Mo_2N to reforming, while inhibiting undesired pathways such as ethylene or methane production.

The hydrodeoxygenation (HDO) of glycerol, the primary manufacturing byproduct of biodiesel, to propylene was studied on WO_x-modified Pt(111) surfaces. Two WO_x active sites were observed for the deoxygenation of glycerol: Brønsted acid WO_x sites for dehydration and oxygen vacancy sites for hydrodeoxygenation (HDO). While the undesired dehydration of glycerol to acrolein was most active on surfaces with thick WO_x coverages, propylene production via the HDO pathway was more facile at intermediate coverages.

Lastly, the ring-opening of THFA, a promising biomass-derived platform oxygenate, was studied on WO_x/Pt(111) surfaces. The desired ring-opened product, 1,5-PeD, was also used as a probe molecule to study binding and desorption on WO_x/Pt(111) surfaces. This work indicates that WO_x-modification weakens the interaction between the ring-opened intermediate and the surface, to an extent that facilitates the hydrogenation of the 1,5-PeD-like intermediate and the desorption of gas-phase 1,5-PeD.

Table of Contents

List of Figures

List of Tables

List of Schemes

Acknowledgments

My New York City adventure began four years ago, when I was still living in North Carolina, the state in which I was born and raised. My first visit to the city overwhelmed me, but I knew that I had found a new temporary home. In many ways my graduate school experience was different than I had anticipated, most significantly by COVID-19 turning into COVID-21. In light of many difficult circumstances and through this experience, I have had many important mentors, colleagues, and friends that I would like to thank.

Firstly, I would like to thank my advisor Prof. Jingguang Chen for his mentorship and thoughtful feedback. Dr. Chen is an academic force of frequent publication and high impact, and I am grateful to have had the opportunity to work in his group. I would also like to thank Prof. Lauren Marbella, Prof. Daniel Esposito, Prof. Alissa Park, and Prof. Alexander Urban-Artrith for serving on my thesis committee.

I would like to thank the past and present members of the Chen Research Group, as well as visiting professors and scholars. Specifically, I would like to thank Prof. Sergey Rykov for his knowledge and assistance in maintaining the UHV equipment, as well as Dr. Nongnuch Artrith for her work and knowledge of DFT and machine learning. I would like to thank my colleagues and seniors in the group, namely Brian Tackett, Zhexi Lin, Lea Winter, Weiming Wan, Akash Neal Biswas, William Porter, Hansen Muo, Elli Wiita, Kevin Turaczy, Xiaoran Niu, Qian (Tyra) Zhang, Ji Hoon Lee, and Elaine Gomez. I've had countless wonderful conversations and interactions with group members, and I attribute to them a large part of my happiness and success in this chapter of my life. Outside of my field of research, I would like to thank Prof. Sanat Kumar, Prof. Kyle Bishop, and Prof. Faye McNeill for friendship and conversation.

For many years, CU's Department of Chemical Engineering has been my home, and I would like to extend my thanks the students, staff, and faculty. The staff play an integral role in the success of the department, and I would be remiss to not thank Kathy Marte, Rezarta Binaj, Ariel Sanchez, Emely Aquino Feliz, and Aurna Malakar. Kathy Marte in particular plays a critical role in the operation of the chemical engineering graduate organization (ChEGO), and is always quick to support events and outreach efforts. ChEGO was my social home for many years, and holds an important, well-supported role in the culture of the department.

I want to thank all of my colleagues and friends in the department for my cherished memories of times spent together, picnics in the park, remote and in-person Dungeons and Dragons, beach trips, and more. A special thanks to those friends closest with me during these years: Marissa Beatty, Ryan Gusley, Brian Tackett, Will Porter, Mateo Williams, Jon Vardner, Rob Mohr, Sara Hamilton, Anna Dorfi, Drew Ells, Jack Davis, Andrew Jiminez, Alejandro Krauskopf, Lea Winter, Zhexi Lin, Dimitri Livitiz, Robbie Tannenbaum, Dan McKeen, Nick Brady, Richard May, Neal Biswas, and many more.

A special acknowledgement goes to Mateo Williams, a close friend and brilliant researcher. His tragic loss shifted the landscape of the department and my perspective on the many things that I value in life. Unlike anyone that I've known, Mateo was a fierce proponent of having passion in all of life's pursuits. He embraced difficult conversations that changed attitudes and challenged conventional thought.

I want to thank my family for their love and support, and for providing a platform on which I was able to launch my professional ambitions. To my parents and brother, Brenda, Chuck, and Kirk, three of my most important mentors, I can't emphasize enough your role in this experience. To my extended family, that is much closer than "extended" would suggest, I've

always cherished our relationships and your support. Most of all, I would like to acknowledge Margaret Tomaszewski-Denny, my closest friend and companion. More than any other individual, Maggie has been my personal and professional rock, and has shared my highs and lows with patience and grace.

Chapter 1: Introduction

1.1 Motivation

Two of the foremost challenges that modern engineering faces are addressing the carbon footprint of the projected boom in energy consumption by the turn of the half century, and transitioning chemical feedstocks from conventional fossil fuel-derived pathways to renewable sources. In part, what the solution to each of these challenges has in common is the necessity of developing stable, active, and earth-abundant catalyst and catalyst support materials. Catalysts are critically important for industrial chemistry, so much so that the production of 75% of all chemicals, and 90% of newly developed chemical processes are catalyst-assisted.[1] Specific to the challenges discussed herein, catalysts are essential for the conversion of renewable power into chemically-stored energy, as well as the selective conversion of functionally complex biomass-derived oxygenates (BDO) into green platform chemicals.

1.2 Water Electrolysis

The Energy Information Administration (EIA) and International Energy Agency (IEA) project that the global energy demand will increase by 28% and 30%, respectively, by 2040.[2,3] As an alternative to CO_2-intensive energy sources, wind and solar renewable energy have been aggressively implemented at the grid-level. The shift away from traditional means of energy production is so ubiquitous that in 2016, 67% of new additions to the United States' net electrical capacity were attributed to renewable energy.[4] Despite this, the intermittence inherent to certain renewable technologies can lead to differences in supply and demand, which at times results in power shortages or oversupply, and necessitates energy storage technologies.[5,6] Current strategies to address this discrepancy include battery-based energy storage, where capacity is

reliant on the size of the installation, as well as curtailment.[5,6] The electrolysis of water into gas-phase hydrogen (H_2) provides an alternative solution, where installations can be modular and readily scalable for energy storage.

H_2 produced using renewable energy has many advantages over other fuel sources. H_2 has more than double the gravimetric energy density than competing fuels, including methane (CH_4), methanol (CH_3OH), gasoline, and diesel.[7] Furthermore, H_2 is a reactant in the Haber-Bosch process of ammonia (NH_3) synthesis. Ammonia production accounts for as much as 2% of global commercial energy consumption, much of which is associated with the fossil-derived hydrocarbon sourcing of H_2.[8] Conventional industrial H_2 production relies on the steam reforming of methane or other light alkanes, which results in the undesired presence of catalyst-poisoning sulfur compounds in the H_2 gas mixture, as well as 2.3 tons of CO_2 per ton of NH_3 produced.[9] Renewably powered water electrolysis has the potential to produce H_2 at-scale, in modular installations that would offset the carbon footprint associated with conventional modes of H_2 production. Prerequisite to the grid-scale adoption of this technology is the discovery and characterization of active, stable, and earth-abundant electrocatalysts for the hydrogen evolution reaction (HER).[10,11]

Water electrolysis is the water splitting electrochemical reaction that produces gas-phase oxygen via the oxygen evolution reaction (OER) at the anode, and gas-phase hydrogen via the hydrogen evolution reaction (HER) at the cathode. The overall reaction, half reactions, and standard electrode potentials (E^0) are shown in Equations 1.1 - 1.3. Water electrolysis can be conducted in both acid and alkaline electrolytes, with differing reaction kinetics for each respective electrolyte. The primary distinctions in the kinetics of acid and alkaline HER stem from disparate proton accessibility, and differences in hydrogen binding energies.[12] In alkaline

environments, the protons that recombine in the HER are sourced from the dissociation of water, a thermodynamically demanding step that is not required for proton-rich acid-electrolysis.[13,14]

Equation 1.1 $2H_2O_{(l)} \rightarrow O_{2\,(g)} + 2H_{2\,(g)}$ ΔE^0 = -1.23 V_{RHE}

Equation 1.2 $2H_2O_{(l)} + 2e^- \rightarrow 2OH^-_{(aq)} + H_{2\,(g)}$ ΔE^0 = 0 V_{RHE}

Equation 1.3 $4OH^-_{(aq)} \rightarrow O_{2\,(g)} + 2H_2O_{(l)} + 4e^-$ ΔE^0 = -1.23V_{RHE}

Historically, platinum (Pt) is the benchmark electrocatalyst for the HER in acid and alkaline electrolyte.[15, 16, 17] Platinum and other platinum group metals (PGMs) that are active for the HER demonstrate low Tafel slopes, high exchange current densities (i_0), and low overpotential losses at high current densities.[17,18] Despite this, PGMs are geologically scarce and geographically localized,[19] and strategies to reduce PGM loading or replace the material entirely with earth-abundant materials have been the focus of significant research efforts. Density functional theory (DFT) calculations of the binding energy between hydrogen and the active catalyst, as well as the change in Gibbs free energy associated with hydrogen adsorption (ΔG_H) have also been used as a screening descriptor for potential materials.

By combining DFT calculations with the exchange current density, a key parameter related to the electrochemical reaction rate, a volcano plot can be generated as an electrocatalytic application of Sabatier's principle.[17] Sabatier's principle suggests that on a thermodynamic basis, active catalysts have intermediate reactant-surface bond strengths.[20] The volcano plot demonstrates the importance of relatively moderate ΔG_H for optimally active HER catalysts in both acid and alkaline electrolytes for metals, transition metal carbides (TMCs), and metal-modified TMCs.[12,17,21] Shown in Figure 1.1, materials with the most positive log(i_0) have moderate ΔG_H, indicating that these materials are most active for the HER.[17] In the case that hydrogen atoms are too strongly bound to the catalyst surface, it is thermodynamically

unfavorable for reaction intermediates to recombine, and gaseous H_2 to desorb.[17, 20] Similarly, in the case that hydrogen atoms are weakly bound to the catalyst surface, bond instability limits local proton concentration, and causes rapid desorption.[17,20]

The stability of an electrocatalyst is also critically important. Chronopotentiometric (CP)-titration curves have been used to generate pseudo-Pourbaix diagrams for several TMCs to assess the material stability in a wide range of pH-potential regimes.[22–24] These diagrams detail regimes in which a material is immune to oxidation, undergoes surface passivation, and is bulk oxidized. This information illustrates the stability of a material in conditions relevant to several electrochemical reactions. Pseudo-Pourbaix diagrams can also serve as a secondary filter in combination with DFT calculations to identify potential candidate materials for important electrochemical reactions.[22–24] For example, in Figure 1.2(a) a pseudo-Pourbaix stability diagram for NbC has been reported in the literature.[22] In combination with DFT calculations of the oxygen binding energy, the oxidation potential can be paired as a guide for pH-potential regimes in which a material is stable for a relevant electrochemical reaction (Figure 1.2(b)).[22]

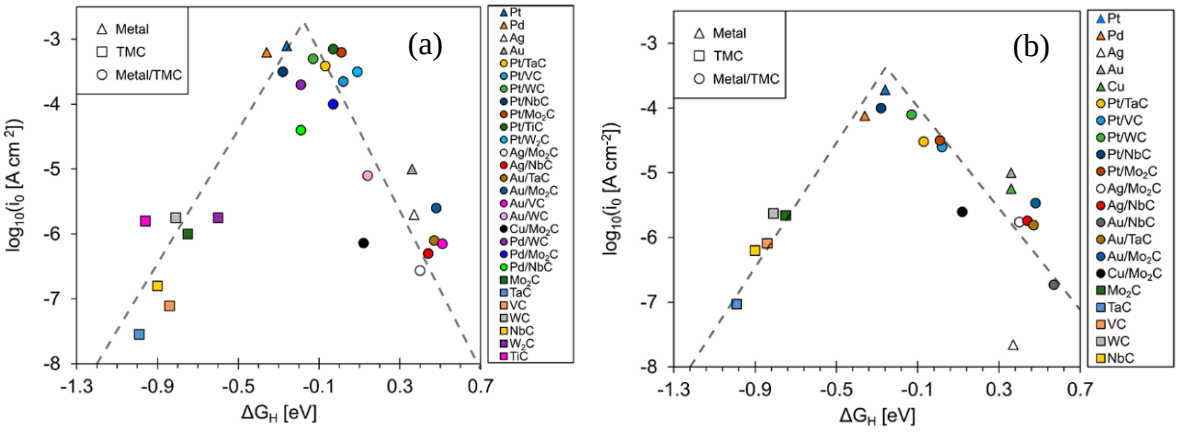

Figure 1.1 Volcano plot relating the exchange current density to the Gibbs free energy change of adsorbed hydrogen (ΔG_H) in (a) 0.5 M H_2SO_4 and (b) 0.1 M KOH. Reprinted

(adapted) with permission from Zhang et al.,[21] Copyright 2019, American Chemical Society.

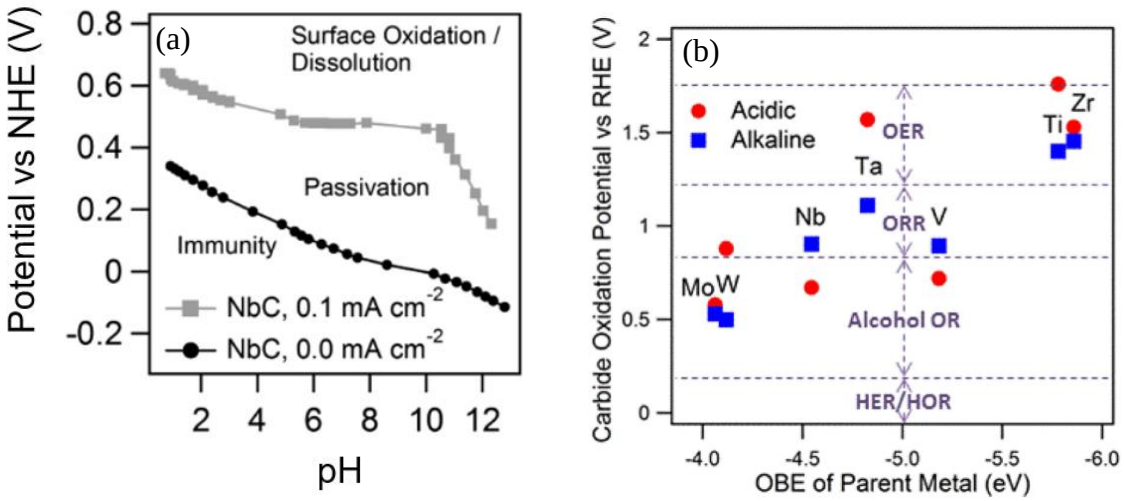

Figure 1.2 (a) Pseudo-Pourbaix diagram of NbC in wide pH-potential regimes. (b) Oxygen binding energy and TMC oxidation potential plotted to gauge material stability for relevant electrochemical reactions: oxygen evolution reaction (OER), oxygen reduction reaction (ORR), alcohol oxidation reaction (OR), hydrogen evolution (HER) and oxidation (HOR) reactions. Reprinted (adapted) with permission from Kimmel et al.,[22] Copyright 2014, American Chemical Society.

1.3 Utilization of Biomass-Derived Oxygenates

1.3.1 Ethanol Reforming

A second front where the discovery of active and selective earth-abundant catalysts can play a critical role in offsetting the carbon-footprint of conventional industrial practices is by altering the feedstock of certain commodity chemicals by utilizing biomass-derived oxygenates (BDOs). One of the most abundantly produced BDOs is ethanol, a simple C2 alcohol that has been successfully integrated with the liquid transportation infrastructure via gasoline blending.[25,26] From 2005 to 2019 corn ethanol production increased from 6.1 to 57 billion liters,

and the associated gasoline displacement led to an emission reduction of 544 million metric tons (MMT) of CO_2 over the same time period.[27] With this substantial increase in production, alternative pathways for ethanol valorization are increasingly important. One promising strategy is to use ethanol as a chemical feedstock for syngas, a gas-phase mixture of CO and H_2 central to the Fischer-Tropsch (FT) synthesis of olefins and other liquid hydrocarbons. Conventional FT processes utilize methane reforming techniques to generate syngas,[28,29] hence substituting this feedstock with biomass-derived ethanol should substantially reduce the CO_2 emissions associated with FT processes.

Many supported PGM catalysts have been studied for the selective reforming of ethanol. Studies on high surface area Ir/CeO_2 for steam reforming,[30] Pd-based membranes for oxidative reforming,[31] and Ru/TiO_2 for aqueous phase reforming[32] offer several industrially relevant strategies to generate bio-derived syngas. While these supported PGMs have interesting ethanol reforming activity, alternative earth-abundant materials, namely TMCs, have attracted the attention of researchers because these materials exhibit Pt-like properties, are stable in relevant reaction conditions, and may allow for reduced PGM-loading and admetal-dependent pathway tunability.[33–35] In addition, the carbon atoms that diffuse into the crystal lattice of a parent transition metal during TMC synthesis provide a diffusion barrier for admetals, which can improve catalyst stability.[36]

To this end, surface science studies have been conducted to assess bond scission order and pathway tunability for the reaction of ethanol on Mo_2C[37] and WC[38,39] thin films. Ethanol undergoes both the complete decomposition pathway and the methane production pathway on clean Mo_2C surfaces.[37] Mo_2C modified by Ni partially shifts the reaction pathway from decomposition to reforming, and Cu-modification similarly shifts the reaction pathway from

decomposition to dehydrogenation, which results in the desorption of gas-phase acetaldehyde. Despite this, the oxygen atom interacts strongly with the oxophilic Mo_2C surface, and complete decomposition is the primary reaction pathway on clean and Cu-/Ni-modified Mo_2C surfaces. The shift in reaction pathway selectivity was further assessed using DFT calculations of the ethoxy intermediate binding energy. Importantly, the binding energy of the ethoxy intermediate was lower on Ni- and Cu-modified Mo_2C surfaces, which partially preserved the C-O bond. Similar pathway tunability was demonstrated on WC, on which ethanol undergoes both complete decomposition and ethylene production pathways.[38,39] Ni-modification partially shifted the reaction pathway from decomposition and ethylene production to reforming and methane production pathways,[39] and sub-monolayer (ML) and ML Rh-modification resulted in a similar shift to reforming and methane production pathways.[38] Despite admetal-based reaction tunability, the synthesis procedures of TMCs can result in surface carbon overlayers that lower catalytic activity and impede substrate-admetal interactions. In consequence, inherently clean nitrogen-modified materials may be strategically leveraged as PGM-supports.

1.3.2 Glycerol Deoxygenation

Glycerol is a C3 polyol that is the main byproduct of biodiesel production. 10 kg of glycerol is produced as a byproduct for every 100 kg of biodiesel.[40] Biodiesel production has steadied over the last several years, with U.S. annual production being between 6.4 and 7.2 billion liters from 2018 to 2020.[41] While biodiesel has already been integrated into the liquid fuel infrastructure, additional valorization pathways for the primary byproduct of glycerol would generate further market incentives for biodiesel production.

The valorization of glycerol can be achieved through several deoxygenation pathways, including HDO and dehydration which maintain C3 product structure, as well as decarbonylation

which results in C1 and C2 products. The selective dehydration or HDO of glycerol can yield several products, including 1,2- and 1,3-propanediol, allyl alcohol, and propylene. These products are generally desired because the mechanism of oxygen removal leaves the C-C/C=C bonds intact for higher market value. The reaction of glycerol on powder catalysts and pristine surfaces has been studied and reviewed at length, including on supported bimetallic and metal-modified transition metal oxide and carbide systems.[40,42–47] Metal oxides that contain acid sites are also highly selective for dehydration.[48] Specifically, Pt/WO_x and inverse WO_x/Pt catalysts contain various deoxygenation active sites for the removal of oxygen from other BDOs.[49] Nonetheless, the nature of co-existing active sites in this system remains unclear and limits the design of catalysts for the selective C-O bond scission of functionally complex oxygenates.

1.3.3 Tetrahydrofurfuryl Alcohol (THFA) Ring-Opening

Heterocyclic BDOs such as tetrahydrofurfuryl alcohol (THFA) are important platform oxygenates that can be readily produced by the industrial processing of lignocellulosic biomass.[50–52] THFA can be upgraded into value-added diol molecules via selective ring-opening.[53,54] These diol molecules, including 1,2- and 1,5-pentanediol (1,2-PeD and 1,5-PeD, respectively), are important monomers for the manufacturing of polyester and polyurethane resins.[55,56]

The ring-opening reaction of THFA is catalyst dependent, and bifunctional catalysts such as Pt/WO_x and the inverse oxide WO_x/Pt have demonstrated selective C-O bond scission in the saturated furan ring to produce 1,5-PeD.[57,58] Other oxide-supported PGMs, including Rh/ReO_x and Rh/MO_x, also demonstrate selective ring-opening of THFA to produce 1,5-PeD.[59] In addition to ring-opening, THFA can undergo several degrees of undesired decomposition. In one study, while HREELS indicated that THFA partially hydrogenated to ring-open on Ir(111) and

Co/Ir(111) surfaces pre-dosed with hydrogen, gas-phase 1,5-PeD was not detected by TPD, and the 1,5-PeD-like intermediate underwent further decomposition to CO and H_2. Studies of WO_x/Pt are currently limited to supported powders, and a fundamental understanding of the active sites and reaction intermediates is needed to further improve the catalytic performance.

1.4 Synthesis and Characterization of Model Surfaces and Powder Catalysts

In this section, the synthesis and characterization of TMC and transition metal nitride (TMN) materials is discussed. A brief discussion of oxygen-modified earth-abundant materials can be found in Chapter 2. While TMC materials were not directly studied in the work presented herein, this discussion of TMC is included for contextual purposes. TMCs have similar physical and electronic properties to TMNs, and as will be discussed, there are key advantages to nitride materials that are better understood within the context of carbide synthesis.

The synthesis of TMC and TMN materials is application-dependent, and studies have utilized single crystal surfaces, polycrystalline foils, and powders to investigate their unique catalytic properties. In consequence, the methods of synthesis and characterization for these materials also differ.

The synthesis of carbide and nitride films on single crystal surfaces has enabled the study of reaction pathways over well-characterized surfaces, and has been useful in corroboration with DFT calculations on the same model surfaces. For these studies, carbide films have been prepared *in situ* on single crystal surfaces by the decomposition of unsaturated hydrocarbons (*e.g.* C_2H_4), a method that has been reviewed in detail previously.[34,60] In brief, carbide films have been synthesized on the surface of parent metal single crystals by undergoing multiple cycles of dosing C_2H_4 and annealing to substrate-dependent temperatures. For example, Mo_2C films have been synthesized on a Mo(110) surface by two cycles of dosing C_2H_4 at 600 K and annealing the

surface to 1150 K,[61] as well as on Mo(100) by exposing the surface to ethylene at 1200 K.[62] Similarly, WC films have been prepared on W(111) surfaces by 3 cycles of dosing C_2H_4 at 90 K and annealing the surface at 1200 K,[63] and on W(110) by heating the surface to 1250 K for 10 minutes in the presence of dosed C_2H_4, followed by flash annealing to 1900 K.[64]

Auger electron spectroscopy (AES) has been used to quantify the C/M atomic ratio to determine the carbide film stoichiometry. Low-energy electron diffraction (LEED) has also been used in combination with AES to identify the surface structure of carbide overlayers. For example, the above described C/W(111) synthesis yielded a sharp ($\sqrt{3} \times \sqrt{3}$)R30°-C/W(111) LEED pattern with an AES C(272 eV)W(182 eV) peak-to-peak ratio between 0.55 and 0.70.[63] These results informed both the surface structure and the atomic C/W ratio, which was calculated to be between 0.58 and 0.74. In contrast to carbide analogues, the synthesis of nitride films on single crystal surfaces has been experimentally challenging. Magnetron sputtering in Ar/N_2 gas environments has been used to deposit superlattice TiN, VN, and NbN films on MgO(100) substrates.[65] Additionally, metallic MoN single crystals have been synthesized by the direct conversion of $PbMoO_4$ single crystals in NH_3 environment at 1023 K.[66]

TMC and TMN films have also been synthesized on polycrystalline metal foils for surface science and electrochemistry experiments, and have been used to bridge the so-called "materials gap" between single crystal surfaces and high surface area powder catalysts. These films have been synthesized *in situ*,[67] similar to the synthesis of films on single crystals, and *ex situ* in a tube furnace (Figure 1.3(a)). The synthesis of TMCs and TMNs using a furnace often involves thermal decomposition of gas-phase carbon- and nitrogen-containing molecules, commonly CH_4 and NH_3, respectively (Figure 1.3(a)). Special efforts have also been made for as-synthesized films to be passivated at room temperature in a gas environment containing dilute

oxygen or H_2O to prevent pyrophoric bulk oxidation when exposed to atmosphere. For example, WC and Mo_2C films were synthesized by direct carburization of metal foils under a 1:2 volumetric flow mixture of CH_4 and H_2 at 1123 K. The films were then cooled to room temperature and passivated under a 1% O_2, balance N_2 gas mixture for 2 hours prior to being exposed to atmosphere.[23] In the same study, W_2C films were synthesized by magnetron sputtering a WC target onto a polycrystalline W foil, which was then carburized and passivated in a tube furnace. Tube furnace synthesis techniques of carbide thin films and powders can lead to the formation of thick carbon overlayers, which have been reported to curtail catalytic activity and impede the comparison of experimental surfaces to the ideal TMC surfaces used for DFT calculations.[68,69] In consequence, tube furnace synthesis techniques have been modified to limit the formation of these carbon overlayers. Specifically, after carburization in a CH_4/H_2 environment, CH_4 was removed from the gas feed, allowing surface carbon overlayers to react with pure H_2 at elevated temperatures.[68] Nitride films have also been synthesized on polycrystalline metal foils. In contrast to the carbon overlayers that formed during the synthesis of TMC, clean TMN surfaces were more easily formed because surface nitrogen desorbed as diatomic N_2. In one study, WN and NbN films were synthesized on W and Nb foils by the decomposition of NH_3 at 1123 K.[70] Nitride films on polycrystalline foils have also been synthesized using a similar magnetron sputtering method described for single crystal surfaces,[71] as well as pulsed laser irradiation in N_2 environments.[72,73]

TMC and TMN films on polycrystalline foils have been characterized using a combination of diffraction, spectroscopy, and microscopy techniques, which include symmetric and glancing-incidence X-ray diffraction (XRD and GI-XRD), X-ray photoelectron spectroscopy (XPS) under ambient-pressure (AP-), near ambient-pressure (NAP-), and ultrahigh vacuum

(UHV) conditions, and scanning electron microscopy (SEM). Symmetric XRD and surface-sensitive GI-XRD have been used in combination to determine the crystalline phase of TMC and TMN films in the bulk and at the surface. If the phases of the bulk and surface are different, the intensity of peaks associated with the thin film increases more in GI-XRD than the intensity of peaks attributed to the bulk. In addition to identifying the presence and phase of a TMC and TMN thin film, GI-XRD measurements can be used to estimate the thickness of the thin film. For example, GI-XRD measurements conducted with an incident X-ray angle of 5° were used to identify the phase of the Mo_2C, WC, and W_2C films, and with a probe depth of 350 nm, confirmed a minimum film thickness (Figure 1.3(bI)).[23] Similar analyses have been conducted on nitride films synthesized on polycrystalline parent metal foils. For example, with an incident X-ray angle of 1° a minimum film thickness of 55 nm WN and 140 nm NbN were synthesized on parent metal foils.[70] Other surface-sensitive techniques, namely XPS, have also been used to confirm carbide or nitride film stoichiometry. Additionally, XPS has been used to study the stability of the carbide and nitride films by comparing changes in the C/M or N/M ratio of fresh and spent foils.[70] SEM has also allowed the investigation of TMC stability by comparing changes in surface roughness of as-synthesized and spent foils.[24]

TMC and TMN powder catalysts have also been synthesized and passivated in tube furnaces (Figure 1.3(a)), with the same or similar gas composition and temperature range used for analogous thin films. Different carbon sources have been used for carburization, including CO, CO/CO_2, CH_4/H_2, C_2H_2/H_2, C_2H_6/H_2, and C_4H_{10}/H_2.[74–79]. It has been shown that the use of higher alkane can lower the carburization temperature, and the choice of carbon source had an effect on the carbide reactivity. Both N_2/H_2 and NH_3 have been used for the nitridification of transition metals.[78,80,81] More detailed studies on the effect of carburization and nitridification

agents on specific catalysts and reactions can be found in the original papers. In contrast to metal foils, precursors for TMC and TMN powders can be chemically complex, and include transition metal oxides, ammonium-containing hydrates, and carbonyls. For example, ammonium molybdate ($(NH_4)_6Mo_7O_{24}.4H_2O$),[82–88] molybdenum hexacarbonyl ($Mo(CO)_6$),[83] and molybdenum oxide (MoO_3)[87,89] have been used as precursors to synthesize molybdenum carbide powders in different phases (β-Mo_2C and α-MoC_{1-x}). In one study, ammonium molybdate was sieved to 125–250 μm, reduced in a H_2-only gas environment at 573 K, and carburized in 15 vol.% CH_4 with balance H_2 at 813 K to synthesize mixed-phase β-Mo_2C and α-MoC_{1-x}.[84] While the specific carburization temperature and gas composition vary depending on the precursor and desired phase, the synthesis methods of TMC powder in a tube furnace are generally similar for various TMCs. In addition to conventional tube furnace synthesis, other synthesis techniques have been developed for the study of morphologically unique TMC materials. For example, Baddour *et al.* utilized a millifluidic reaction system for continuous flow synthesis of carbon-supported MoC_{1-x} nanoparticles (2.2 ± 0.4 nm) from a $Mo(CO)_6$ precursor.[83] The synthesis of TMN powders often involves the same or similar precursors to those used in TMC synthesis, with the exception of replacing CH_4 with NH_3. For example, in one study ammonium molybdate was wet impregnated with a cobalt precursor ($Co(NO_3)_2 \cdot 6H_2O$), calcined in air to form an oxidic precursor, and then nitridified in a pure ammonia environment at 1023 K to form Co_3Mo_3N/Al_2O_3.[87] Ir/Fe_4N has also been synthesized using a similar wet impregnation technique of iron ($Fe(NO_3)_3$) and iridium ($(NH_4)_2IrCl_6$) metal salts, followed by nitridification under an ambient pressure flow of 100% ammonia at 773 K.[90]

While similar, and in many cases the same, techniques have been used to characterize TMC and TMN powders as thin films, several techniques are distinct. For example, GI-XRD

patterns are uninformative for nanoparticles because the particle size is of the same order of magnitude as depth profiling. In place of GI-XRD surface analysis, symmetric XRD of TMC and TMN powder catalysts has been used to characterize the degree of crystallinity and crystalline phase of the TMC and TMN powder materials. In one study, XRD was used to characterize carbon supported nanoparticle (NP) α-MoC_{1-x}, in comparison to bulk α-MoC_{1-x}. The NP α-MoC_{1-x} XRD revealed that the carbon-supported NP carbide was less crystalline than the bulk powder, as indicated by diffraction peak broadening.[83] XPS has been utilized similarly to study thin films, both for the quantification of the C/M or N/M atomic ratio and the identification of metal oxidation states near the surface region of powder catalysts.[91] Transmission electron microscopy (TEM) and modified scanning (STEM) and high-resolution (HR-TEM) TEM techniques have been used to investigate particle size, uniformity, and morphology of TMC and TMN powder catalysts. In one study, TEM was used to track the effect of carburization on nanoparticle size distribution. Specifically, TEM images revealed that the incorporation of carbon into the iron metal lattice increased the NP size from Fe(0) NP of 12.5 ± 0.6 nm to iron carbide NP of 15.1 ± 0.9 nm, without adversely affecting NP size homogeneity.[92] Similarly in a separate study, HR-TEM images of α-MoC_{1-x} NPs revealed an approximate crystallite size of 2.2 ± 0.4 nm based on the measurement of >100 unique crystalline domains.[83] Furthermore, the high-resolution enabled the imaging of lattice fringes of the carbide nanoparticles (Figure 1.3(bII)).[93] A combination of these characterization techniques has been adopted in many studies to better understand the relationship between material properties and catalytic activities.[82,83,89,92]

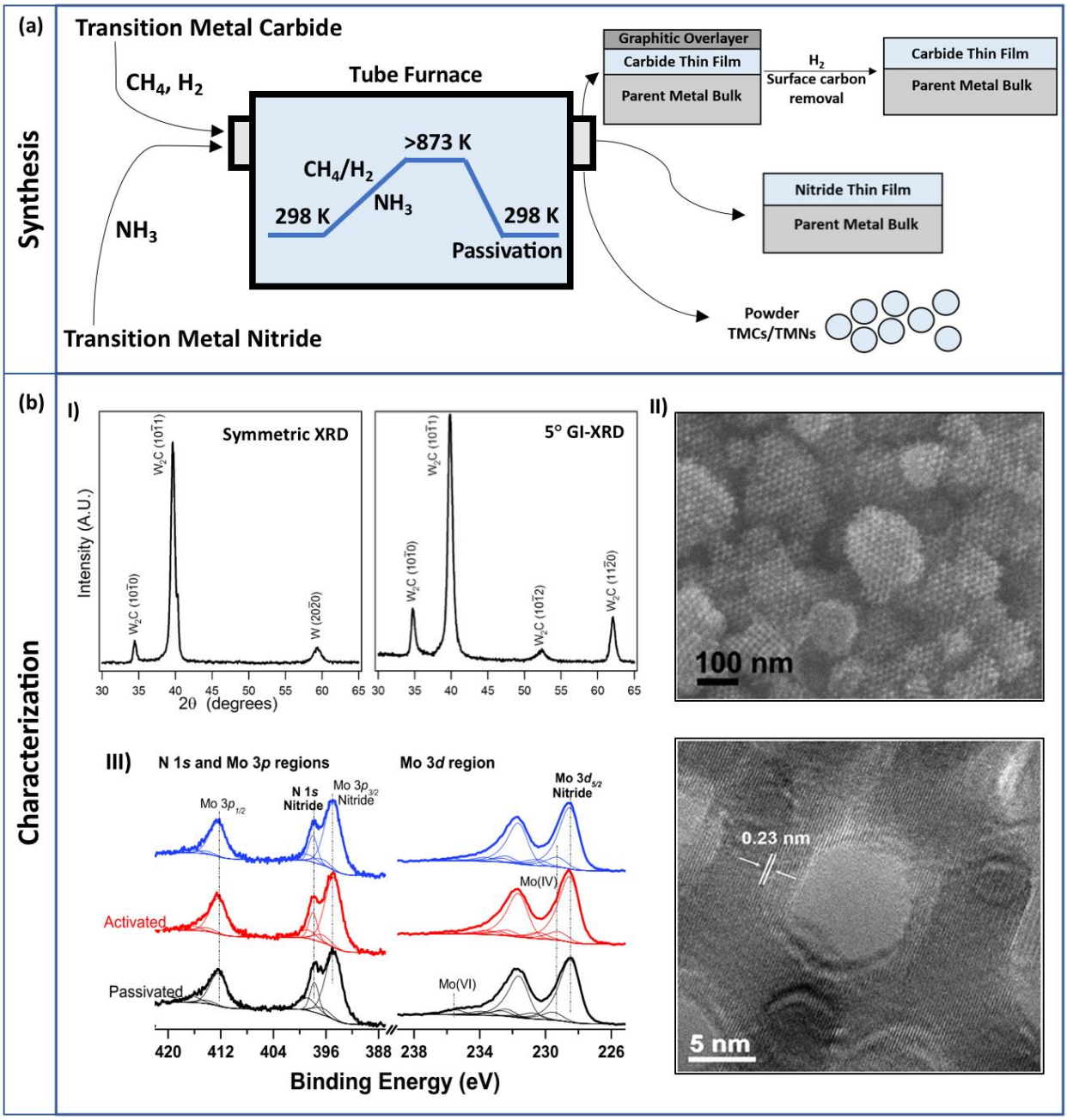

Figure 1.3 (a) Summary of conventional tube furnace synthesis techniques for TMC and TMN thin films and powders. (b) (I) Symmetric XRD (left panel) and GI-XRD (right panel) of a W_2C thin film. The surface sensitive GI-XRD with a 5° angle of incidence has a penetration depth of ~350 nm for W_2C, while symmetric XRD characterizes the bulk material. Reprinted from Weidman et al.,[23] Copyright 2012, with permission from Elsevier. (II) A typical SEM image for ordered mesoporous Mo_2C (top panel) and a typical HR-

TEM image of mesoporous Mo_2C (bottom panel). Reprinted with permission from Lu et al.,[93] Copyright 2016 American Chemical Society. (III) AP-XPS spectra of the Mo 3d, and the overlapping N 1 s and Mo 3p binding energy regions for a passivated, activated, and under-reaction-conditions 2 wt% Co/c-Mo_2N catalyst. Reprinted with permission from Yao et al.,[91] Copyright 2019 American Chemical Society.

1.5 Dissertation Outline

The preceding sections are helpful to understand the motivation for and technical background of the research presented herein, specifically on the study of nitrogen- and oxygen-modified earth-abundant catalysts. The scope of the remainder of the work is to combine electrochemical and surface science techniques to study important electrochemical and thermochemical reactions. Subsequent to the introduction, the dissertation contains 6 chapters outlined as follows.

Chapter 2 introduces the synthesis, characterization, electrochemical, and surface science techniques utilized in Chapters 3 – 6. The principles and schematics of select techniques, including Auger electron diffraction (AES), X-ray photoelectron spectroscopy (XPS), temperature programmed desorption (TPD), and high resolution electron energy loss spectroscopy (HREELS) are included to provide additional fundamental insight. Other techniques central to the work are also presented, including nitridificaiton, symmetric (XRD) and glancing incidence (GI-XRD) X-ray diffraction, and surface preparation. Some techniques, such as cyclic voltammetry (CV) and TPD quantification, are discussed in subsequent chapters where relevant.

Chapter 3 presents a study of the electrochemical stability of two TMNs, WN and NbN, over wide pH-potential regimes. From CV data, pseudo-Pourbaix diagrams are generated to

assess the potential use of these nitrogen-modified earth-abundant materials as catalyst and catalyst support materials for several relevant electrochemical reactions, including alcohol oxidation and CO_2 electrochemical reduction. HER is used as a probe reaction for unmodified and Pt-modified WN and NbN thin films, where activity is compared with DFT calculations of HER descriptors, such as HBE and ΔG_H.

Chapter 4 presents a study of unmodified and Pt-modified Mo_2N surfaces for the decomposition and reforming of ethanol, respectively. TPD is used to quantify activity and reaction selectivity, and HREELS is used to identify surface reaction intermediates. This study demonstrates the pathway tunability of a Mo_2N surface by Pt-modification, as low Pt coverages are shown to distinctly shift the reaction pathway from complete decomposition to reforming.

Chapters 5 and 6 present surface science studies of the reaction of two BDOs, glycerol and THFA, on WO_x-modified Pt(111) surfaces. The selected probe molecules were used to assess two unique and important thermochemical reactions, namely hydrodeoxygenation and ring-opening. The reaction of glycerol on WO_x/Pt(111) expands upon a colleague's previous work on the reaction of isopropyl alcohol, a similar C3 alcohol, on the same surface. The reaction of glycerol revealed several unique WO_x sites for dehydration and hydrodeoxygenation. The ring-opening of THFA is also studied on WO_x-modified Pt(111) surfaces. The functionally complex heterocyclic BDO is a potential platform oxygenate, and selective C-O bond scission is an important step in the production of the desired ring-opened product, 1,5-PeD. HREELS reveals the formation of a 1,5-PeD-like intermediate on clean Pt(111) and WO_x-modified surfaces, however gas-phase 1,5 PeD only desorbs from WO_x/Pt(111) via TPD experiments.

Chapter 7 provides concluding remarks, as well as future directions to continue the study of the work presented herein. More specifically, several ongoing DFT collaborations for Chapters 4 and 6 are discussed.

1.6 Acknowledgements

Parts of this chapter were adapted from *Z. Lin, S. R. Denny, and J. G. Chen, Journal of Catalysis, 2021, In Press.* No permission was necessary to reproduce sections of this publication for this thesis chapter.

Chapter 2: Experimental Methods

2.1 Synthesis and Characterization

2.1.1 Transition Metal Nitride Thin Film Synthesis

Transition metal nitrides (TMN) are formed when nitrogen atoms are incorporated into the interstitial sites of the crystal lattice of a parent transition metal. While several nitrogen source molecules and synthesis techniques have been used to prepare TMN thin films,[78,81] for the electrochemical and surface science experiments herein, nitride thin films were synthesized at the surface of parent transition metal foils in a quartz tube furnace under the ambient pressure flow of pure ammonia (NH_3). Prior to loading the foils into the furnace, parent metal foils were cut to size, typically 1 cm x 2 cm, and washed with ethanol, deionized (DI) water, and sodium hydroxide to remove oils from factory processing and surface oxides. The foils were loaded into the quartz tube furnace located in a fume hood and fit with corrosive resistant components. Foils then underwent a temperature programmed reaction in pure ammonia at 150 standard cubic centimeters per minute (sccm). For each parent metal foil, the temperature was ramped from 273 K to 1123 K in 2 h, then held for 10 h. After which the furnace was cooled to room temperature under the same gas flow, and purged with Argon gas. The foils were then removed and stored in a desiccator to limit exposure to atmosphere.

2.1.2 Transition Metal Nitride Characterization

The as-synthesized nitride thin films were characterized using a combination of X-ray photoelectron spectroscopy (XPS), symmetric X-ray diffraction (XRD), and glancing-incidence (GI-) X-ray diffraction techniques. XPS is a surface analytical technique that involves the irradiation of a sample with X-rays of a defined energy (in this work, Al Kα at 1486.6 eV), and the detection of the photoelectrons emitted by the sample. A general schematic of the XPS and

the mechanism of photoelectron emission are shown in Figure 2.1. The kinetic energy (KE) of the emitted electrons is described by Equation 2.1, where hν is the energy of the incoming photon from the X-ray source, BE is the binding energy of the atomic orbital from which the electron is emitted (ex. 1s, 2s, 2p, etc.), and Φ_S is the pre-defined work function of the spectrometer.

Equation 2.1 $$KE = h\nu - BE - \Phi_S$$

In brief, the X-ray bombarded surface emits photoelectrons upon electron excitation. Each element has a unique set of binding energies associated with emitted photoelectrons. Based on the set of detected binding energies, the elemental composition and oxidation states near the surface region can be determined. While the X-rays in UHV have a penetration depth on the order of magnitude of micrometers, the relatively short inelastic mean free path of electrons emitted from a solid-state material limits XPS analysis to the first several nanometers at the surface.

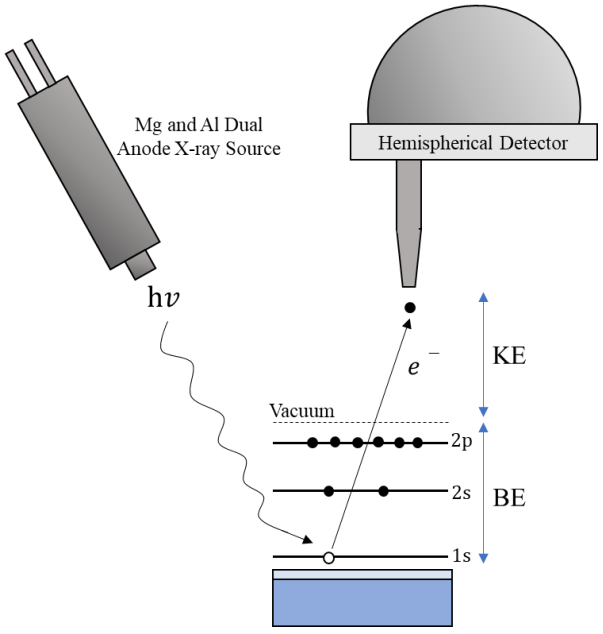

Figure 2.1 Schematic of an XPS apparatus and the mechanism of photoelectron emission from a material surface.

For the experiments herein, XPS was conducted in an ultrahigh vacuum (UHV) chamber with a base pressure of 5 x 10^{-9} Torr. Foils were adhered to stainless steel studs using carbon tape to prevent sample charging. The foils were placed in a loading chamber isolated by gate valve from the main chamber. The loading chamber was then brought to a pressure of < 5 x 10^{-3} Torr prior to being loaded into the main chamber for XPS measurements. XPS multiplex scans were used to quantify the relative atomic ratio of parent metal to nitrogen, which informed the surface-dominant nitride phase. The atomic ratio was calculated using Equation 2.2, where n_A is the atomic density (# of atoms/cm^3) of element A, I_A is functionally the integrated peak area associated with the intensity of emitted photoelectrons from a specific orbital of element A, and S_A is the empirically derived atomic sensitivity factor.

Equation 2.2
$$\frac{n_A}{n_B} = \frac{\left(\frac{I_A}{S_A}\right)}{\left(\frac{I_B}{S_B}\right)}$$

More detailed descriptions of the photoelectric effect, XPS instrumentation, and calculations related to XPS data are available in several texts in the literature.[94–97]

XRD techniques utilize hard X-rays to reveal structural information about the surface and bulk of a material sample. XRD utilizes a monochromatic incoming beam (Ex. Cu Kα) that is diffracted at defined angles related to the lattice planes of a crystalline material. The diffraction of incoming X-rays is characterized by Bragg's Law, shown in Equation 2.3, where n is an integer, λ is the wavelength of the incident X-rays, d is the spacing between planes that generates diffraction, and θ is the angle of diffraction with respect to the surface.

Equation 2.3
$$n\lambda = 2dsin\theta$$

Similar to element-specific X-ray photoelectron spectra, the diffraction patterns of crystalline materials are unique to a crystal structure and composition. While XRD is a powerful tool to analyze crystalline properties, the penetrating depth of the X-rays used often limits

application to the study of bulk materials rather than thin films present at the surface. In contrast, by lowering the incident X-ray angle, GI-XRD can be used to characterize crystalline properties near the surface region, such as the presence, thickness, and phase of a thin film. Relevant to this work, XRD was used to identify the chemical composition of as-synthesized foils, the nitride phase(s), the surface dominant phase, the thin film thickness, and other relevant material properties. Symmetric XRD informed properties relevant to the material bulk, and GI-XRD was used to determine parameters relevant to the as-synthesized thin film. Additional descriptions of X-ray diffraction and XRD instrumentation are available in the literature.[96,98,99]

2.1.3 Surface Preparation

Surfaces for electrochemical and surface science experiments were prepared using different protocols. For electrochemical experiments, TMN thin films were prepared by undergoing a series of cleaning steps to remove surface oxides. Specifically, prior to metal deposition, the as-synthesized thin films underwent a rinse in sodium hydroxide and DI water. The dried foils were then loaded into the XPS for metal modification, or prepared directly for electrochemical experiments.

In comparison, the preparation of nitride, metal-modified nitride, single crystal, and WO_x-modified single crystal surfaces for surface science experiments was more involved. The polycrystalline foil or single crystal was spot welded to two Ta posts for resistive heating, and cooled by contact with a liquid nitrogen reservoir on the opposite side of the feedthrough. A K-type thermocouple was welded to the back of the foil or crystal at a single point to monitor temperature. Before surface-modification by physical (PVD) or chemical vapor deposition (CVD), the surface was cleaned using a combination of Ne^+ sputtering, oxygen treatment, and annealing. Ne^+ sputtering utilized ionized Ne directed at the surface to bombard and remove

surface species, such as carbon, oxygen, or intentional modifications (ex. admetal, WO_x). The surface could also be treated by dosing oxygen at elevated temperatures to remove surface carbon. After cycles of sputtering and oxygen treatment, the film or crystal was annealed to high temperatures (>1000 K) to homogenize the surface and remove any adsorbed species. Cycles of these preparation procedures were done to the extent that the presence of carbon, oxygen, and metal species were negligible on Auger electron spectra, after which experiments were conducted or the surface underwent further modification.

2.1.4 Physical Vapor Deposition

PVD is a line-of-sight metal deposition technique that was used herein to modify the nitride thin films with sub-monolayer (sub-ML) and ML coverages of a desired admetal. A typical schematic of the PVD apparatus is shown in Figure 2.2, where a thin, ultrapure wire of the desired deposition metal is tightly wrapped around a thicker W filament, isolated inside of a protective Ta shield. The filament is resistively heated using a DC power supply, and the thin metal wire vaporizes in vacuum and deposits on all surfaces within a field of vision. The Ta cage directs deposition to a sample oriented in front of the filament for a set time and applied current. While the PVD apparatus was functionally identical for the preparation of surfaces for both (1) surface science and (2) electrochemical experiments, the spectroscopy technique and quantification of overlayer coverage were different.

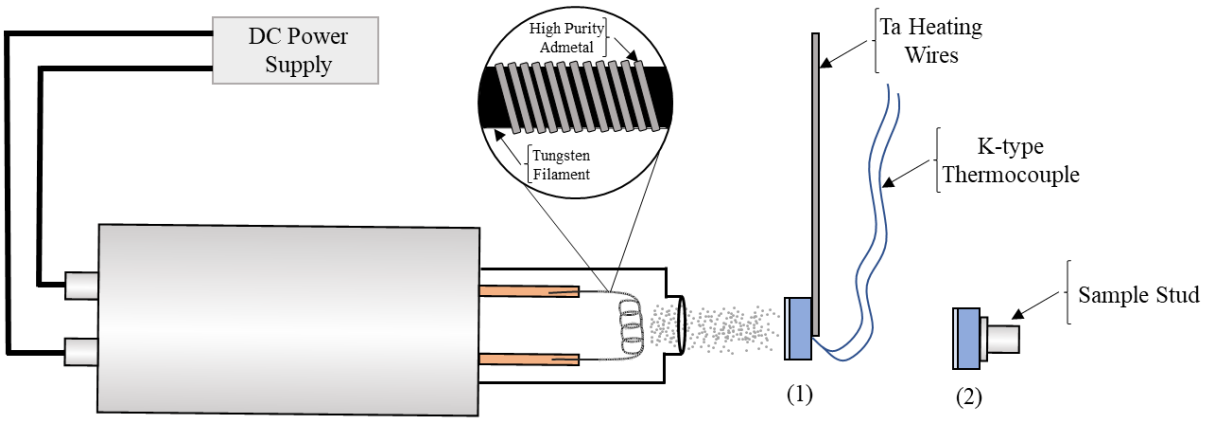

Figure 2.2 Schematic of a PVD apparatus. (1) Representative of PVD onto a sample mounted for surface science experiments; (2) Representative of PVD onto a sample prepared for electrochemical experiments.

For the metal-modification of nitride thin films intended for electrochemical experiments, foils were loaded into a UHV chamber equipped with both PVD and XPS. XPS is used to quantify the overlayer thickness, based on Equation 2.4, where I_A and S_A are the intensity of the integrated peak area and the empirically-derived sensitivity factor of overlayer element A, λ^A_{IMFP} is the inelastic mean free path of electrons emitted by A atoms, which is a function of the kinetic energy of emitted photoelectrons (E_A), θ is the X-ray angle of incidence, and d is the thickness of overlayer material A over substrate material B.

Equation 2.4

$$\frac{I_A/S_A}{I_B/S_B} = \frac{1-\exp\left[-\frac{d}{\lambda^A_{IMFP}(E_A)\cos\theta}\right]}{\exp\left[-\frac{d}{\lambda^A_{IMFP}(E_B)\cos\theta}\right]}$$

2.1.5 Auger Electron Spectroscopy

For the metal-modification of nitride thin films for surface science experiments, Auger Electron Spectroscopy (AES) was used to quantify admetal deposition. AES is a UHV technique that utilizes the Auger effect, similar to the photoelectric effect, to qualitatively and quantitatively determine the surface elements and the thickness of surface overlayers. A

schematic of the instrumentation and the mechanism of Auger electron emission is shown in Figure 2.3. Briefly, upon excitation by an electron beam, a core level electron is displaced leaving an unstable hole (Figure 2.3 (1)). When an outer level orbital relaxes to fill the hole in the inner orbital, an Auger electron is simultaneously emitted from the outer orbital (Figure 2.3 (2)). The energy of the emitted Auger electron is detected and attributed to a specific elemental fingerprint, as described by Equation 2.5, where the energy of the emitted electron is equal to the difference between the energy of the core-level electron and the coupled energy of the electron orbital of the relaxed and emitted outer electrons.

Equation 2.5 $$E_{KLL} = E_K - E_{L_1} - E_{L_2}$$

AES is also used for the quantification of deposited overlayers, by PVD, CVD, or some other surface modification method (e.g. ALD). The quantification of surface overlayers is thoroughly discussed in the literature, and is based upon sensitivity factor-adjusted intensities of characteristic, element-specific Auger electron emissions.

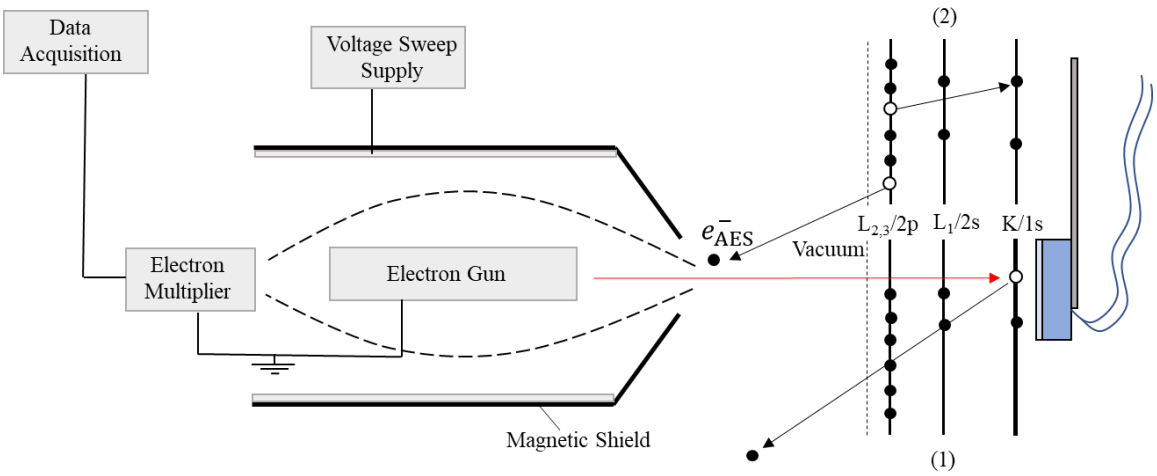

Figure 2.3 Schematic of a typical AES apparatus and the mechanism of Auger electron emission from a material surface.

2.1.6 Chemical Vapor Deposition

CVD is a technique that utilizes thermally decomposed metal precursors in the gas-phase for surface modification. Herein, WO_x was synthesized on the surface of a Pt(111) single crystal surface by dosing vaporized tungsten hexacarbonyl ($W(CO)_6$) into the chamber, in the presence of oxygen, through a directional gas line connected to a leak valve. While the deposition could be controlled by either changing the temperature of the substrate, and thereby modifying the initial sticking probability of the dosed species, or increasing the exposure, the later was the relied upon for this work. The adsorbed $W(CO)_6$ underwent electron-induced decomposition by the AES electron beam during surface characterization. The partially decomposed surface species was then oxidized at elevated temperatures with dosed O_2, and reduced in a H_2 environment. While this briefly outlines the relevant CVD procedure herein, the technique is a powerful tool to deposit diverse metal compounds onto several classes of substrates. More detailed accounts of CVD precursors and deposition mechanisms are available in the literature.[20,96]

2.2 Electrochemical Techniques

2.2.1 Three-Electrode Electrochemical Cell

A three-electrode cell, by its name, utilizes three electrodes immersed in an aqueous electrolyte connected by a potentiostat. The potentiostat controls the potential of the working electrode by electrochemically referencing the constant potential of a saturated calomel, Ag/AgCl, or reversible hydrogen (RHE) reference electrode. The potential and current are read at the working electrode, from which current flows between a counter electrode. Of an overall electrochemical reaction, a complementary oxidation or reduction half-reaction occurs at the

working and counter electrode. The electrolyte can be either acid or alkaline, but is electrically conductive via the ionic composition of the media.

Relevant to the work presented herein, the working electrode was the electrode of material interest (NbN or WN). The counter electrode was a graphite rod. Potentials were reported vs. RHE, and current was reported per unit geometric area. The current was also corrected for the solution resistance by using electrochemical impedance spectroscopy (EIS) measurements.

2.2.2 Linear Sweep Voltammetry

Linear sweep voltammetry (LSV) experiments sweep the potential of the working electrode at a constant rate, from which the generated current is measured. For a reduction reaction, the initial potential is positive of the standard reduction potential (E^0) and is swept to negative potentials. In a typical experiment the initial potential is selected to minimize the flow of oxidative or reductive current. As the potential sweeps negatively, a reductive current is generated and a half-reaction occurs at the surface of the working electrode. Data of the reduction current can be used to quantify important reaction parameters, such as the exchange current density (i_0) or Tafel slope, which provide insight into the catalytic activity of an experimental cathode material.

For the hydrogen evolution reaction, LSV experiments are used to inform key reaction parameters by Tafel analysis. The Tafel equation (Equation 2.7) is a simplified Butler-Volmer equation (Equation 2.6), based on the assumption that the overpotential at the cathode is dominant. The Tafel equation can be linearized (Equation 2.8), from which the Tafel slope (Equation 2.9) and the exchange current density (Equation 2.10) can be calculated, where i represents current density (A/cm^2), α represents transfer coefficient (assumed to have a scalar

value of 0.5), η_s represents surface overpotential (V), F represents Faraday's constant (C/mol), R represents the gas constant (J/mol·K), and T represents temperature (K).

Equation 2.6 $$i = i_0 \left(exp\left(\frac{\alpha_a F \eta_s}{RT}\right) - exp\left(\frac{-\alpha_c F \eta_s}{RT}\right)\right)$$

Equation 2.7 $$i = -i_0 exp\left(\frac{-\alpha_c F \eta_s}{RT}\right)$$

Equation 2.8 $$\eta_s = mlog(|i|) + b$$

Equation 2.9 $$m = \frac{-2.303RT}{\alpha_c F}$$

Equation 2.10 $$b = -mlog_{10}(i_0)$$

2.3 Surface Science Techniques

2.3.1 Temperature Programmed Desorption

Temperature programmed desorption is a surface science technique that uses mass spectrometry (MS) to detect the gas-phase reaction products of an adsorbed species on a thin film or single crystal surface. In a typical experiment, reactants were directionally dosed in Langmuir units (1 L = $1x10^{-6}$ Torr·s) onto a prepared and liquid N_2-cooled surface. After dosing the reactant, the surface was oriented normal to a quadrupole MS with approximately 1 mm separation, and was heated at a linear rate (ex. 1 K/s or 3 K/s). MS was used to detect the desorption of gas-phase products upon the controlled heating of the surface. Spectra of several gas cracking patterns were collected to quantify product yield and selectivity.

Products often have overlapping gas cracking patterns, and molecule-specific masses are used to determine the desorption of unique gas-phase products. For example, ethylene and CO both have gas cracking patterns at 28 atomic mass units (amu), however between the two molecules, ethylene has a unique cracking pattern at 26 and 27 amu. If a desorption peak is

observed on a 28 amu spectrum, but not the corresponding 26 and 27 amu spectra, one can reasonably conclude that the desorption was associated with CO and not ethylene.

The desorption onset and peak temperatures can also inform the binding energies of adsorbates or the reaction barrier, based on the mode of desorption. With a reaction-limited desorption mechanism, a reaction product desorbs from the surface upon formation, and desorption temperature relates to the energy of the reaction barrier. If the desorption mechanism is desorption-limited, the formed and surface-bound reaction product only desorbs upon a threshold heating of the surface. In this case, the desorption onset and peak temperatures correspond to the binding energy of the adsorbate.

2.3.2 High Resolution Electron Energy Loss Spectroscopy

High resolution electron energy loss spectroscopy (HREELS) is a UHV vibrational spectroscopy technique that detects the energy of scattered electrons from a monoenergetic beam directed at a surface. Distinct peaks in an HREEL spectra are attributed to the vibrational energy losses associated with chemical bonds of an adsorbate or reaction intermediate species on the surface.

A schematic of HREELS is shown in Figure 2.4, where a 6 eV electron beam emits from a source, is transmitted through monochromator and lens, scattered at the surface upon incidence at an angle of 60º, and refocused through a lens for analysis. Several types of electron scattering may occur from the surface. Elastic scattering is the reflection of the primary beam, where energy is conserved. This mode of scattering is dominant and provides a basis for signal normalization and spectra alignment to zero wavenumber. Three main types of inelastic scattering can also take place, which include dipole scattering, impact scattering, and inelastic scattering associated with negative ion resonances. The latter two scattering processes result in

count rates that are orders of magnitude less than dipole scattering, and consequently, dipole scattering that results in electron energy loss less than 4000 cm^{-1} (0.495 eV) is informative of the adsorbed surface species. Dipole scattering is near the specular direction and occurs when an electron interacts with a dipole potential from an adsorbate. The orientation of the dipole is important. When the dipole is (1) perpendicular, the dipole potential extends into the vacuum and the electron interacts strongly to induce dipole scattering. In contrast, when the dipole is (2) parallel to the surface, the image dipole cancels the dipole moment, and no scattering is observed. Detailed discussions of HREELS instrumentation and electron scattering mechanisms are available in the literature.[20,100]

Experimentally, the HREELS beam is tuned to an electrically grounded clean surface, where various voltage parameters in the monochromator, lens, and analyzer are adjusted to maximize the detected beam counts per second (cps), and minimize the peak full width at half maximum (FWHM), which enhances peak identification. Once tuned, the surface is prepared and exposed to the desired reactant. An initial HREELS scan is taken at the liquid N_2 cooled base temperature of the surface, which is typically between 110 K and 120 K. The surface is then raised from the Mu metal cage which shields the incidence region from low-frequency magnetic fields. The surface is flashed to a desired temperature and cooled to below 200 K before conducting further HREELS experiments. Typically, the surface undergoes thermal sequencing to several specific temperatures, which are selected based on the results of temperature programmed desorption experiments. For example, if a gas-phase product has a desorption onset temperature of 300 K, HREELS spectra may be collected at temperatures below, at, and above 300 K to better understand the adsorbed surface species.

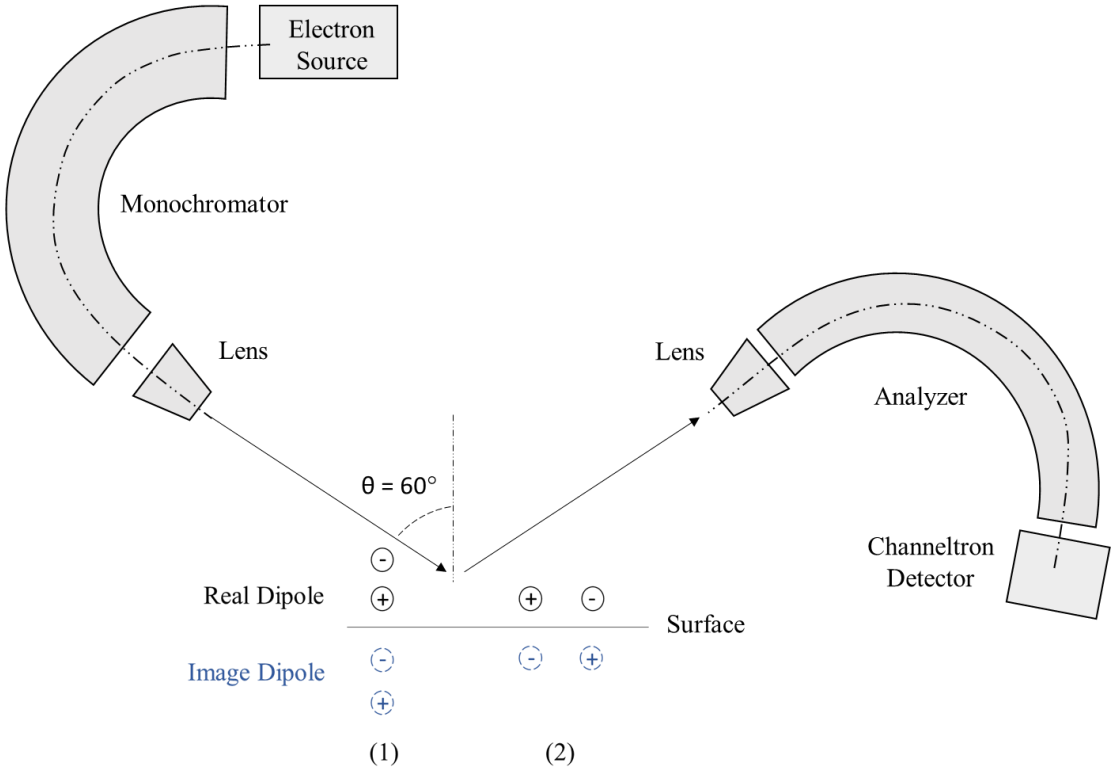

Figure 2.4 Schematic of a HREEL spectrometer and dipole scattering.

Chapter 3: Exploring Electrocatalytic Stability and Activity of Unmodified and Platinum-Modified Tungsten and Niobium Nitrides

3.1 Introduction

Transition metal carbides (TMC) have been utilized as versatile electrocatalyst supports that offer a template to tailor activity toward a variety of electrocatalytic reactions.[10,101–104] However, creating high surface area carbides is challenging due to high synthesis temperatures and the formation of carbonaceous overlayers that result from synthesis in the presence of methane.[68,105] The latter can lead to discrepancies in correlating between the pristine carbide surfaces used in DFT calculations and the often carbon-covered carbide surfaces used as electrocatalyst supports.[69]

Transition metal nitrides (TMN), on the other hand, are synthesized by decomposing ammonia to elemental nitrogen that is driven into the metal lattice, with extra surface nitrogen atoms readily desorbing as molecular nitrogen instead of accumulating on the TMN surfaces. These inherently "clean" surfaces should correlate well with DFT calculations, which should facilitate new catalyst design by maximizing the utility of DFT-calculated descriptors as screening tools. Additionally, it should be more feasible to support metal-modifiers on TMN surfaces without the interference from carbonaceous overlayers on TMC. Nitrides of early transition metals typically have similar physical structures and electronic properties as their carbide counterparts,[60,106] which may impart similar stability and versatility for different electrochemical reactions.[107] Here, the utility of TMN as electrocatalyst materials was explored by focusing on nitrides of niobium and tungsten. The electrochemical stability of both nitrides was evaluated in

wide potential-pH regimes to generate Pseudo-Pourbaix diagrams, which have been shown previously to be useful for selecting appropriate TMC electrocatalysts for specific reactions.[22] The hydrogen evolution reaction (HER) was selected as a probe reaction, where the activities of unmodified and Pt-modified TMN thin films were measured and correlated to the DFT-calculated hydrogen binding energies and Gibbs free energies for hydrogen adsorption to demonstrate the relationship between experimental results and DFT calculations.

3.2 Methods

3.2.1 Synthesis

Nitride thin films were prepared from foils of 0.127 mm thick Nb (99.97%) and 0.1 mm thick W (99.95%) from Alfa Aesar. The foils were sonicated for 5 minutes in ethanol to remove any oils from factory processing, rinsed with DI water, sonicated for 5 minutes in 1 M NaOH to remove surface oxides, and rinsed a final time with DI water before being loaded into a horizontal quartz tube furnace. Under an ambient pressure gas flow of 100% ammonia at 150 standard cubic centimeters per minute (sccm), the furnace was ramped from room temperature to 1123 K in 2 h, then held at 1123 K for 10 h. The resulting nitride films were cooled to room temperature under the same gas conditions and then purged with Argon before removal from the furnace.

Pt was deposited on the nitride thin films via physical vapor deposition (PVD) in an ultra-high vacuum (UHV) chamber equipped with X-ray photoelectron spectroscopy (XPS). Prior to Pt deposition, the nitride films were sonicated in 0.3 M NaOH for 5 minutes, washed with DI water, and dried in atmosphere. For PVD, a Pt wire (Alfa Aesar, 99.99%) was wrapped around a tungsten filament, which was resistively heated in the vacuum chamber. The nitride sample was placed in front of the Pt source for deposition, and the Pt coverage was determined from the XPS measurements[108] without exposing the sample to atmosphere.

3.2.2 Characterization

XPS measurements were conducted using a PHI 5600 XPS unit with a hemispherical analyzer and an Al X-ray source. The chamber had a base pressure of 2×10^{-9} Torr. Peak positions were calibrated to the adventitious carbon peak at 284.4 eV.

X-ray diffraction (XRD) was used to characterize the nitride thin films. A PANalytical XPERT3 Powder XRD with Cu Kα radiation was used. The stage was held stationary (no spinning) for both symmetric and glancing incidence measurements. Glancing incidence XRD measurements were conducted by holding the incident X-ray angle at 1 degree.

3.2.3 Electrochemical Measurements

The nitride films were sonicated at room temperature in 0.3 M NaOH for 5 minutes to remove surface oxides, then rinsed with DI water. Each sample was then taped with 3M 470 electroplating tape to define the surface area exposed to electrolyte. The geometric surface area was measured and used to calculate current density.

Electrochemical stability testing was conducted at room temperature in a buffered electrolyte solution of 0.5 M H_2SO_4, 0.1 M H_3PO_4, and 0.1 M $NaSO_4$. Experiments were performed in a standard three-electrode, single-cell setup using a Princeton Applied Research VersaSTAT 4. A saturated calomel electrode (SCE) was used as the reference electrode and a graphite rod (Sigma-Aldrich, 99.995%) was used as the counter electrode. The pH values and temperature were measured using a Thermo Scientific Orion Star A211. Titrations were conducted using concentrated base (5 M NaOH), and electrolyte temperature was maintained at 293 K by flowing chilled water through a water jacket in contact with the cell. A magnetic stir bar was used during titrations, but turned off for electrochemical testing. After each titration, the electrolyte

temperature was allowed to return to 293 K, which typically occurred within 3 to 10 minutes. A fresh nitride film was used for measurements at each pH value.

Before electrochemical stability testing, the electrolyte was purged for 20 minutes with argon. The electrolyte was then continuously purged with Ar during subsequent titrations and electrochemical testing. Working electrodes were cleaned via cyclic voltammetry (CV), by which the potential was cycled from 0.05 V_{RHE} to 0.3 V_{RHE} at 50 mV s^{-1} for 20 cycles. Additional CVs were then conducted to measure the current response to more positive potentials, where the potential was cycled from 0.05 V_{RHE} to 1.8 V_{RHE} at 50 mV s^{-1} for 5 cycles. The uncompensated solution resistance was measured by electrochemical impedance spectroscopy (EIS), which was conducted before CV measurements.

To assess the HER activity of unmodified and Pt-modified WN and NbN, prepared films were cleaned in Ar-purged electrolyte (0.5 M H_2SO_4 or 0.1 M KOH) using the same cleaning CV parameters described for stability testing. The electrolyte was then purged for 20 minutes using hydrogen, which continued throughout linear sweep voltammetry (LSV) testing. Cathodic linear potential sweeps were conducted at 10 mV s^{-1} from 0.05 V_{RHE} until a current density of 5 mA cm^{-2} was achieved.

To assess the stability of Pt overlayers on nitride thin films, two sets of three linear sweeps were conducted. Each set of LSV testing took place over the course of an hour. After each set, the thin film was removed from the electrolyte, rinsed in DI water, and dried in atmosphere. The dry film was then loaded into the UHV chamber for XPS characterization. After XPS scans were conducted on each film from the first hour of HER testing, the film was removed from the UHV chamber and reintroduced to the H_2-saturated electrolyte for additional HER measurements and subsequent XPS characterization.

3.2.4 Density Functional Theory Calculations

Spin polarized density functional theory (DFT)[109,110] calculations were performed using the generalized gradient approximation (GGA) within the projector augmented wave (PAW) Perdew-Wang-91 (PW91) formulism[111,112] on the Vienna *Ab-Initio* Simulation Package (VASP) code.[113,114] The total energy calculations were performed using a 3 × 3 × 1 Monkhorst-Pack grid[21] and a plane wave cut-off energy of 400 eV.[101]

According to XRD characterization, the hexagonal closed packed (HCP) NbN(0001) surface and the face centered cubic (FCC) WN(111) surface were modeled using four bilayers, each containing one layer of Nb or W and one layer of N atoms, with a 3 × 3 surface slab. For the reference Pt surface, a 3 × 3 (111) unit cell with four layers was used.[21] For the Pt-modified NbN(0001) and WN(111) surfaces, one monolayer of Pt was placed on the NbN(0001) or WN(111) surface. A vacuum layer of ~15 Å thick was added in the slab to minimize interactions between the slab and the periodic images perpendicular to the surface. Atoms in the bottom two layers were fixed, while all other atoms, including those of adsorbates, were allowed to relax until the force on each ion was smaller than 0.02 eV $Å^{-1}$ during geometry optimization. The convergence criteria was selected as 1×10^{-5} for structure optimization.

The hydrogen binding energy (HBE) was calculated as:

Equation 3.1 $$E_{(Binding\ Energy)} = E_{(slab-H)} - E_{(slab)} - E_{(H)}$$

where $E_{(slab-H)}$, $E_{(slab)}$ and $E_{(H)}$ were the total energy of the slab with adsorbed H atom, the total energy of the clean slab, and one-half of the total energy of a H_2 molecule in the gas phase, respectively.

The free energy (G) of a species was calculated as[115]:

Equation 3.2 $$G = E + ZPE - TS$$

where E represented the total energy of a species obtained from DFT calculations, ZPE was the zero-point energy, S was the entropy of a species, and T = 298.15 K. The change in free energy (ΔG) was calculated as[116].

Equation 3.3 $$\Delta G = \Delta E + \Delta ZPE - T\Delta S$$

where ΔE was the binding energy of adsorbed species.

3.3 Results and Discussion

3.3.1 XRD Characterization

As-synthesized tungsten nitride and niobium nitride thin films were analyzed with symmetric and glancing incidence (GI) XRD to determine the nitride phase. In Figure 3.1, the symmetric XRD patterns showed the most intense reflections for the pure metal peaks and less intense reflections for nitride phases. This indicated that the nitride domain existed as a thin film on the foil surface, and most of the intensity was reflected from X-rays penetrating deeper into the foil. GI-XRD measurements were more sensitive to surface layers, and Figure 3.1 showed that fixing the incident X-ray angle at 1 degree revealed relatively more intense nitride phase peaks. Using the linear attenuation coefficient of each parent metal, the thin film thicknesses were ~55 nm and ~140 nm for WN and NbN, respectively, using GI-XRD. These findings were consistent with previous studies on similarly synthesized carbide films.[35] The reference XRD patterns revealed that the nitride phase in the thin film on the niobium foil was a mixture of hexagonal NbN (COD 9008874) and Nb_2N (ICSD 76387). The phase on the tungsten thin film was FCC WN (ICSD 30381). XPS analysis of the as-synthesized nitride thin films revealed that the nitrogen:metal ratio on the surface of each nitride film was roughly 1 (Figures 3.2(c) and 3.2(d)). This indicated that the surface stoichiometry for both nitrides was M_1N_1 when synthesized at 1123 K in 100% ammonia. The Nb-rich phase observed with XRD was likely from deeper beneath the

surface, and therefore contributed less to the N:Nb signals measured with the more surface sensitive XPS. The (110) reflection of W and (111) reflection of WN were missing. This was likely due to the preferred grain orientation of the as-received W foil used for these measurements. Similar preferential grain orientation resulting in a diffraction pattern dominated by the W(200) plane has been observed on previous studies of carburized tungsten foils.[24]

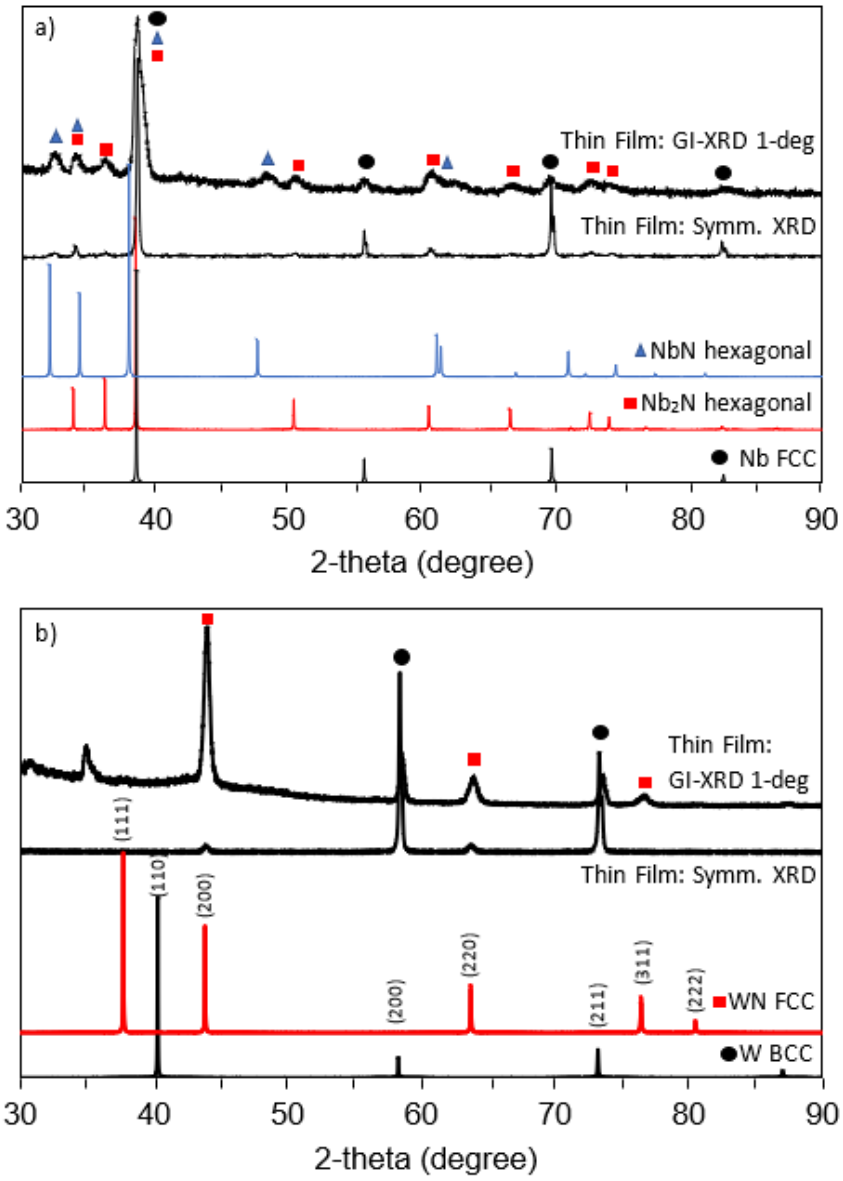

Figure 3.1 Tungsten nitride and niobium nitride thin film X-ray diffraction patterns. (a) Niobium nitride and (b) tungsten nitride thin film XRD patterns with diffractometer operated in symmetric mode and glancing incidence (GI) mode at an incident angle of 1 degree.

3.3.2 Electrochemical Stability

In order to determine the nitride stability over a wide range of potential-pH values, the thin films were evaluated using a cyclic voltammetry (CV) titration technique to create a pseudo-Pourbaix diagram. These types of pseudo-Pourbaix diagrams have been utilized previously to describe carbide stability.[22–24] Pseudo-Pourbaix diagrams typically include three distinct regions of stability: stable, passivation, and oxidation/dissolution. The stable region represents potential-pH conditions where the catalyst surface is relatively immune to oxide formation. The passivation region is defined by potential-pH values where the surface is mildly oxidized to form a passivating layer, but the bulk remains stable. In contrast, the oxidation/dissolution region is characterized by potential-pH conditions where the catalyst surface is oxidized severely and the formed oxides dissolve into the electrolyte. In this work, these diagrams were created by identifying the potentials at which specific oxidation peaks occurred at each pH. The CVs at the initial pH of 0.3 exhibited multiple distinct oxidation peaks on the first potential cycle for both NbN and WN (Figures 3.2(a) and 3.2(b)). For WN, these oxidation peaks were followed by current resulting from the oxygen evolution reaction above 1.6 V_{RHE}. The oxidation peaks below 1.6 V_{RHE} were not present on the second CV cycle for either nitride, indicating an irreversible oxidation.

The extent of nitride oxidation as a function of applied potential was determined with XPS. Different thin film samples were used for XPS surface analysis before and after 5 CV cycles with a maximum potential corresponding to one of the distinct oxidation peaks (Figures 3.2(c) and

3.2(d)). The N:Nb atomic ratio for each fresh NbN sample was measured with XPS and calculated to be between 1.0 and 1.2, which was in good agreement with the NbN XRD phase determination in Figure 3.1(a). After CV cycling to 1.0 V_{RHE} in an electrolyte with pH of 0.3, the N:Nb atomic ratio remained essentially unchanged, indicating that the first oxidation peak at 1.0 V_{RHE} was likely a result of passivation of defect or low-coordinated sites. However, after cycling to 1.3 V_{RHE} and 1.5 V_{RHE}, corresponding to the second and third oxidation peak, the N:Nb ratio decreased to values between 0.6 and 0.4. This change in N:Nb ratio indicated that severe oxidation of the nitride thin film began at 1.3 V_{RHE}. Thus, the pseudo-Pourbaix diagram for NbN was created by assigning potentials higher than the second most positive peak as "oxidizing", potentials lower than the onset of the initial peak as "stable", and the potentials in between as "passivating". The same peak designations were used for NbN at each pH because the oxidation CV maintained the same shape regardless of the pH of the electrolyte.

A similar trend was observed for the WN thin film in pH 0.3 electrolyte when evaluated by XPS after cycling to different oxidation potentials (Figure 3.2(d)). Specifically, the N:W ratio remained close to that of the fresh sample after cycling the potential to the initial oxidation peaks at 1.2 V_{RHE} and 1.3 V_{RHE}, but reduced to less than 0.8 when cycled to the most positive peak at 1.5 V_{RHE}. Therefore, potentials less than the onset of the initial WN oxidation peak were assigned as "stable", those higher than the most positive oxidation peak were considered "oxidizing", and those in between were called "passivating". These peak designations for WN were only used for pH < 6, because the oxidation profile for WN changed at higher pH.

The CVs for WN at pH 8.0 (Figure 3.2(e)) were representative of CVs observed for all WN samples at pH > 6. This change in oxidation profile compared to those at low pH was not surprising, considering previous reports of the oxidation behavior of tungsten carbide (WC) in

neutral pH[117,118] and tungsten metal at high pH.[119] In Figure 3.2(e), the initial anodic sweep of WN was similar to that of lower pH sweeps, but only one distinct oxidation peak was observed. On the subsequent cathodic sweep, an oxidative current response was observed with several distinct peaks. Subsequent CV cycles maintained current response at potentials below the onset of OER, which was unlike the results observed for WN at low-pH. Furthermore, in Figure 3.2(e), the anodic sweep of cycle 2 and all those subsequent cycles were unlike the anodic sweep of cycle 1. In contrast, the cathodic sweeps for all cycles were similar. This behavior was previously observed for metallic tungsten in alkaline pH, and the various oxidation peaks on the anodic and cathodic scans were attributed to formation and interchanging of various unstable hydroxylated tungsten species that formed a passivating layer on the electrode.[119] Interestingly, the XPS surface analysis post-CV (to 1.8 V_{RHE}) at pH 8.0 revealed a minimal oxidation of WN, with only a slight reduction of the N:W atomic ratio. This was in contrast to the observation that the nitrogen peak completely disappeared from WN at low pH after cycling to 1.8 V_{RHE} (Figure 3.3). This may be explained by the previous report that the unstable tungsten species were chemically dissolved at open circuit potential.[119] Despite the apparent preservation of the WN surface during CV sweeps, the passivation layer likely made the WN surface catalytically inactive. Therefore, potentials greater than the large oxidation peak of the first cycle for WN tested in pH > 6 were denoted as "oxidizing". No "passivating" region was denoted for WN samples at these pH values.

The pseudo-Pourbaix diagrams in Figure 3.4 revealed that NbN and WN were stable at all pH up to around 0.6 V_{RHE} and 1.0 V_{RHE}, respectively. This makes NbN a viable electrocatalyst support material for hydrogen evolution (-0.3 V_{RHE} to 0.0 V_{RHE}), hydrogen oxidation (0.0 V_{RHE} to 0.2 V_{RHE}) and CO_2 reduction (< -0.6 V_{RHE}). Similarly, WN should be suitable for the same reactions, with the addition of alcohol oxidation (0.5 V_{RHE} to 0.9 V_{RHE}).

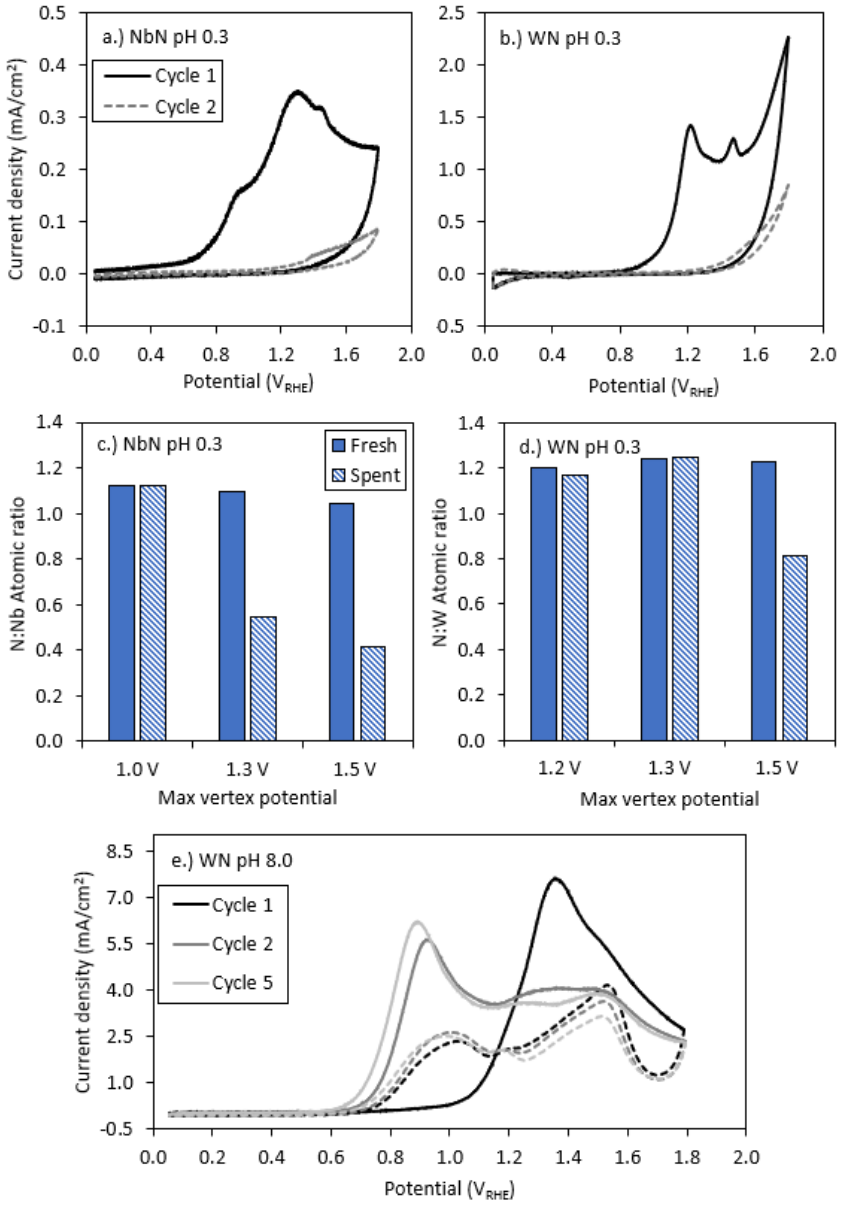

Figure 3.2 First 2 CV cycles for (a) NbN and (b) WN thin films in pH 0.3 electrolyte. The first cycle for each sample shows distinct oxidation peaks. For WN, these peaks are followed by current response from oxygen evolution reaction at potentials higher than 1.6 V_{RHE}. The oxidation peaks are not present on the second cycle. The atomic ratios of nitrogen-to-metal on the surface before and after cycling to various potentials are shown for (c) NbN and (d) WN. (e) WN thin film CVs at pH 8.0. The solid lines represent anodic

sweeps for each cycle and the dashed lines represent cathodic sweeps for each cycle. A constant scan rate of 50 mV s^{-1} was used. The oxidation currents observed in both directions are attributed to the formation and interchange of unstable hydroxylated tungsten species at the electrode surface.[119] A similar oxidation profile was observed for all WN samples tested at pH > 6.

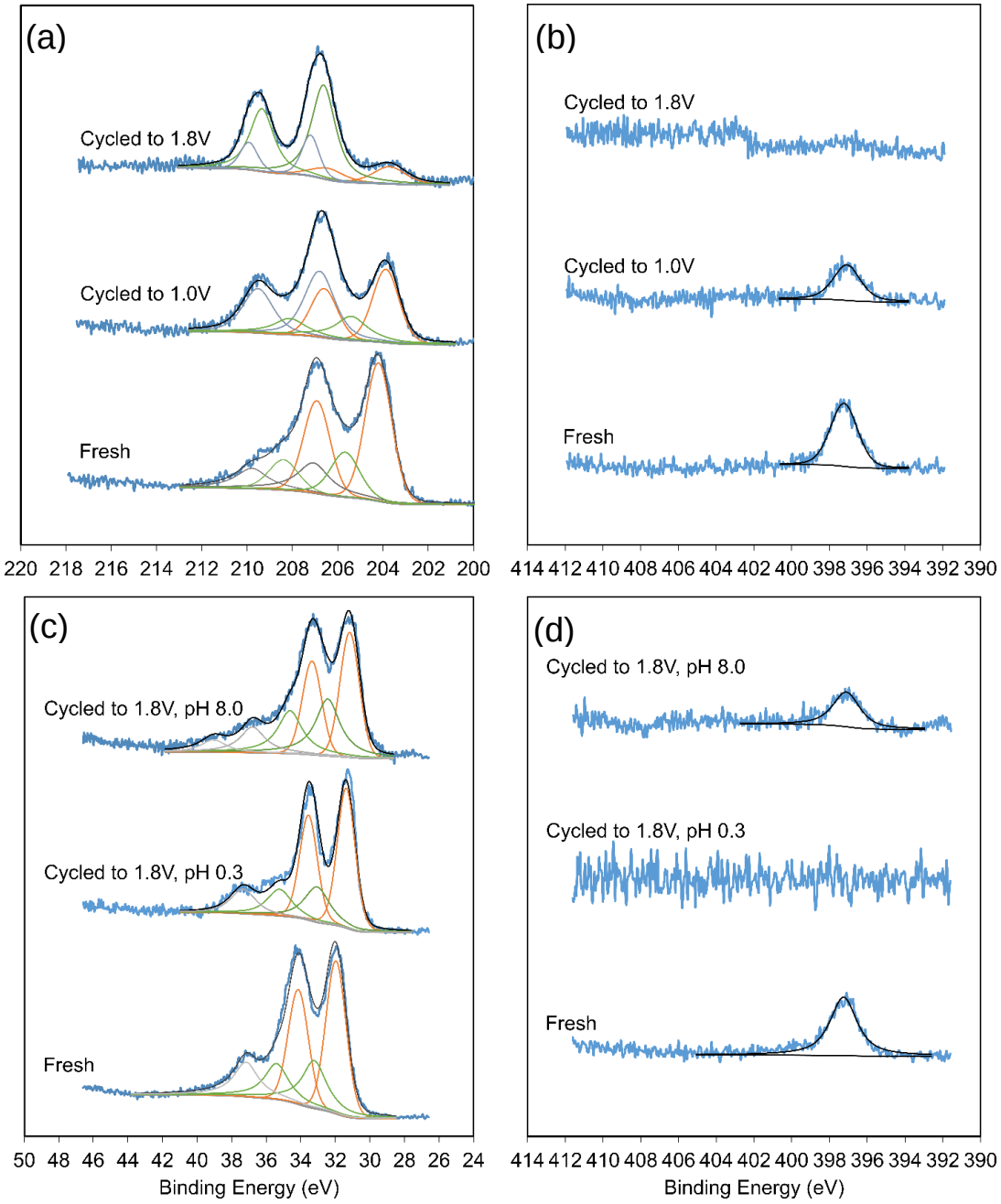

Figure 3.3 XPS spectra of NbN and WN before and after oxidation CVs. (a) Nb3d spectra and (b) N1s spectra for fresh NbN and after cycling to 1.0V and 1.8 V at pH 0.3. (c) W4f spectra and (d) N1s spectra for fresh WN and after cycling to 1.8 V in pH 0.3 electrolyte and cycling to 1.8 V in pH 8.0 electrolyte.

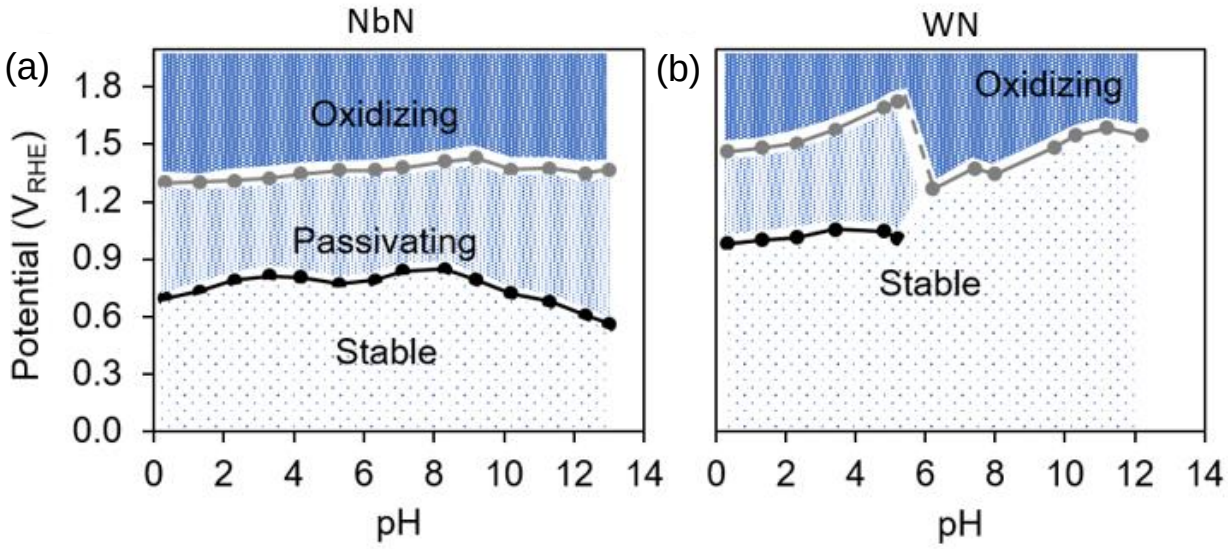

Figure 3.4 Pseudo-Pourbaix diagrams for (a) NbN and (b) WN thin films. Potentials below the black lines represent catalyst stability, where the nitride phase is preserved. Potentials above the gray lines represent catalyst oxidation. And potentials between the lines represent a passivating region where low-coordinated sites may be oxidized, but bulk oxidation was not observed. No passivating region was observed for WN films in pH > 6, due to its unique oxidation behavior at high pH.

3.3.3 HER Activity of Unmodified and Pt-Modified Nitride Films

Modifying transition metal nitride thin films with precious metal overlayers should enable close correlation with the model surfaces used in DFT calculations because the nitride surfaces are not contaminated with surface carbon, as is often the case with carbides. To test this hypothesis and to determine if transition metal nitrides are promising candidates to reduce Pt electrocatalyst loading,

Pt was deposited in sub-monolayer and monolayer (ML) coverages on WN and NbN thin films, and tested for HER activity. The deposition of Pt on both nitride surfaces occurred in a layer-by-layer fashion, as determined by the linear relationship between deposition time and measured Pt coverage (Figure 3.5). The HER was used as a probe reaction because the DFT-calculated hydrogen binding energy (HBE) is a known and effective descriptor of HER activity for TMC in both acid and alkaline electrolyte.[21]

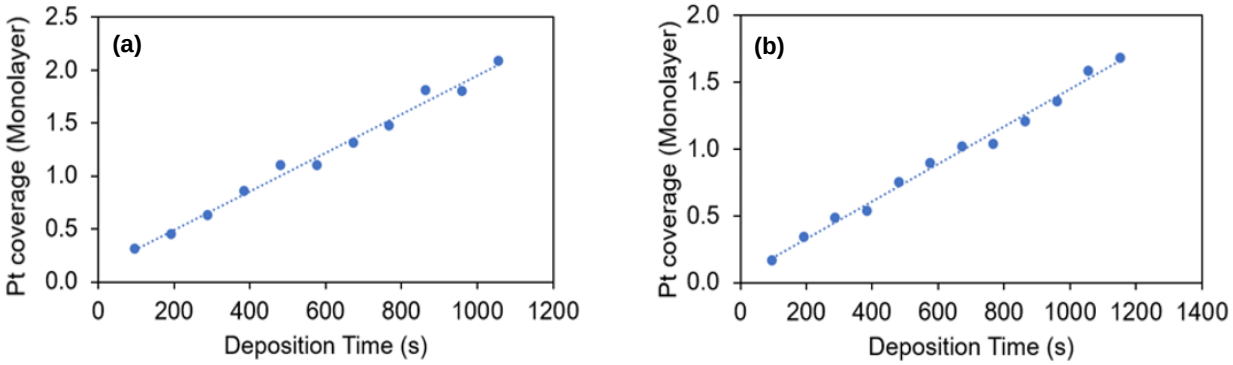

Figure 3.5 Pt growth on (a) NbN thin film and (b) WN thin film. The Pt coverage was determined using XPS peak area ratios. The linear relationship between Pt coverage and deposition time indicated layer-by-layer growth of Pt on NbN and WN.

Increasing Pt coverage on WN and NbN improved HER activity in acid electrolyte, shown in Figures 3.6(a) and 3.6(b). As the Pt coverage increased from 0.7 to 2.6 ML on WN, the HER polarization curves shifted anodically, and the curve for 2.6 ML Pt/WN overlapped with bulk Pt-foil. The same trend was seen with Pt on the NbN thin film in acid electrolyte, where the curve for 2.8 ML Pt/NbN essentially overlapped with bulk Pt foil (Figure 3.6(b)). Corresponding to the HER polarization curves in Figures 3.6(a) and 3.6(b), the overpotential losses at a cutoff current density of 5 mA cm^{-2} decreased as a function of Pt coverage (Table 3.1). This result was consistent with the DFT calculations of HBE and ΔG of Pt-modified nitrides, shown in Table 3.2. The HBE for the unmodified NbN(0001) and WN(111) surfaces were stronger (more negative) than the Pt(111)

surface, which indicated that unmodified NbN(0001) and WN(111) surfaces should have poor HER activity. In contrast, HBE values for ML Pt/NbN(0001) and Pt/WN(111) surfaces were much closer to that of the Pt(111) surface, which suggested Pt-like HER activity. The HBE and ΔG values for Pt(111) calculated for this work were consistent with values reported previously.[21,35] The △G calculations (Equation 3.3) described the free energy of the adsorbed intermediate, where △G = 0 eV represented the ideal reaction pathway for HER. DFT calculations were consistent with the trend in the experimental HER exchange current densities in acid (Figures 3.7(a) and 3.7(b)), determined from the linear portion of HER Tafel plots (Equations 2.8 and 2.10). The HER exchange current densities on bare nitrides were several orders of magnitude lower than the Pt foil, while those of ML Pt-modified nitrides in acid were similar to that of bulk Pt. Furthermore, XPS measurements before and after HER showed that the Pt coverage was stable on both nitrides in acid. Pt coverage on both nitrides decreased by about 20% after the initial testing but remained stable upon further testing (Figure 3.6(c)), indicating that the initial decrease was likely due to agglomeration of Pt instead of continuous dissolution.

In alkaline electrolyte, similar trends were observed, where increased Pt coverage on WN and NbN (Figures 3.6(d) and 3.6(e)) increased HER activity. However, even 2 or more ML Pt on WN or NbN did not result in HER activity approaching bulk Pt. The difference in activity between bulk Pt and Pt/WN or Pt/NbN in alkaline electrolyte was attributed to the instability of Pt overlayers on the nitride surface under these conditions. Unlike in acid, XPS revealed that Pt coverage continued to decrease after additional HER testing on both nitrides (Figure 3.6(f)). The alkaline activity trends were also reflected by the HER exchange current densities (Figures 3.7(c) and 3.7(d)), which were determined by fitting the linear portion of Tafel plots. However, once Pt coverage exceeded 1 ML on both nitrides in alkaline electrolyte, the Tafel plots were non-linear, possibly

due to Pt dissolution. Thus, exchange current densities calculated from these specific plots were not reliable. Calculations affected by this non-linearity were depicted in red in Figure 3.7. Additionally, the Tafel analysis used for samples in acid HER has been understood to represent diffusion limited current density, rather than the kinetic activity.[120] Thus, the trends depicted in Figure 3.7(a) and 3.7(b) were meant to show qualitative increase in HER activity of Pt-modified nitrides compared to bulk Pt.

These results showed that WN and NbN should be effective substrates to reduce Pt loading for HER in acid conditions, but may not be suitable for alkaline conditions due to instability of the Pt overlayer. Further studies are required to understand if Pt would be stable on other TMN in alkaline media, or if other precious metals would be stable on WN and NbN at high pH.

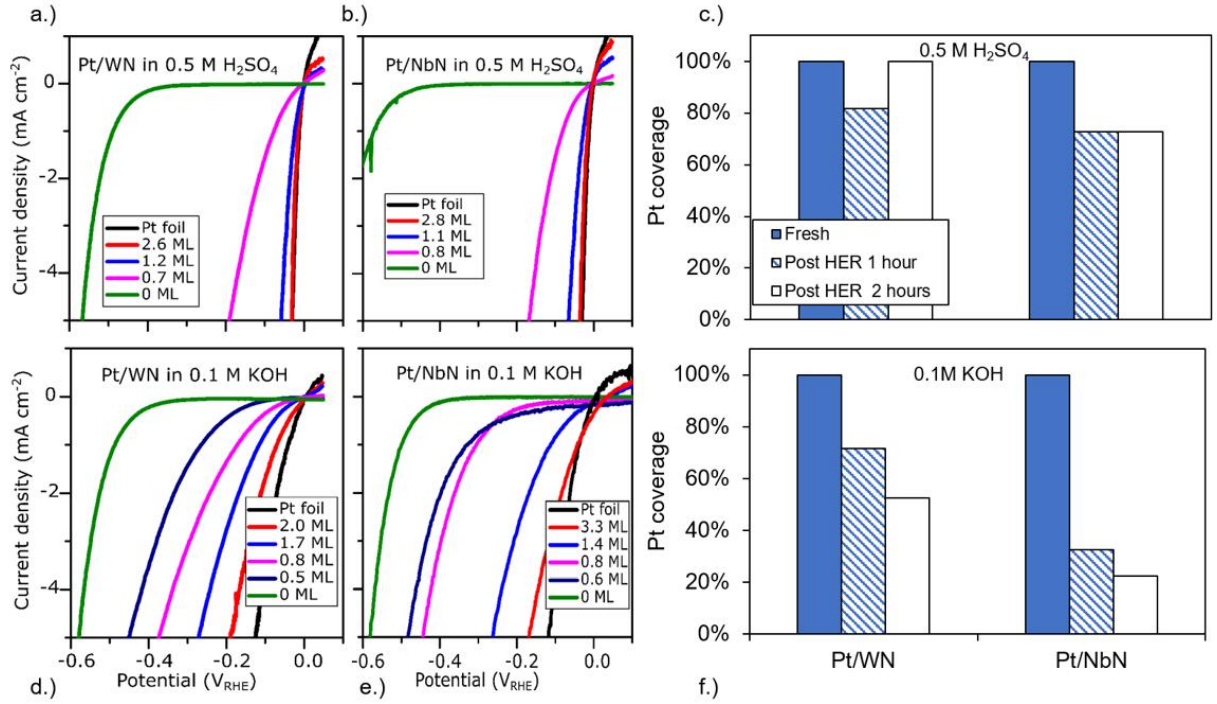

Figure 3.6 Hydrogen evolution reaction polarization curves for metal-modified nitride thin films. (a) Curves for Pt on WN in 0.5 M H_2SO_4. (b) Curves for Pt on NbN in 0.5 M H_2SO_4. (c) Pt coverage measured by XPS on WN and NbN thin films in acid. (d) Curves for Pt on

WN in 0.1 M KOH. (e) Curves for Pt on NbN in 0.1 M KOH. (f) Pt coverage measured by XPS on WN and NbN thin films in alkaline. Pt coverages were measured fresh, after HER testing for 1 hour, and after HER testing for 2 hours.

Table 3.1 Hydrogen evolution reaction overpotential at a cutoff current density of -5 mA cm^{-2}. Overpotentials were recorded directly from the HER polarization curves in Figures 3.6(a), 3.6(b), 3.6(d), and 3.6(e).

WN, 0.5 M H_2SO_4		NbN, 0.5 M H_2SO_4	
Pt-coverage	η (V_{RHE} @ -5 mA cm^{-2})	Pt-coverage	η (V_{RHE} @ -5 mA cm^{-2})
0 ML	-0.57	0 ML	-0.66
0.7 ML	-0.19	0.8 ML	-0.17
1.2 ML	-0.06	1.1 ML	-0.07
2.6 ML	-0.04	2.8 ML	-0.04
Pt foil	-0.03	Pt foil	-0.03
WN, 0.1 M KOH		NbN, 0.1 M KOH	
Pt-coverage	η (V_{RHE} @ -5 mA cm^{-2})	Pt-coverage	η (V_{RHE} @ -5 mA cm^{-2})
0 ML	-0.58	0 ML	-0.58
0.5 ML	-0.45	0.6 ML	-0.48
0.8 ML	-0.38	0.8 ML	-0.44
1.7 ML	-0.27	1.4 ML	-0.26
2.0 ML	-0.19	3.3 ML	-0.17
Pt foil	-0.12	Pt foil	-0.12

Table 3.2 DFT calculated binding energies and ΔG of adsorbed hydrogen on Pt(111), NbN(0001), WN(111), and ML Pt/NbN(0001) and Pt/WN(111) surfaces.

	Pt(111)	NbN(0001)	WN(111)	Pt/NbN(0001)	Pt/WN(111)
HBE (eV)	-0.46	-1.38	-0.83	-0.24	-0.38
△G (eV)	-0.26	-1.17	-0.63	-0.03	-0.18

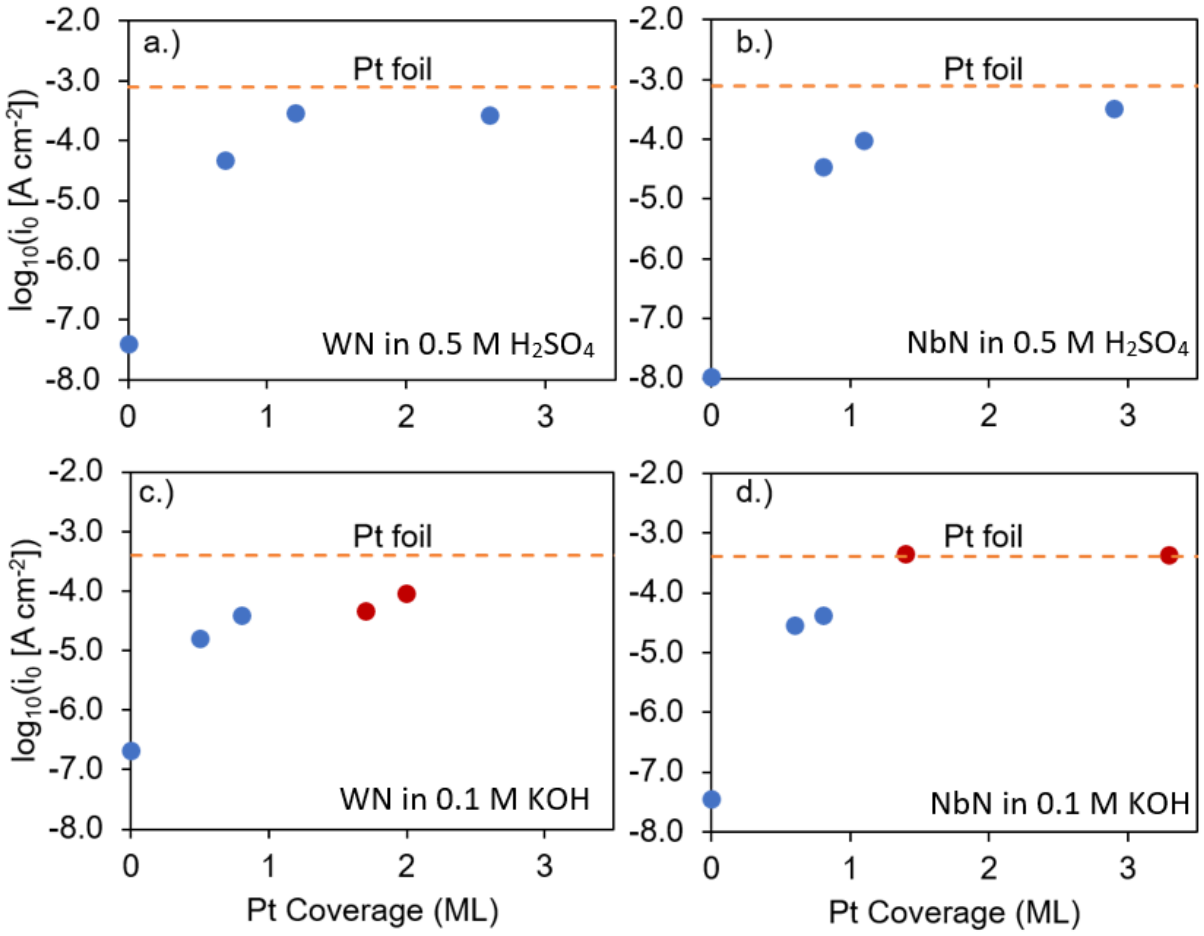

Figure 3.7 Hydrogen evolution reaction exchange current density as a function of Pt coverage on thin films of (a) WN in 0.5 M H_2SO_4, (b) NbN in 0.5 M H_2SO_4, (c) WN in 0.1 M KOH, and (d) NbN in 0.1 M KOH. Exchange current densities were extracted from Tafel plots, and red dots denote values that were extracted from Tafel plots with significant non-linearity, possibly due to Pt dissolution during HER.

3.4 Conclusions

This work shows the potential application of WN and NbN as promising electrocatalyst materials and presents a general methodology for evaluating the stability and activity of transition metal nitride thin films. WN and NbN were both synthesized as thin films with M_1N_1 stoichiometry by

annealing parent metal foils for 10 h at 1123 K in 100% ammonia at ambient pressure. Potential-pH stability regimes for both nitrides were established, and both should be stable under electrochemical conditions for hydrogen evolution/oxidation and CO_2 reduction, as well as alcohol oxidation for WN. Pt-modified WN and NbN thin films showed Pt-like HER activity in acid electrolyte, making them promising electrocatalysts to achieve a reduction in Pt loading while achieving similar HER activity as bulk Pt in low-pH electrolyte. The correlation between DFT calculations and HER activity showed that DFT could be an effective screening tool for metal-modified transition metal nitrides, similar to previous applications for carbide thin films. The Pt overlayer was not stable on either nitride at high pH conditions, and other combinations of metal-modified nitrides should be evaluated for applications in alkaline media.

3.5 Acknowledgements

I acknowledge Brian M. Tackett as a co-1st author, as well as Dong Tian and Dr. Kotaro Sasaki for their contributions to the DFT results and materials synthesis, respectively. This research was supported by the US Department of Energy, Office of Basic Energy Sciences, Catalysis Science Program (Grant No. DE-FG02-13ER16381). Brian M. Tackett acknowledges support from the U.S. Department of Energy, Office of Science, Office of Workforce Development for Teachers and Scientists, Office of Science Graduate Student Research (SCGSR) program. The SCGSR program is administered by the Oak Ridge Institute for Science and Education for the DOE under contract number DE-SC0014664. This chapter was adapted from *S. R. Denny, B. M. Tackett, D. Tian, K. and J. G. Chen, International Journal of Hydrogen Energy, 45(43) pp. 22883-22892, 2020.* No permission was necessary to reproduce sections of this publication for this thesis chapter.

Chapter 4: Investigating Platinum-Modified Molybdenum Nitride as an Ethanol Reforming Catalyst

4.1 Introduction

Biomass derived oxygenates are of interest both as fuels and building-blocks for commodity chemicals. Ethanol reforming in particular is an attractive pathway for renewable hydrogen production in the form of synthesis gas, or syngas, a CO/H_2 feedstock for Fischer-Tropsch (F-T) synthesis.[45] To utilize ethanol in this capacity, catalysts selective for C-C and C-H bond scission are essential. Surface science studies have revealed that ethanol reacts on platinum group metals (PGM) to form H_2 and CO, however some of these materials also produce undesired methane or lead to complete decomposition.[121–124] Of these, Pt is highly selective for the reforming pathway, and has been the focus of significant research efforts.[124–127] While Pt resources are geographically scarce and expensive,[19] supported Pt catalysts have been developed to effectively reduce precious metal loading and reduce cost.[128–130]

Transition metal carbides (TMC) of earth-abundant elements are a well-studied class of catalysts and catalyst support materials that are less expensive than PGMs.[129] Specific to the reaction of ethanol, past research on tungsten carbide (WC) and molybdenum carbide (Mo_2C) thin films demonstrated tunable bond scission and selectivity with the deposition of different admetals.[37,128] For example, while Mo_2C was reported to decompose ethanol into H_2, C_{ads}, and $O_{ads,}$ Ni-modification partially preserved the C-O bond which altered pathway selectivity from complete decomposition to reforming.[37]

Despite these interesting properties, TMC synthesis can result in the accumulation of undesired surface carbon that can decrease catalytic activity and lead to discrepancies between the experimentally relevant surface and the well-defined model surface used for density-

functional theory calculations.[68,69] In contrast to carbide analogues, transition metal nitrides (TMN) can be synthesized by the decomposition of NH_3, from which adsorbed N can desorb as N_2, resulting in inherently clean surfaces. Furthermore, TMNs show similar physical and electronic properties to carbide counterparts,[60,131] and have been studied as both catalysts and catalyst supports for several of heterogenous catalytic reactions.[90,106,132–138] In one study of methanol steam reforming, PGM/Mo_2N catalysts were shown to have greater overall activity and increased selectivity for H_2 production in place of CH_4 formation, in comparison to Mo_2C-supported analogs.[132] In a different study, Mo_2N was shown to interact more weakly with the oxygen atoms in a glycerol probe molecule in comparison to Mo_2C, which resulted in the production of allyl alcohol and propanal with some C-O bonds preserved, in addition to the fully deoxygenated propylene.[139]

In this work, these trends were further explored by investigating the reaction of ethanol on unmodified and Pt-modified Mo_2N thin films using surface science techniques. Under ultrahigh vacuum (UHV) conditions, temperature programmed desorption (TPD) experiments were employed to identify the gas-phase reaction products, as well as to quantify the reaction activity and selectivity. High resolution electron energy loss spectroscopy (HREELS) was employed to further understand the reaction intermediates present on the surface, which informed the nature of C-C, C-O, and C-H bond scission. This study demonstrates that Mo_2N can be effectively tuned from the ethanol decomposition to reforming pathway with the addition of a Pt admetal, offering a potential strategy to utilize TMNs as support materials to reduce Pt loading and allow for better correlation between experiment results and first-principles calculations.

4.2 Methods

4.2.1 Nitride Synthesis

Mo_2N thin films were synthesized from 0.1 mm thick Mo (Alfa Aesar, 99.95%) cut into 1 cm x 2 cm rectangles. Cut foils were cleaned using a previously described procedure which utilized a series of sonication and wash steps to remove surface oils and oxides prior to being loaded into a horizontal quartz tube furnace.[24,70] Nitride thin film synthesis was also adapted from a prior study.[70] In brief, the furnace was ramped from 298 K to 1123 K at a linear rate over 2 hours with an ambient pressure gas flow of 150 standard cubic centimeters (sccm) of 100% ammonia. The furnace dwelled at 1123 K for 10 hours, after which the synthesized nitride thin films gradually cooled to ambient temperature under the same gas condition. Once cooled to room temperature, the furnace was purged with Argon and the films were removed. In a previous study that used the same synthesis procedure, the as-synthesized Mo_2N films were characterized using X-ray photoelectron spectroscopy to quantify the Mo:N atomic ratio, as well as symmetric and glancing incidence X-ray diffraction to confirm the nitride phase.[139]

4.2.2 Surface Science Experiments

TPD experiments were conducted in a UHV chamber equipped with Auger electron spectroscopy (AES) for surface analysis, mass spectrometry (MS) for product detection, a Ne^+ sputter gun for surface cleaning, and a Pt metal source for physical vapor deposition (PVD). The UHV chamber had a base pressure of 7.0×10^{-10} Torr. The Mo_2N foil or Pt(111) single crystal was spot welded to two 0.7 mm tungsten posts (Alfa Aesar, 99.95%) that were resistively heated and cooled by contact with a liquid N_2 reservoir opposite the feedthrough. Temperature was measured by a type K thermocouple spot welded to a single point on the back of the sample. The Pt(111) single crystal and Mo_2N film were cleaned using the same methodology as a past surface

science study of Pt(111).[124] The sample cylinder was prepared by transferring ethanol (Sigma-Aldrich, 99.5%) into an evacuated glass cylinder in an Argon gas environment via a glove bag. The reagent then underwent 4 freeze-thaw-pump cycles for further purification.

The Pt overlayer was deposited by PVD and the coverage was quantified by AES. During deposition, the cleaned surface was held at 300 K. PVD employed the resistive heating of a 0.1 mm Pt (Alfa Aesar, 99.997%) wire wrapped around a 0.5 mm tungsten filament (Alfa Aesar, 99.95%), mounted in a tantalum shield. The AES atomic ratio of Pt(62 eV) and Mo(186 eV) were used to calculate Pt coverage.[140]

For TPD experiments, 4 L (1 L = 1 x 10^{-6} Torr·s) ethanol was dosed while the sample was held at 200 K.[124] The sample directionally faced the gas inlet for dosing and was positioned in front of the MS for the duration of the TPD experiment. Once cooled to a base temperature of 110 K, the sample temperature was ramped at a constant rate of 3 K/s to 850 K.[37,124,128] Gas-phase ethanol reaction products were identified using the MS, based on preselected atomic mass units (amu) in accordance with gas cracking patterns. AES measurements were performed to monitor the surface composition before and after the TPD experiments. Quantification of the activity and selectivity accounted for calculated MS and reported ion gauge (IG) sensitivity factors, and was based on a previously reported C_2H_4 decomposition method.[141]

HREELS experiments were conducted in a similarly equipped UHV chamber with the addition of HREELS. The base chamber pressure was 1.0 x 10^{-9} Torr. The surface was prepared using the same procedures for cleaning, PVD, and dosing as described for TPD experiments. For thermal sequencing experiments, the surface was ramped to the desired temperature and cooled to less than 200 K prior to conducting the HREELS scan.

4.3 Results and Discussion

4.3.1 Identification and Quantification of Gas-Phase Products using TPD

TPD experiments of ethanol on Mo_2N, Pt/Mo_2N, and Pt(111) were conducted to identify the gas-phase reaction products, and quantify the catalytic activity and selectivity. Figure 4.1 shows the TPD spectra of select gas-cracking patterns representative of reaction products. Specifically, the panels in Figure 4.1 correspond to (a) H_2 (2 amu), (b) CO (28 amu), (c) C_2H_4 (27 amu), and (d) CH_4 (16 amu). On all surfaces tested, the reaction products were attributed to a combination of four reaction pathways:

Reaction 4.1 Ethylene production $$aC_2H_5OH \rightarrow aO_{ads} + aC_2H_4 + aH_2$$

Reaction 4.2 Methane production $$bC_2H_5OH \rightarrow bCO + bCH_4 + bH_2$$

Reaction 4.3 Reforming $$cC_2H_5OH \rightarrow cC_{ads} + cCO + 3cH_2$$

Reaction 4.4 Complete decomposition $$dC_2H_5OH \rightarrow dO_{ads} + 2dC_{ads} + 3dH_2$$

On unmodified Mo_2N, H_2 was the main reaction product. H_2 desorbed in an initially sharp peak at 404 K that extended into a 200 K broad peak, which suggested that various reaction intermediates underwent further decomposition (Figure 4.1(a)). Peaks associated with the desorption of C_2H_4, CO, and CH_4 were also observed on the Mo_2N surface, but with lower peak areas. The peak at 480 K in Figure 4.1(b) is attributed to C_2H_4, which has an overlapping gas cracking pattern with CO at 28 amu. The reaction products of ethanol on Mo_2N were similar to those reported on Mo_2C/Mo(110), where H_2 generation was dominant.[37] This likely indicated that the Mo_2N surface was similar to the Mo_2C analogue in that the surface was active for the scission of C-C, C-O, and C-H bonds.

The addition of Pt at sub-ML and ML coverages on Mo_2N shifted the peak intensities and the composition of the detected gas-phase products. Specifically, in Figure 4.1(c) C_2H_4 did not desorb from Pt-modified surfaces, and in Figure 4.1(d) the CH_4 peak intensity decreased as a function of Pt coverage. H_2 peaks were broad on all Mo_2N surfaces. The deposition of Pt significantly increased CO production. The onset temperature of CO desorption increased with Pt coverage, from Pt/Mo_2N to Pt(111), in agreement with previously reported trends of ethanol reacted on Pt/WC and polycrystalline Pt foil.[128]

Table 4.1 summarizes the quantified activity and reaction (4.1) – (4.4) selectivity of each of the four surfaces studied. Because multiple reaction pathways produced overlapping gas-phase products, specifically H_2 and CO, the reaction pathway stoichiometry was used to quantify activity and selectivity. In brief, following the decomposition of C_2H_4 on Mo_2N and Pt(111), the C(273 eV)/Mo(186 eV) AES peak-to-peak ratio and H_2 desorption peak intensity were used as the basis for calculating product yield. An example calculation of CH_4 yield follows:

Equation 4.1
$$CH_4\ yield = b = \frac{\theta_{C_2H_4}}{P_{H_2}}\ P_{CH_4}^{C_2H_5OH}\ \frac{S_2^{H_2}}{S_{16}^{CH_4}}$$

where $\theta_{C_2H_4}$ was the C/Mo AES ratio from C_2H_4 decomposition, P_{H_2} was the H_2 peak area from C_2H_4 decomposition, $P_{CH_4}^{C_2H_5OH}$ was the CH_4 peak area from C_2H_5OH decomposition, and $\frac{S_2^{H_2}}{S_{16}^{CH_4}}$ was the ratio of the H_2 and CH_4 combined IG and MS sensitivity factors. This calculation was used to quantify the yield of other products, and the remaining stoichiometric variables were deduced as:

$$C_2H_4\ yield = a$$

$$CO\ yield = b + c \quad \rightarrow \quad c = CO\ yield - b$$

$$H_2\ yield = a + b + 3c + 3d \quad \rightarrow \quad d = \frac{(H_2\ yield - a - b - 3c)}{3}$$

The quantification results presented in Table 4.1 revealed that Pt-modification of the Mo_2N surface resulted in tunable selectivity, where complete decomposition could be suppressed in place of reforming. The gas-phase H_2 desorption peak from the unmodified Mo_2N was primary attributed to the complete decomposition pathway, with a selectivity of 93%. This result was consistent with past studies of the decomposition of ethanol and other oxygenates on Mo_2C, where C-O bond scission activity was attributed to the strong oxophilicity of Mo_2C.[37,142] This property likely extends to the Mo_2N surface to some degree, as indicated by the pathway selectivity reported in Table 4.1. The addition of sub-monolayer Pt markedly shifted pathway selectivity from complete decomposition to reforming, and the ethanol reforming selectivity of the 1.1 ML Pt/Mo_2N and Pt(111) surfaces were nearly identical. These results demonstrated that even with low Pt coverage, C-O bond scission on the Mo_2N surface was suppressed.

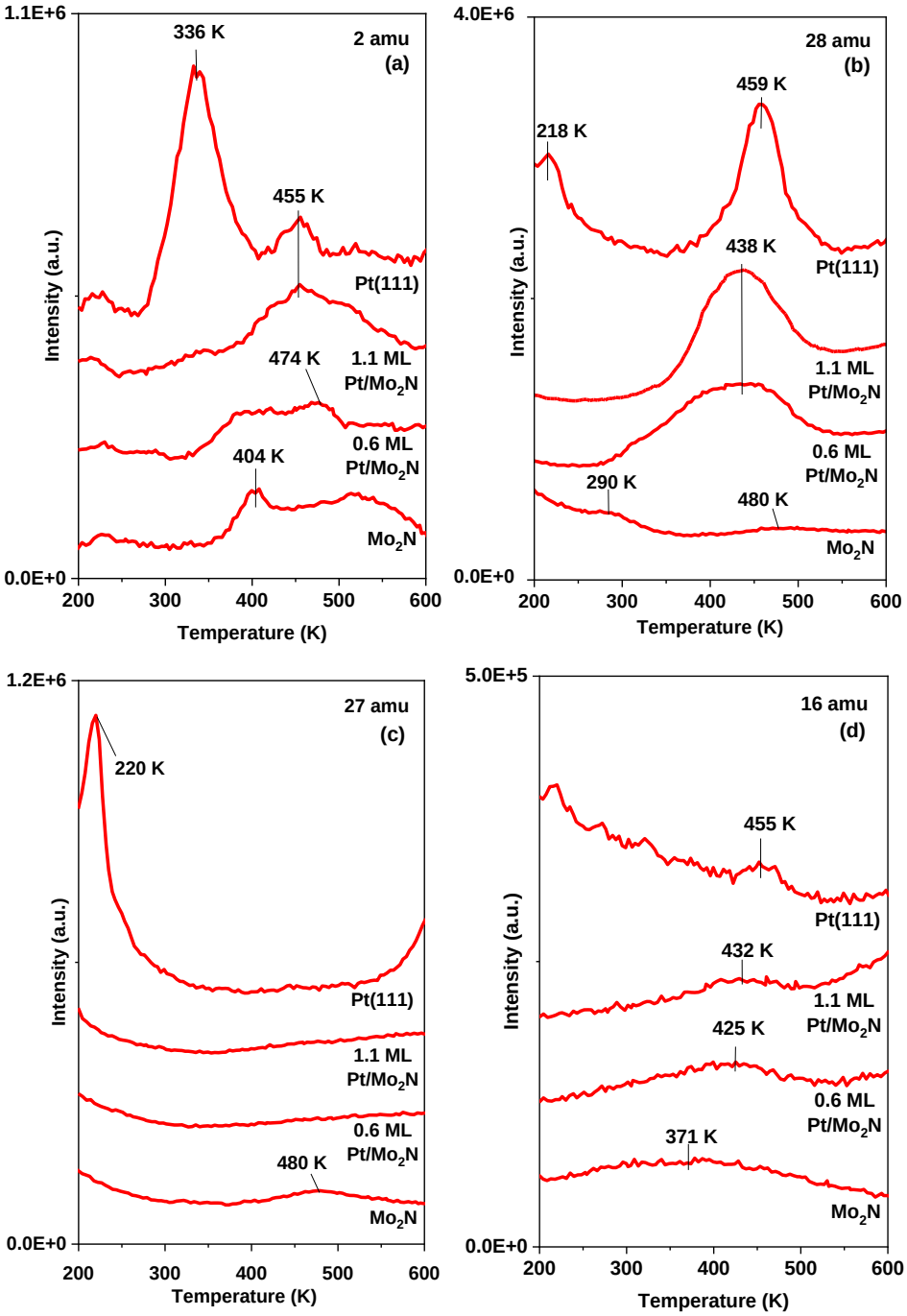

Figure 4.1 TPD spectra of ethanol decomposition on Mo_2N, Pt-modified Mo_2N, and Pt(111) surfaces. Reaction products (a) 2 amu, H_2; (b) 28 amu, CO; (c) 27 amu, C_2H_4; (d) 16 amu, CH_4.

Table 4.1 Activity and reaction pathway selectivity of ethanol on Mo_2N, Pt-modified Mo_2N, and Pt(111).

	Activity (molecules/metal atom)					**Selectivity** (%)			
Surface	Ethylene (a)	Methane (b)	Reforming (c)	Decomposition (d)	Total	Ethylene (a)	Methane (b)	Reforming (c)	Decomposition (d)
Mo_2N	0.010	0.004	0	0.185	0.199	5	2	0	93
0.6 ML	0	0.003	0.128	0.033	0.164	0	2	78	20
1.1 ML	0	0.002	0.146	0.010	0.158	0	1	93	6
Pt(111)	0	0.000	0.027	0.001	0.028	0	1	95	4

4.3.2 Identification of Surface Reaction Intermediates using HREELS

HREELS was used to identify surface intermediates to further understand the different reaction pathways on four surfaces: Mo_2N, 0.4 ML Pt/Mo_2N, 1.0 ML Pt/Mo_2N, and Pt(111). Figure 4.2 shows the HREEL spectra of adsorbed and reacted ethanol on the unmodified Mo_2N surface. Figure 4.4 shows the spectra of all four surfaces dosed with 4 L ethanol at 200 K, and heated to 350 K and 500 K. As noted in the Methods section, HREELS experiments were conducted after the surface had cooled to less than 200 K. The assignments to the vibrational modes are reported in Table 4.2.

On the Mo_2N surface, the characteristic vibrational modes of ethoxy were present after adsorption of ethanol at 200 K (Figure 4.2). These vibrational modes (frequency, cm^{-1}) can be summarized as follows: ν_s(CCO) and ν_{as}(CCO) at 908 cm^{-1} and 1107 cm^{-1}, $\delta(CH_3)$ and $\delta(CH_2)$ at 1377 cm^{-1} and 1470 cm^{-1}, and $\nu(CH_3)$ at 2928 cm^{-1}. When ethanol was dosed at 200 K, the O-H stretching mode was not observed, which indicated that ethanol did not adsorb molecularly and OH bond scission occurred upon adsorption. HREELS results after dosing 1 L and 4 L ethanol on unmodified Mo_2N at 120 K showed that ethanol molecularly adsorbed to the surface (Figure 4.3). Vibrational mode assignments match those reported in Table 4.2, with the addition of ν(OH) at 3281 cm^{-1} present on the 120 K dosed surface. This vibrational mode is attributed to the -OH stretching mode of molecularly adsorbed ethanol, consistent with past literature on

analogous Mo_2C surfaces.[37] In Figure 4.2, upon heating the surface to 300 K the vibrational modes associated with *ν*(CCO) decreased in intensity, which indicated initial decomposition of the of the ethoxy intermediate. Upon further heating to 350 K and 400 K, deformation modes associated with CH_2 and CH_3 bonds also decreased, consistent with the H_2 desorption peak at 404 K from the TPD experiments. Furthermore, as the temperature was increased to 600 K, poorly defined C_xH_y fragments from ethoxy decomposition remained on the surface as indicated by peaks in the characteristic frequency range. A *ν*(CO) vibrational mode was not observed on the Mo_2N surface, which is consistent with the TPD results that there was not significant CO desorption from the surface. Evidenced by the HREELS results, Mo_2N was active for C-C, C-H, and C-O bond scission, and the ethoxy intermediate decomposed without the formation of adsorbed species containing *ν*(CC) or *ν*(CO) vibrational modes.

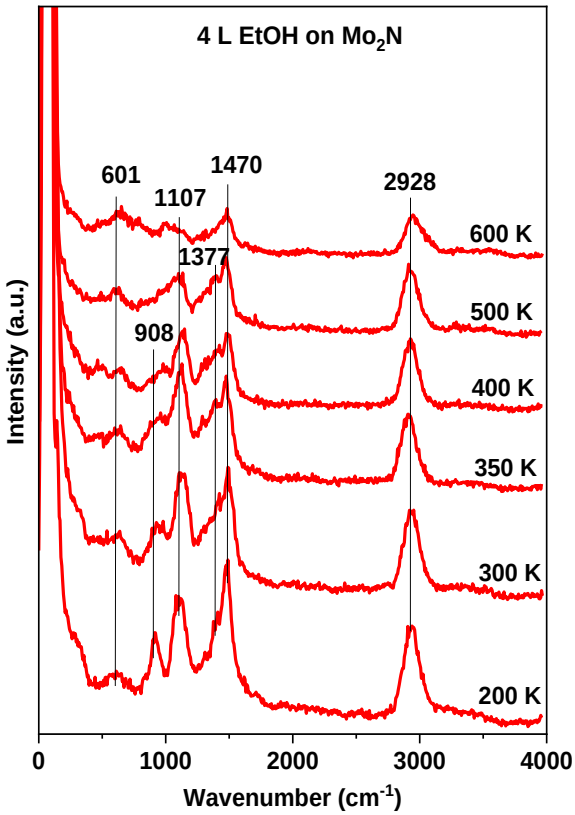

Figure 4.2 HREEL spectra of 4 L ethanol dosed at 200 K on Mo_2N.

Table 4.2 Vibrational mode assignments of ethanol on Mo_2N, Pt-modified Mo_2N, and Pt(111).

Ethanol HREELS assignments, frequency (cm^{-1})					
Mode	Solid Phase[a]	Mo_2N	Mo_2C/Mo(100)[b]	Pt(111)	Pt(111)[c]
δ (CCO)	419				450
γ (CH_2)	801			793	800
ν_s (CCO)	885	908	873	908	880
ρ (CH_3)	1033				
ν_{as} (CCO)	1089	1107	1055	1107	1060
δ (OH)	1241				
δ (CH_3)	1394/1452	1377	1366	1386	1390
δ (CH_2)	1490	1470	1448	1470	1450
ν (CH_2)	2900				
ν (CH_3)	2943/2989	2928	2936	2957	2960
ν (OH)	3676		3430		3230

δ, deformation*; ν*, stretching*; ρ,* rocking; *s*-symmetric; *as*-asymmetric. [a]Ref[143]. [b]Ref[37]. [c]Ref[125].

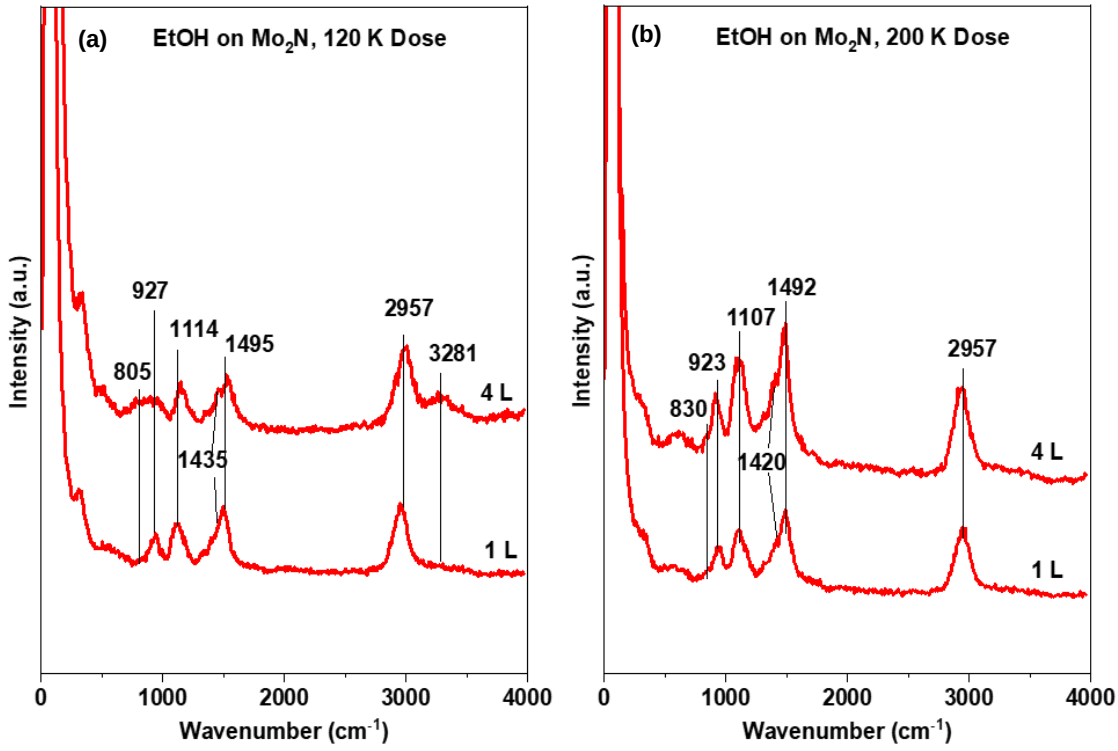

Figure 4.3 HREEL spectra of 1 L and 4 L ethanol dosed on unmodified Mo_2N surfaces at (a) 120 K and (b) 200 K.

The HREEL spectra at the ethanol adsorption temperature of 200 K and spectra of 350 K and 500 K of the Mo_2N, 0.4 ML Pt/Mo_2N, 1.0 ML Pt/Mo_2N, and Pt(111) surfaces showed distinct differences in the reaction intermediates present on the surface. In Figure 4.4(a), the vibrational modes associated with the adsorption of ethanol on the four surfaces were different. Specifically, on Mo_2N the vibrational modes associated with ν(CCO) were well-resolved and there was no observed CO stretching mode. On the 0.4 ML Pt/Mo_2N surface, the ν(CCO) modes were less-resolved and there were two distinct CO stretching modes at 1917 cm^{-1} and 2070 cm^{-1} attributed to CO adsorbed on different sites. This result was consistent with the broad CO TPD peak detected on the 0.6 ML Pt/Mo_2N surface. As Pt-coverage increased to 1.0 ML Pt/Mo_2N, the ν(CO) mode at 2070 cm^{-1} and Pt-O at 542 cm^{-1} were detected, consistent with vibrational modes present on the Pt(111) surface. The second ν(CO) mode was no longer detected on the 1.0 ML surface, consistent with the desorption of CO from a single site and a narrowed CO TPD peak from the 1.1 ML Pt/Mo_2N surface. After the surfaces were heated to 350 K the ν(CCO) modes decreased in intensity, which indicated partial decomposition of the ethoxy intermediate on all surfaces. In contrast to Pt-modified Mo_2N and Pt(111) surfaces, ν_s(CCO) and ν_{as}(CCO) at 908 cm^{-1} and 1107 cm^{-1}, and $\delta(CH_3)$ and $\delta(CH_2)$ at 1377 cm^{-1} and 1470 cm^{-1} remained relatively intense on the Mo_2N surface. The intensity of these vibrational modes suggested that the intermediates were less decomposed on the Mo_2N surface. Upon further heating of the surfaces to 500 K, the vibrational modes attributed to the decomposed ethoxy intermediate disappeared on Pt-modified Mo_2N and Pt(111) surfaces. The intensity of the CO stretching mode also decreased, which was consistent with the desorption of CO from each of these surfaces. In agreement with the TPD results, the HREELS experiments indicated that Pt-modification at sub-ML and ML coverages substantially altered the reaction intermediates present on the surface, and hence the

reaction pathway.

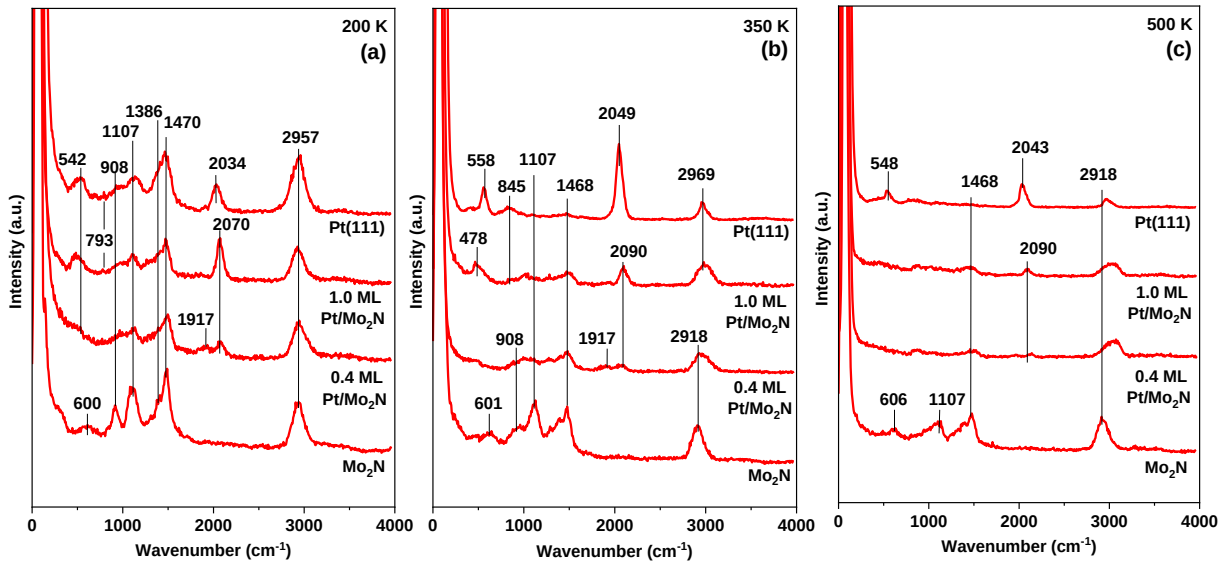

Figure 4.4 HREELS spectra of 4 L ethanol dosed at 200 K on Mo_2N, Pt-modified Mo_2N, and Pt(111) surfaces. Temperature profiles presented at the adsorption temperature 200 K, and ramped temperatures 350 K and 500 K.

4.4 Conclusions

This work presents the first surface science investigation of Mo_2N and Pt-modified Mo_2N for the reaction of ethanol. TPD experiments revealed the surface-dependent reaction of ethanol to C_2H_4, CH_4, CO, and H_2. On the Mo_2N surface, ethanol primarily underwent complete decomposition through the scission of C-C, C-O, and C-H bonds, consistent with reported bond scission activity on Mo_2C surfaces.[37] Minor CH_4 and C_2H_4 gas-phase products desorbed from the Mo_2N surface, but did not account for a substantial portion of the reacted ethanol. While unmodified Mo_2N primarily decomposed ethanol, Pt-modification shifted the reaction pathway from complete decomposition to reforming, which left the C-O bond intact. HREELS was used to further understand the reaction intermediates on surface, and elucidate the shift in the reaction selectivity associated with Pt-modification from the TPD experiments. Specifically, HREELS

results revealed that the C-O bond was preserved as the ethoxy intermediate decomposed on Pt-modified surfaces, as evidenced by the presence of the *ν*(CO) mode. In combination, the HREELS and TPD results indicated that ethanol reacted on the 1.0 ML Pt/Mo_2N surface had similar reaction intermediates and selectivity to Pt(111). This work highlights the potential of TMN materials as supports for the tunable and selective reforming of biomass-derived oxygenates, as well as a strategy to decrease precious metal loading for the generation of renewable syngas.

4.5 Acknowledgments

This research was supported by the US Department of Energy, Office of Basic Energy Sciences, Catalysis Science Program (Grant No. DE-FG02-13ER16381). I acknowledge Dr. Zhexi Lin for his contribution to the HREELS results and Dr. Brian M. Tackett for the synthesis of the Mo_2N thin films.

Chapter 5: Mechanistic Insights into the Active Sites on WO_x/Pt(111) for Glycerol Deoxygenation Reactions

5.1 Introduction

Over the past several decades, the conversion of lignocellulosic biomass into useful fuels and chemicals has attracted considerable research attention.[52,144–148] Biomass conversion is a promising approach to produce renewable chemicals and fuels that could help to alleviate some of the environmental issues associated with conventional methods of production.[149–151] One critical step in the upgrading of biomass often involves the selective removal of excess oxygen in biomass-derived molecules. The presence of excess oxygen not only reduces the heat value of the molecules, but also creates opportunities for side reactions that can lead to undesirable products.[146] The removal of oxygen can be achieved by means of decarbonylation, decarboxylation, dehydration, and HDO.[152] While decarbonylation and decarboxylation result in the undesired loss of carbon,[88] dehydration and HDO reactions are more favorable because oxygen can be selectively without breaking the C-C/C=C bonds. Many catalysts have been studied for the dehydration and HDO reactions of biomass derivatives. Metal oxide catalysts contain acid sites that are highly selective toward dehydration.[49,52,153–155] Bimetallic and transition metal carbide catalysts have been shown to selectively catalyze HDO reactions.[44,156–161] Among these catalysts, Pt/WO_x and its inverse oxide WO_x/Pt are particularly interesting in that they contain active sites for both dehydration and HDO reactions.[49,161] Pt/WO_x-based catalysts have been studied extensively for the HDO/hydrogenolysis reaction of glycerol in the liquid phase.[46,48,162–168] It has been proposed that the bifunctionality of the catalyst plays an important role in the selective conversion of glycerol into 1,3-propanediol.[48,167,168] In this reaction, the Pt site dissociates H_2 into H atoms, which spill over to the WO_x site to form

hydroxyl groups in situ. In one study, such in situ formed hydroxyl groups were found to be more active than those originally present on the WO_x site.[48] In another study, Wang et al. showed that the oxygen vacancies on Pt-WO_x/C were highly selective toward the HDO reaction of m-cresol.[161] It has also been demonstrated that the WO_x-covered Pt sites resulting from strong metal-support interaction served as the active sites for the ring-opening of tetrahydrofurfuryl alcohol.[57]

Despite the interesting reactivity of Pt/WO_x and WO_x/Pt, and in contrast to the extensive studies conducted on powder catalysts, there have been relatively few studies on single crystal model surfaces that investigate the nature of the active sites on a model surface. Chen et al. studied the HDO reaction of m-cresol on a WO_x/Pt(111) surface, and revealed the interaction between Pt and WO_x that stabilized the active sites for the reaction.[169] Lin et al. investigated the reactions of isopropyl alcohol (IPA) on WO_x/Pt(111) and identified the dehydrogenation sites Pt and the dehydration sites on WO_x.[49] However, neither of these studies focused on elucidating the simultaneous existence of multiple types of deoxygenation active sites, which are highly important for the upgrading of biomass-derive oxygenates. In this work, a combination of TPD and HREELS techniques were used to elucidate the various deoxygenation active sites and reaction mechanisms on a WO_x/Pt(111) model surface. Glycerol was chosen as a model compound due to its multiple hydroxyl groups that potentially allowed it to interact differently with the different deoxygenation sites on the surface. It is worth noting that the reactivities of glycerol under ultrahigh vacuum (UHV) conditions are not necessarily the same as those in the liquid phase, as shown in a previous study that used glycerol as a model molecule to reveal Lewis and Brønsted acid sites on niobia.[42] In the current study, the use of glycerol also allowed the differentiation of different active sites on WO_x/Pt(111). TPD results showed that three types

of active sites existed on the surface: Pt sites for reforming, Brønsted acid WO_x sites for dehydration to produce acrolein, and oxygen vacancy WO_x sites for HDO to form propylene. HREELS observations indicated that glycerol interacted with Pt(111) strongly and underwent the reforming pathway and further decomposition. On WO_x-modified Pt(111) surfaces, glycerol bonded to the surface through its oxygen atoms. Two types of W-O bonds were observed with different relative intensity ratios on 0.7 monolayer (ML) and above-ML WO_x/Pt(111), likely corresponding to the two WO_x coverage-dependent oxygen removal pathways on WO_x-modified Pt(111) surfaces from TPD experiments.

5.2 Methods

All TPD experiments were conducted in a UHV chamber described previously.[49] The preparation procedure for the Pt(111) and WO_x-modified Pt(111) surfaces were the same as that used in our previous work.[49] Briefly, the synthesis of the WO_x/Pt(111) surfaces involved exposing a Pt(111) single crystal to a heated $W(CO)_6$ source, followed by oxidation. The prepared surface was exposed to a desired amount of reactant and was heated at 3 K/s in front of a mass spectrometer (UTI-100C). The surface elemental composition was monitored during the synthesis procedure as well as before and after the TPD experiments. HREELS experiments were performed in a separate UHV chamber documented elsewhere.[44] The prepared surface was exposed to a desired amount of reactant at 200 K before the first spectrum was taken. Subsequent spectra were recorded after the surface was heated to desired temperatures and cooled to below 200 K.

5.3. Results and Discussion

5.3.1 TPD Studies of Reaction Products

In order to probe the different kinds of WO_x sites, TPD experiments were conducted using glycerol as a probe molecule. The multiple hydroxyl groups of glycerol open the possibility for different C-O bond cleavage pathways to happen on different active sites. Based on the TPD results, three distinct sites were identified, including the Pt site and two types of WO_x sites present on WO_x. Figure 5.1 shows the desorption of hydrogen, carbon monoxide, acrolein, and propylene from Pt(111) and WO_x/Pt(111) with different WO_x coverages. Unreacted glycerol desorbed at an onset temperature around 250 K, with a peak temperature of 280 K. The sharp peaks at around 280 K were attributed to either the cracking pattern of glycerol or crosstalk in the mass spectrometer associated with the glycerol cracking pattern. From Figure 5.1(a) and (b), on Pt(111), H_2 and CO desorption was observed with a peak temperature of 383 K, suggesting that glycerol underwent the reforming pathway. As the WO_x coverage was increased, the H_2 and CO peak areas decreased. On the surface with WO_x coverage greater than 1 ML, no significant amount of H_2 or CO desorption was observed. These results indicated that the reforming pathway was favored on the Pt sites, but not on the WO_x sites.

Figure 5.1(c) shows the desorption of acrolein from the corresponding surfaces. On surfaces with WO_x coverage less than 0.7 ML, no significant amount of acrolein was formed. Nonetheless, on 0.7 ML WO_x/Pt(111), an acrolein desorption peak centered at 622 K was observed. As the WO_x coverage was increased to above 1 ML, the peak area of acrolein increased, and the peak temperature shifted to 530 K, indicating that the dehydration pathway to form acrolein was preferred on the WO_x site. It was likely that the Brønsted acid sites (hydroxyl groups) on WO_x catalyzed the dehydration pathway, as demonstrated in a previous study.[49]

Acrolein was formed after two molecules of water was removed from glycerol, which was also observed on nobia previously.[42] Shown in Figure 5.1(d) is the desorption of propylene from the corresponding surfaces. Similar to the desorption of acrolein, no significant amount of propylene desorbed from surfaces with a WO_x coverage less than 0.7 ML. When the WO_x coverage was increased to 0.7 ML, a propylene peak centered at 462 K appeared. The formation of propylene followed the HDO pathway, in contrast to the dehydration pathway that produced acrolein. As the WO_x coverage was further increased to above 1 ML, the peak temperature shifted to 506 K. Consistent with previous studies, the shift of the peak temperature to a higher value indicated that that the WO_x/Pt(111) interface facilitated the HDO pathway,[161,169] in comparison to the dehydration pathway that was more favorable on a surface fully covered by WO_x.[49] The shift of peak temperature of the dehydration and HDO pathways in opposite directions further suggested that these two pathways were catalyzed by two distinct sites.

Based on the glycerol TPD experiments, three distinct sites were identified, as shown in Scheme 5.1. On Pt sites, glycerol underwent the reforming reaction to form H_2 and CO. On the Brønsted acid sites on WO_x, glycerol was dehydrated to form acrolein. Glycerol could also undergo the HDO reaction to produce propylene on another type of active sites associated with the WO_x/Pt(111) interface. These sites possibly originated from the oxygen vacancies on WO_x, which were enhanced by Pt, as suggested by previous studies.[161,169] The quantification results of the product concentration from each pathway are shown in Table 5.1. It is clear that CO concentration decreased with the increase of WO_x coverage, and that more acrolein was produced as the WO_x coverage was increased from 0.7 ML to above 1 ML, whereas the increase of propylene concentration was not significant.

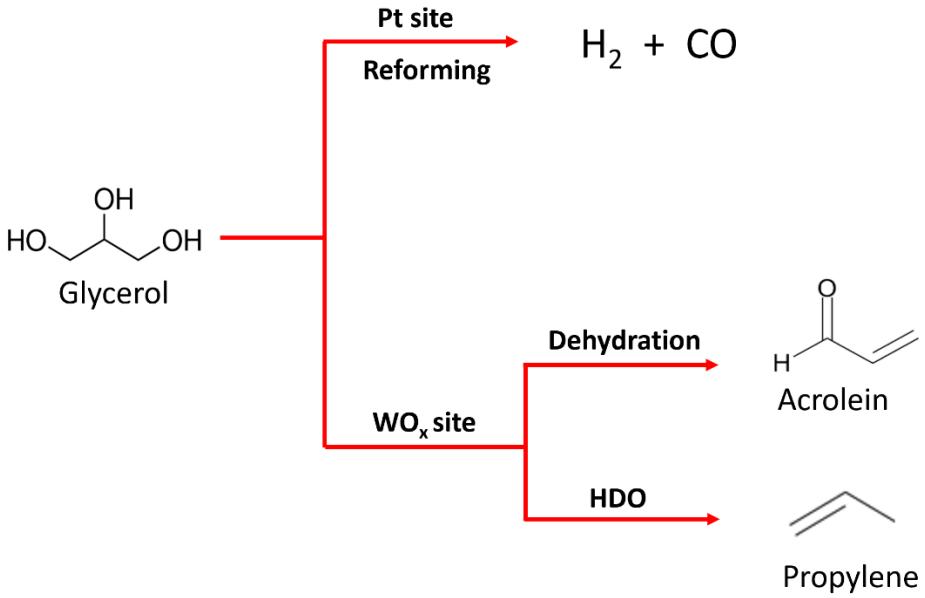

Scheme 5.1 Reaction pathways of glycerol over the Pt and WO_x sites of WO_x/Pt(111).

Table 5.1 Concentration (molecules per metal atom) of products from the reforming, dehydration, and HDO pathways of glycerol on Pt(111) modified by different coverages of WO_x.

WO_x Coverage	CO	Acrolein	Propylene
0 ML	0.173	0.000	0.000
0.5 ML	0.110	0.000	0.000
0.7 ML	0.010	0.008	0.004
Above ML	0.000	0.012	0.005

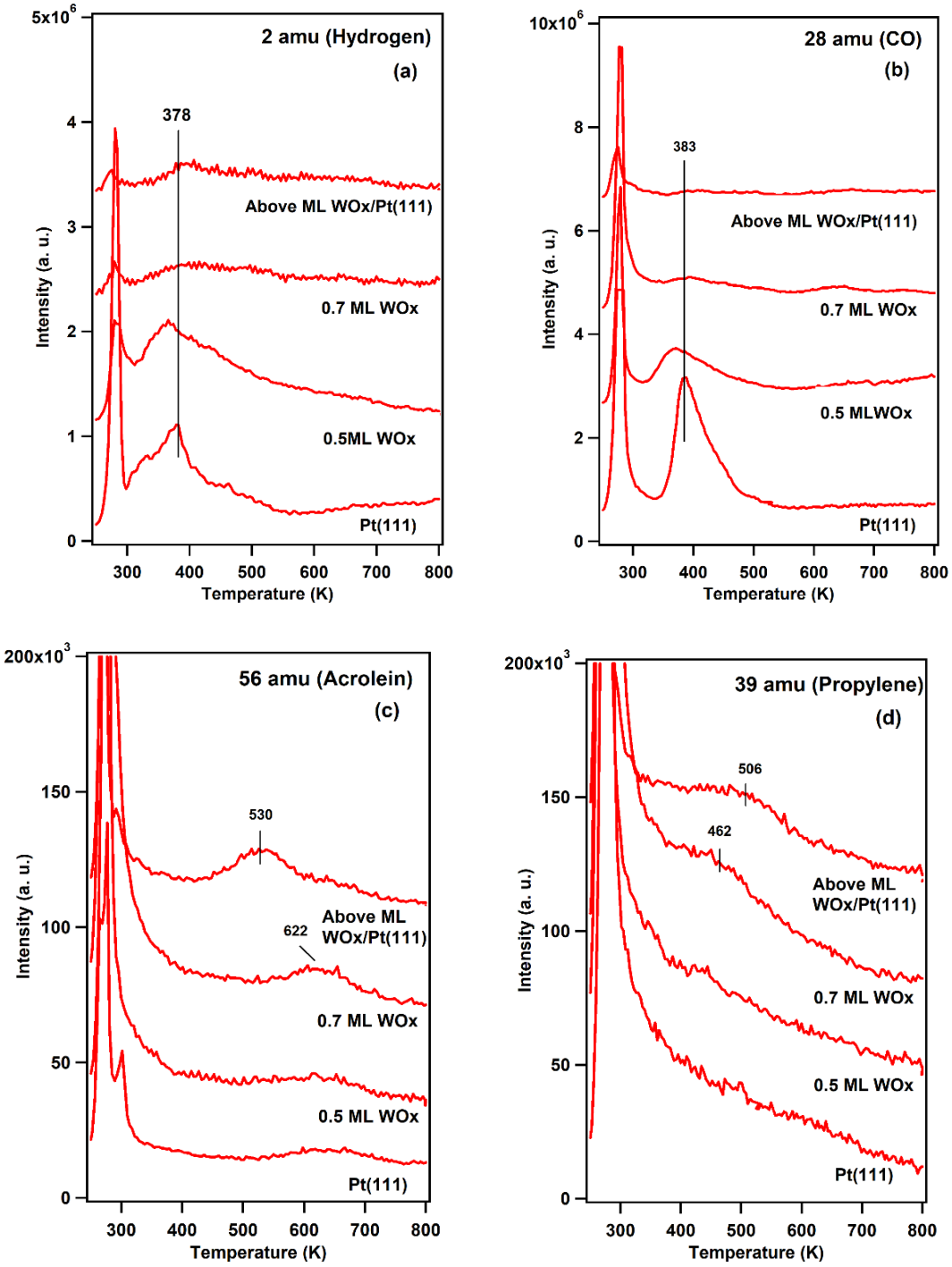

Figure 5.1 Desorption of (a) hydrogen, (b) carbon monoxide, (c) acrolein, and (d) propylene after exposing the corresponding hydrogen pre-dosed surfaces to 4 Langmuir (L, 1 L = $1*10^{-6}$ Torr*s) of glycerol.

5.3.2 HREELS Determination of Surface Intermediates

HREELS experiments were performed to identify the surface intermediates during the adsorption and reaction of glycerol over Pt(111), 0.7 ML WO_x/Pt(111), and above-ML WO_x/Pt(111). The vibrational mode assignments are listed in Table 5.2. The surface was pre-dosed with H_2 followed by exposing to glycerol at 200 K (Figure 5.2(a)). For subsequent spectra, the surface was heated to the indicated temperatures and cooled to below 200 K before the spectra were recorded. As shown in Figure 5.2(a), at 200 K, the adsorption spectra of glycerol were similar on all three surfaces. The similar intensities of the τ(OH) mode at 671 cm^{-1}, ν(CO) mode at 1054 cm^{-1}, δ(CH_2) mode at 1416 cm^{-1}, ν(CH) mode at 2859 cm^{-1}, and ν(OH) mode at 3255 cm^{-1} indicated molecular adsorption of glycerol on all surfaces. Upon heating the surface to 400 K (Figure 5.2(b)), CO was found on Pt(111) at 1980 cm^{-1}. Also observed on the Pt(111) surface was a significant decrease of the τ(OH) and ν(OH) modes, as well as the formation of Pt-C or Pt-O bonds at 497 cm^{-1}. These observations were consistent with the detection of the reforming product CO from TPD experiments. As the surface was modified with 0.7 ML of WO_x, W-O bonds formed with vibrational modes at 564 cm^{-1} and 651 cm^{-1}. On above-ML WO_x/Pt(111), the formation of these W-O bonds was also observed, along with decreased intensities of the ν(CO) mode at 1067 cm^{-1} and the δ(CH_2) mode at 1409 cm^{-1}, indicating that glycerol likely adsorbed through its oxygen atoms with the surface, and had reacted or desorbed to some extent by this temperature. The intensities of the ν(OH) modes at 3255 cm^{-1} on 0.7 ML and above-ML WO_x/Pt(111) also decreased, suggesting that some of the O-H bonds of glycerol had been cleaved. The absence of C=C or C=O modes on the 0.7 ML and above-ML surfaces suggested reaction-limited desorption of acrolein and propylene, in which the products desorbed as soon as they were formed and therefore were not detected by HREELS. In a previous study on

the IPA dehydration reaction on WO_x/Pt(111), only one type of W-O bond was observed at 400 K, either due to the presence of the W-O bond on the as-synthesized WO_x/Pt(111) or the oxygen deposited from the dehydration reaction.[49] In the current study, two types of W-O bonds were observed. This indicated that one type of the W-O bond likely resulted from oxygen deposition from a distinct deoxygenation pathway, in addition to those deposited through the dehydration pathway or the W-O bonds present on the surface before the reaction occurred as shown in the study on IPA over WO_x/Pt(111).[49]

When the surfaces were heated to 500 K (Figure 5.2(c)), a decrease in CO intensity at 1967 cm^{-1} was observed on Pt(111), consistent with the desorption of CO from TPD experiments. The remainder of CO on the surface was likely from re-adsorbed CO from the UHV background. The spectra for both 0.7 ML and above-ML WO_x/Pt(111) were similar to those at 400 K, suggesting that the reaction intermediates were similar at both temperatures. However, after further heating the surfaces to 600 K, the two types of W-O bonds at 537 cm^{-1} and 638 cm^{-1} on 0.7 ML and above-ML WO_x/Pt(111) became more prominent. More importantly, the ν(W-O) mode at 537 cm^{-1} increased significantly on 0.7 ML WO_x/Pt(111). Considering the onset of the dehydration product (acrolein) at around 550 K on 0.7 ML WO_x/Pt(111) as compared to that of the HDO product (propylene) at around 380 K from TPD experiments (Figure 5.1(c) and (d)), the increase of the ν(W-O) mode at 537 cm^{-1} likely indicated the deposition of oxygen from the dehydration pathway, again consistent with the observation of ν(W-O) mode at 537 cm^{-1} for the IPA dehydration reaction over WO_x/Pt(111).[49] In comparison, the intensity ratio of the two ν(W-O) modes at 537 cm^{-1} and 638 cm^{-1} on above-ML WO_x/Pt(111) remained similar between 400 K and 600 K, likely due to the similar onset and peak temperatures of acrolein and propylene desorption (Figures 5.1(c) and 5.1(d)). Combining these

observations of the two ν(W-O) modes on 0.7 ML and above-ML WO_x/Pt(111), it could be inferred that the ν(W-O) mode at 537 cm^{-1} was contributed from the oxygen deposited through the dehydration pathway overlapping with the W-O bond present on the surface before reaction; and the ν(W-O) mode at 638 cm^{-1} originated from the oxygen deposited via the HDO pathway. The ν(CO) and δ(CH_2) modes on 0.7 ML and above-ML WO_x/Pt(111) continued to decrease in intensity, suggesting that further reaction and product desorption had occurred, consistent with the desorption of acrolein and propylene on both surfaces. In contrast, there were still a significant amount of hydrocarbon fragments and adsorbed CO on Pt(111), which likely resulted from the decomposition of glycerol and re-adsorption of CO from the UHV background. This indicated that Pt likely interacted with glycerol more strongly than WO_x, which led to undesired decomposition of glycerol. Similar results were reported in another study (Chapter 6) on the ring-opening reaction of tetrahydrofurfuryl alcohol (THFA) over WO_x/Pt(111), where WO_x effectively weakened the interaction between THFA and Pt to facilitate the desorption of desired ring-opened product and avoid further decomposition that happened on Pt.

Overall, in agreement with TPD experiments, the HREELS results reflected the distinct pathways on Pt(111), 0.7 ML WO_x/Pt(111), and above-ML WO_x/Pt(111). Pt(111) interacted strongly with glycerol, resulting in the reforming of glycerol as well as further decomposition. In contrast, WO_x-modified Pt(111) surfaces interacted less strongly with glycerol and selectively dissociated the C-O bonds of glycerol via the hydration and HDO pathways. The different ratios of the two types of W-O bonds observed on the 0.7 ML and above-ML WO_x/Pt(111) surfaces at different temperatures were consistent with the coverage-dependent reaction pathways from TPD experiments. Dehydration was favored on above-ML WO_x/Pt(111) with hydroxyl groups being the active sites, similar to that reported in the literature;[49] whereas HDO was preferred on an

interfacial (0.7 ML) WO_x/Pt(111) site where the interaction between Pt and WO_x helped to stabilize the active sites, also consistent with previous studies. [161,169]

Table 5.2 Vibrational mode assignments of glycerol

	Frequency (cm^{-1})		
Mode	**Pt(111)**	**WO_x/Pt(111)**	**Mo_2C/Mo(110)[a]**
ν(Pt-O), ν(Pt-C)	497		
ν(Mo-O)			570
ν(W-O)		537, 638	
τ(OH)	671	671	671
ν(CO)	1054	1054	1060
δ(CH_2)	1416	1416	1430
ν(CH)	2859	2859	2873
ν(OH)	3255	3255	3248

ν – stretching, τ – torsion, δ – deformation.

a. Reference[44]

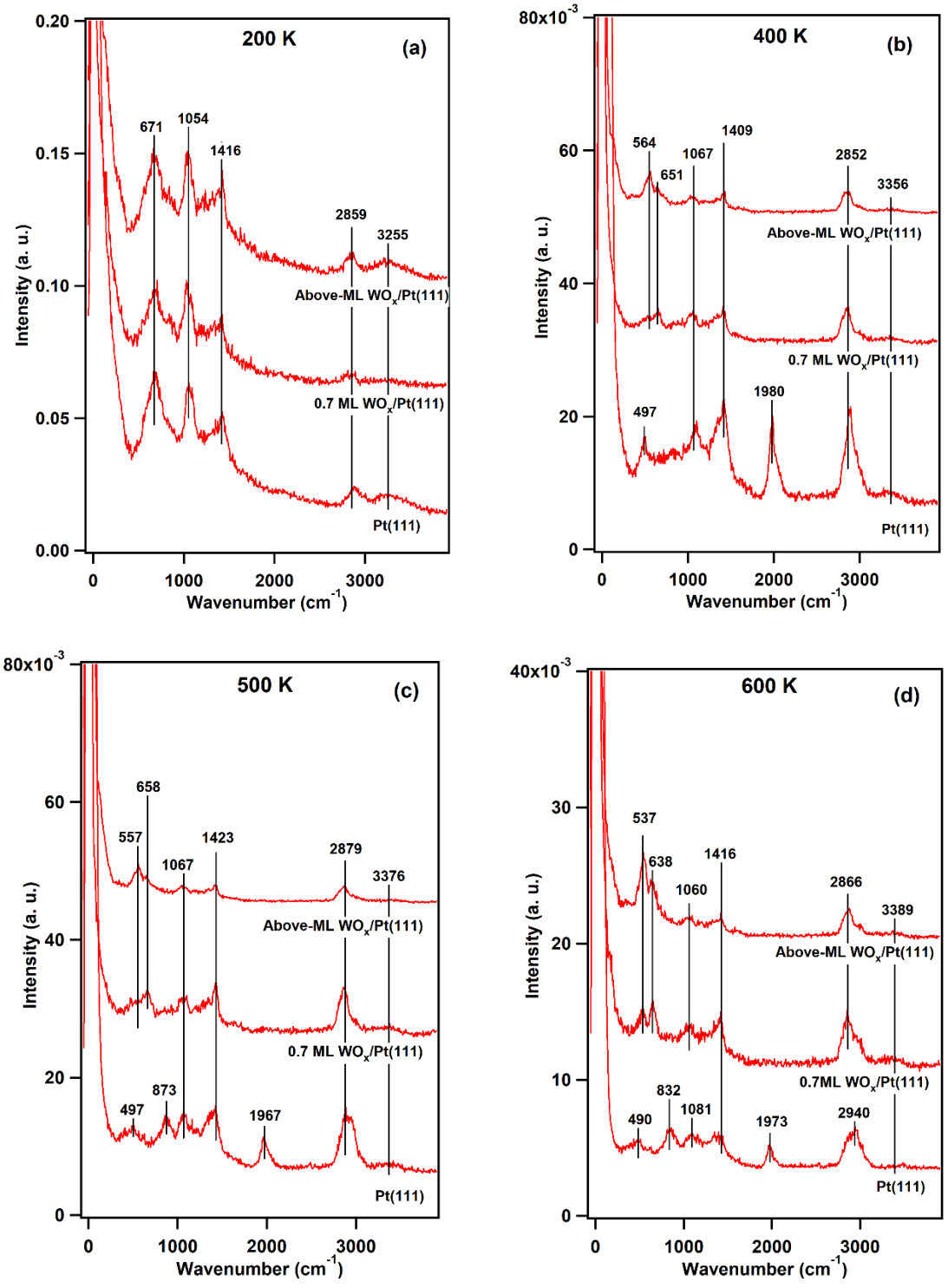

Figure 5.2 HREEL spectra after exposing the corresponding hydrogen pre-dosed surfaces to 4 L of glycerol at (a) 200 K and heated to (b) 400 K, (c) 500 K, and (d) 600 K.

5.4 Conclusions

This work presents the first surface science study of glycerol over WO_x/Pt(111) model surfaces to unravel the nature of the multiple active sites on the surface. TPD experiments identified three types of active sites. Pt sites were responsible for reforming, and there were two types of deoxygenation WO_x sites. One type of site was active for the glycerol dehydration reaction to produce acrolein. This type of sites possibly originated from the hydroxyl groups present on WO_x and the activity was highest on a surface fully covered with WO_x. The other type of deoxygenation sites catalyzed the HDO reaction to form propylene, and likely originated from the oxygen vacancies stabilized at the WO_x/Pt(111) interface. HREELS revealed that glycerol interacted strongly with Pt(111), leading to reforming reaction and undesired decomposition. On WO_x-modified Pt(111) surfaces, glycerol bonded to the surface via its oxygen atoms and that there were two types of W-O bonds observed, resulting from oxygen deposition via two different deoxygenation pathways. Consistent with TPD experiments, HREELS observations showed that dehydration was more favorable on the WO_x sites, while the HDO reaction was more facile on the WO_x/Pt(111) interface sites, likely due to the interaction between WO_x and Pt that stabilized the active sites. The understanding gained in this study on the various deoxygenation active sites should provide important information for guiding rational catalyst design for the upgrading of biomass-derived oxygenates

5.5 Acknowledgements

This article was sponsored by the Catalysis Center for Energy Innovation (CCEI), an Energy Frontier Research Center (EFRC) funded by the U.S. Department of Energy, Office of Basic Energy Sciences under Award Number DE-SC0001004. I acknowledge Dr. Zhexi Lin and William Porter for their contribution to the surface science results.

Chapter 6: Ring-Opening of Tetrahydrofurfuryl Alcohol over WO_x-Modified Pt(111) Surfaces

6.1 Introduction

The substantial environmental challenges associated with fossil fuels and petroleum-derived chemicals have led to an intense interest in biomass-derived alternatives for the mitigation of CO_2 emissions and as a source of renewable platform chemicals.[170–174] Biomass-derived oxygenates (BDOs), particularly heterocycle-containing molecules such as tetrahydrofurfuryl alcohol (THFA) and furfural, can be generated from lignocellulosic biomass by established industrial techniques to serve as renewable platform oxygenates. [51,52,175] While many strategies have been investigated to better utilize these oxygen-rich biomass molecules, catalyst selection remains critically important for the tunable and selective conversion to value-added products over byproducts.[43,176]

BDOs can be catalytically upgraded by the selective hydrodeoxygenation[44] or dehydration[49] of C-O bonds. The hydrogenolysis of heterocyclic BDOs, via the selective ring-opening of the C-O bond within the ring, represents a unique opportunity for the production of diol molecules, which are important monomers for the manufacturing of polyester and polyurethane resins.[55,56,177–179] Several types of catalysts have been reported in the literature for the ring-opening of these BDOs, including transition metal oxides[57,58,180–184] and bimetallic catalysts[185]. Among the transition metal oxides studied, Pt/WO_x and the inverse oxide WO_x/Pt have demonstrated interesting catalytic properties for the selective C-O bond scission. For example, silica-supported Pt/WO_x was used to convert 1,4-anhydroerythritol into 1,3-butanediol.[182] A volcano-type dependence on the W:Pt ratio was observed, as it was postulated that WO_x clusters were anchors for 1,4-anhtoerthritol and Pt sites activated co-fed H_2. This

bifunctionality was also observed for the ring-opening of THFA to 1,5-pentanediol (1,5-PeD).[57,58] On carbon-supported Pt/WO_x, a direct metal-to-oxide contact was necessary for active hydrogenolysis, however a simple physical mixture of Pt/C and WO_x/C also resulted in comparable selectivity.[57] In a separate study, the 1,5-PeD yield was closely correlated to the loading of WO_3, however, it was also postulated that the zirconia support was mechanistically important for THFA hydrogenolysis.[58] While these studies indicate Pt/WO_x catalysts are active for the selective hydrogenolysis of heterocyclic BDOs, a fundamental understanding of the active sites and reaction intermediates is important for guiding the design of catalysts.

In order to better understand the hydrogenolysis reaction of heterocyclic BDOs, this work utilized surface science techniques for the study of the decomposition and ring-opening reactions of THFA on Pt(111) and WO_x/Pt(111) inverse oxide surfaces. The WO_x/Pt(111) surface was prepared by chemical vapor deposition of $W(CO)_6$ on a clean Pt(111) surface cooled to liquid nitrogen temperature, followed by electron-induced decomposition of $W(CO)_6$ and the oxidation and reduction of the precursor-exposed surface. The as-synthesized surface was then pre-dosed with hydrogen and exposed to the reactant of interest, either THFA or 1,5-PeD. Temperature programmed desorption (TPD) experiments were used to detect gas-phase products. High resolution electron energy loss spectroscopy (HREELS) was used to identify reaction intermediates on the surface, which informed the mechanism that led to the desorption of different gas-phase products from the Pt and WO_x active sites. 1,5-PeD was used as a probe molecule for both TPD and HREELS experiments to better understand the decomposition or desorption of the ring-opened THFA product. By utilizing surface science techniques, this study provides fundamental insight into the Pt and WO_x active sites for the reaction of THFA on

WO_x/Pt(111) surfaces, and should inform catalyst design for the selective ring-opening of other heterocyclic BDOs.

6.2 Methods

The TPD and HREELS experiments were conducted in separate ultrahigh vacuum (UHV) chambers, which have been described previously.[44,157,160,185,186] The WO_x-modified Pt(111) surfaces were prepared by the chemical vapor deposition (CVD) of $W(CO)_6$ (99%, Strem Chemicals).[49] In brief, $W(CO)_6$ aliquoted into a glass sample cylinder was decomposed upon heating to 403 K and dosed at a pressure of 5 x 10^{-8} torr onto a Pt(111) surface at 130 K. The purity of gas-phase $W(CO)_6$ was monitored by mass spectrometry (MS) and the presence of W on the dosed surface was confirmed by Auger electron spectrometry (AES). The adsorbed $W(CO)_6$ then underwent electron-induced decomposition by placing the surface in front of an ion gun, which had a beam voltage of 3 kV and an emission current of 2 mA. The surface was then oxidized by heating from 130 K to 573 K at a rate of 0.5 K/s with a background pressure of 5 x 10^{-7} torr O_2, and then held at 573 K in the same gas environment for 30 minutes. After oxidation, the surface was flashed to 950 K in 5 x 10^{-7} torr O_2 and then reduced at 473 K for 10 minutes in 5 x 10^{-8} torr H_2. The WO_x surface coverage was determined by CO TPD,[49] and confirmed by AES calculations of the W(38 eV)/Pt(168 eV) ratio.

The TPD experiments were conducted in a 2-level UHV chamber with a base pressure of 8 x 10^{-10} Torr. The chamber was fitted with a UTI-100C quadrupole MS, AES, Ne^+ sputter gun, and several gas lines for dosing and CVD. In a typical TPD experiment, the as-synthesized surface was cooled to 150 K and pre-dosed with 5 Langmuir (1 L = 10^{-6} torr*s) of H_2, followed by dosing 4 L of either THFA or 1,5-PeD.[185] After dosing, the surface was oriented in front of the MS for the detection of gas-phase products, and the temperature was ramped at 3 K/s to 850

K. For reactant preparation, THFA (99%, Sigma Aldrich) and 1,5-PeD (99.1%, Sigma Aldrich) were aliquoted into glass sample cylinders that had been baked out overnight. Prior to dosing, the reactants underwent a series of freeze-pump-thaw cycles and purity was confirmed by MS. The quantification of the TPD results was based on a previously described procedure.[124]

The HREELS experiments were conducted in a 3-level UHV chamber equipped with the same instrumentation as the TPD chamber, with the addition of HREELS. For each HREELS experiment, the as-synthesized surface was dosed using the same procedure that was used for TPD. After dosing, the surface was placed into the HREELS focal plane where the angles of incidence and reflection were 60° with respect to the surface normal. The beam was optimized to a rate of 1-2 x 10^4 counts/s and a peak resolution with a full width half maximum (FWHM) between 50 and 70 cm^{-1} prior to each scan. Between scans, the surface was flashed to the desired temperature and cooled to temperatures below 200 K prior to HREELS measurements.

6.3 Results and Discussion

6.3.1 Identification and Quantification of Gas-Phase Products using TPD

TPD experiments were performed to identify gas-phase products, and to quantify the activity for the decomposition and ring-opening reactions of THFA on Pt(111) and WO_x-modified Pt(111) surfaces. Figures 6.1(a) and 6.1(b) show that THFA decomposed on the Pt(111) surface, as H_2 (*m/e* = 2) and CO (*m/e* = 28) were the only gas-phase products to desorb. Several distinct H_2 desorption peaks are observed on the Pt(111) surface, and can be associated with both the decomposition of THFA and the recombinative desorption of pre-dosed hydrogen (Figure 6.2). The decomposition of THFA on Pt(111) was not surprising because THFA reportedly decomposed on a similarly prepared Ir(111) surface.[185] The prior study indicated that while THFA ring-opened to the desired dioxy intermediate on Ir(111) pre-dosed with H_2, the

species was unable to undergo hydrogenation under UHV reaction conditions, leading to subsequent thermal decomposition to H_2 and CO.[185] Similarly in the current work gas-phase 1,5-PeD did not desorb from Pt(111) (Figures 6.1(c) and 6.1(d)), although TPD results alone could not rule out the possibility of the formation and decomposition of the desired ring-opened intermediate, as discussed later in the HREELS results.

Figure 6.2 shows the 2 amu and 28 amu spectra from the TPD of 5 L H_2 on Pt(111) and WO_x-modified surfaces. Several desorption peaks were observed on the 2 amu spectrum of the Pt(111) surface, and were attributed to the recombinative desorption of H_2. In Figure 6.2, The CO desorption peak at 510 K on the Pt(111) surface was attributed to the desorption of CO from the UHV background. On WO_x-modified surfaces, the desorption peak attributed to background CO was not observed.

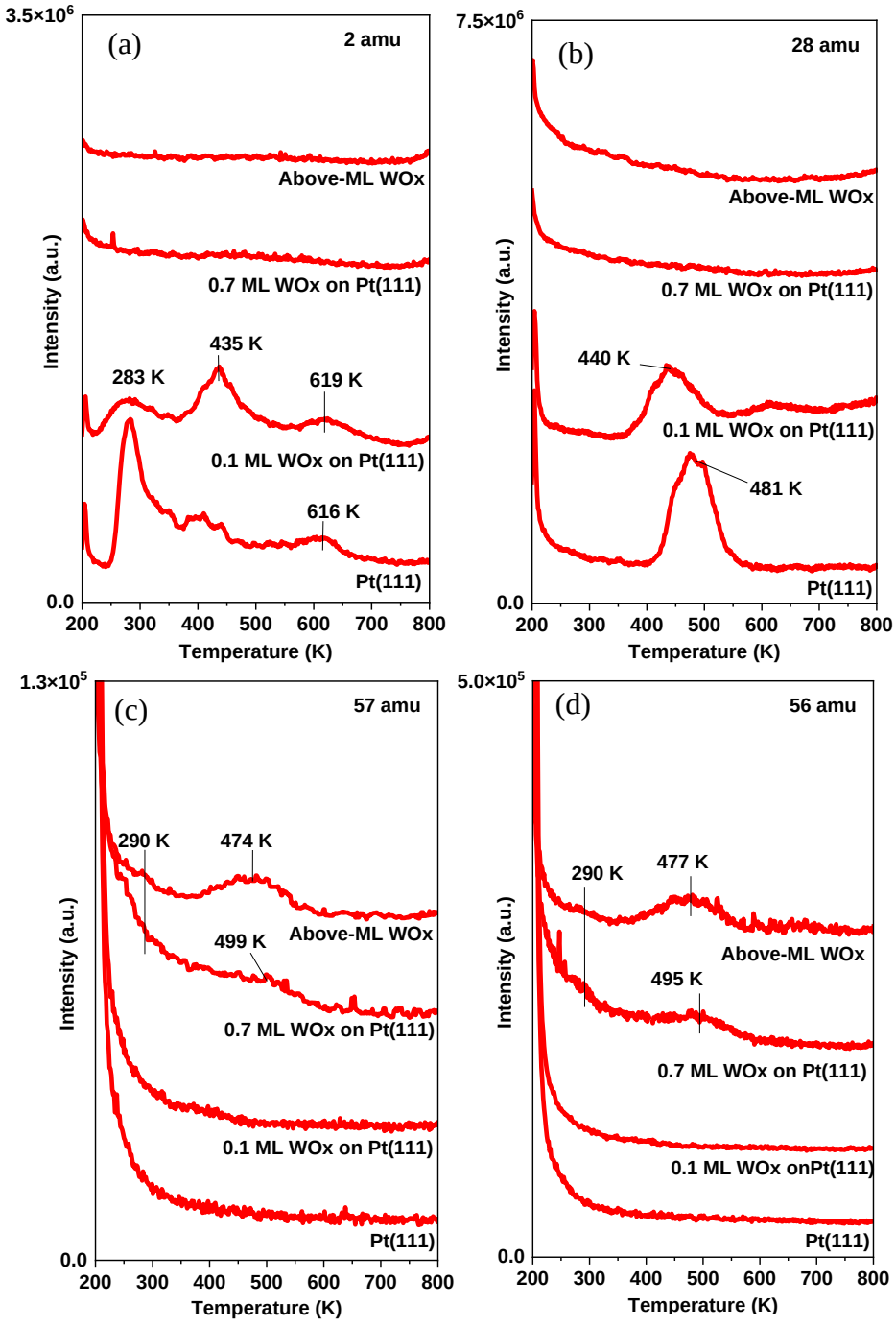

Figure 6.1 TPD spectra of 4 L THFA on Pt(111) and WO_x-modified Pt(111) surfaces pre-dosed with 5 L H_2.

The product distribution on surfaces with low-coverages of WO_x depended significantly on the thickness of the deposited metal oxide. On 0.1 ML WO_x/Pt(111), THFA decomposed into

CO and H_2, similar to the pathway observed on the clean Pt(111) surface. Notably, the addition of 0.1 ML WO_x to the Pt(111) surface lowered the desorption temperature of CO by 40 K, which was in agreement with past literature[49] and indicated that the addition of WO_x decreased the binding energy of CO with the surface.

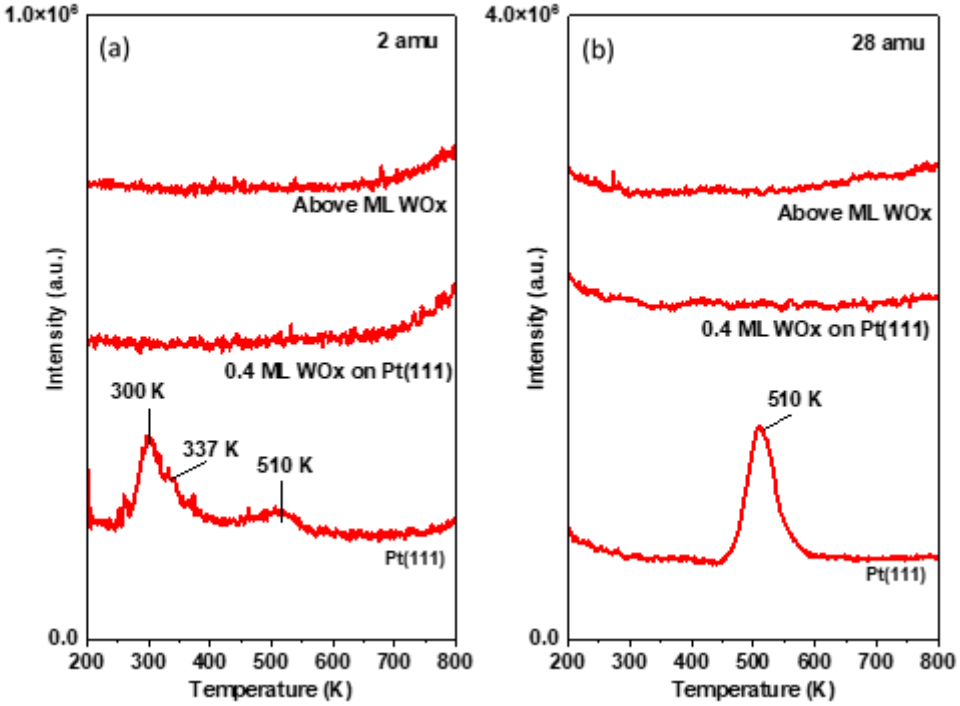

Figure 6.2 TPD spectra of 5 L H_2 on Pt(111) and WO_x-modified Pt(111) surfaces.

At 0.7 ML and above-ML WO_x-modification resulted in both the ring-opening of THFA, and the hydrogenation/desorption of the dioxy (likely 1,5-pentanedioxy) intermediate as gas-phase 1,5-PeD. On these surfaces, the desorption peaks attributed to 1,5-PeD (*m/e* = 56 and *m/e* = 57) were observed (Figures 6.1(c) and 6.1(d)). As WO_x coverage increased from 0.7 ML to above 1 ML WO_x, the desorption peak area increased, coinciding with an increase in activity for the ring-opening reaction (Table 6.1). The 1,5-PeD desorption onset and peak temperatures also decreased as a function of WO_x coverage, indicating that the addition of WO_x likely weakened

the binding energy of the ring-opened intermediate with the surface and that the desorption of the ring-opened product from WO_x/Pt(111) was likely desorption-limited.

Table 6.1 Activity (molecules per metal atom) of decomposition and ring-opening products from THFA TPD experiments on WO_x-modified Pt(111) surfaces.

WO_x coverage	decomposition	ring-opening
0 ML	0.126	0.000
0.1 ML	0.025	0.000
0.7 ML	0.000	0.008
above 1 ML	0.000	0.021

TPD experiments following the adsorption and reaction of 1,5-PeD on Pt(111) and WO_x-modified Pt(111) surfaces were also performed to provide further insight on the desorption of ring-opened THFA reaction products. Consistent with the partial decomposition of THFA on Pt(111) and 0.1 ML WO_x/Pt(111), Figures 6.3(a) and 6.3(b) show that 1,5-PeD decomposed on Pt(111) and Pt(111) modified by relatively low coverages of WO_x. Figures 6.3(c) and 6.3(d) present the same mass spectra representative of 1,5-PeD in Figures 6.1(c) and 6.1(d), *m/e* = 56 and *m/e* = 57, respectively. In agreement with the TPD results of THFA on these prepared surfaces, 1,5-PeD only desorbed from the Pt(111) surface modified by a relatively thick, above-ML coverage of WO_x. While the peak shape differed between the desorption of dosed 1,5-PeD (Figure 6.3) and 1,5-PeD ring-opened product (Figure 6.1), the desorption onset and peak temperature were similar.

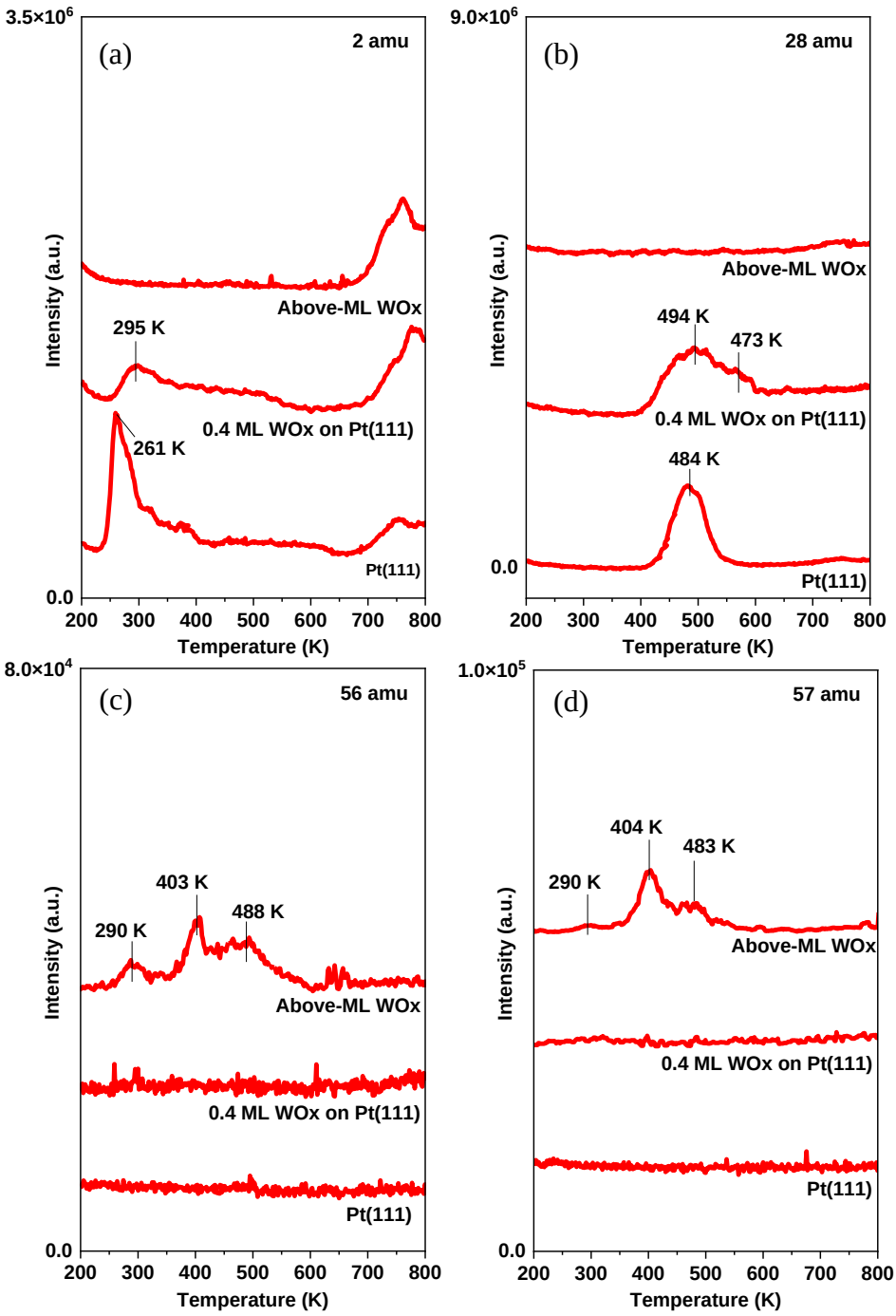

Figure 6.3 TPD spectra of 4 L 1,5-PeD on Pt(111) and WO_x-modified Pt(111) surfaces pre-dosed with 5 L H_2.

Overall, the TPD experiments demonstrated that near-ML and above-ML WO_x-modified Pt(111) surfaces were active and selective for the ring-opening of THFA to 1,5-PeD. The results

also suggested that the clean Pt(111) surface bonded too strongly with reaction intermediates, which resulted in undesired decomposition.

6.3.2 Identification of Surface Reaction Intermediates using HREELS

HREELS was used to identify the adsorbed species and surface intermediates that led to the desorption of different gas-phase products on Pt(111) and WO_x-modified Pt(111) surfaces. Figure 6.4 shows the HREEL spectra of adsorbed and reacted THFA on Pt(111), 0.4 ML WO_x/Pt(111), and above-ML WO_x/Pt(111) surfaces. Similar to the TPD experiments of 1,5-PeD, the ring-opened product was also used as a reference molecule for the HREELS identification of possible 1,5-PeD-type intermediates (Figure 6.5). The vibrational mode assignments for adsorbed THFA and 1,5-PeD on the Pt(111) and WO_x/Pt(111) surfaces are summarized in Table 6.2.

On each surface studied, the characteristic vibrational modes of THFA were present after adsorption at 150 K. Consistent with a previous HREELS study of THFA on Ir(111),[185] these vibrational modes included the ν(CC) stretching of the C-C bond at 860 cm^{-1}, the ν(CO) stretching of C-O in the saturated furan ring and the methoxy group at 979 cm^{-1} and 1115 cm^{-1}, respectively, the δ(CH) deformation and ν(CH) stretching of the of the sp^3 C-H bond at 1190 cm^{-1} and 2949 cm^{-1}, respectively, and the $\rho_w(CH_2)$ wagging and $\delta(CH_2)$ deformation of the of CH_2 group at 1379 cm^{-1} and 1479 cm^{-1}, respectively. It should also be noted that stretching modes related to Pt-C/O and W-O bonds were observed at 200 K and above, corresponding to peaks at 554 cm^{-1} and 620 cm^{-1}, respectively, in agreement with prior reports in the literature.[49,185,186] Furthermore, the reference vibrational modes for 1,5-PeD on Ir(111) (Table 6.2, [c]Ref[186]) were based on the reported vibrational modes listed for 1,3-propanediol on Mo_2C,[186] and were used as

approximate vibrational frequencies of the corresponding modes of 1,5-PeD on Ir(111), because they were not previously reported.[185]

The observation of the τ(OH) mode at 748 cm^{-1} and ν(OH) at 3319 cm^{-1} on both clean Pt(111) and WO_x-modified Pt(111) surfaces revealed molecular adsorption of THFA at 150 K. These vibrational modes disappeared upon heating the surface to 200 K, indicating the scission of the O-H bond. While the 200 K spectra of Pt(111) and WO_x-modified Pt(111) surfaces were qualitatively similar, subsequent heating to higher temperatures led to different reaction intermediates.

On Pt(111), when the temperature was increased from 200 K to 300 K, the δ(CH) peak at 1190 cm^{-1} was still present, indicating that the saturated furan ring remained intact. The relative peak intensity of the methoxy ν(CO) mode at 1118 cm^{-1} decreased, and possibly redshifted to overlap with the ν(CO) mode of the C-O bond in the saturated furan ring. Upon further heating to 400 K, the relative intensity of the ν(CO) mode (992 cm^{-1}) of the C-O bond in the heterocycle decreased, which suggested the selective scission of the C-O bond for ring-opening. The observed ν(CO) vibrational mode at 2036 cm^{-1} was associated with the adsorbed CO species, and reached a maximum intensity at 400 K. The intensity of this peak decreased after further heating the surface to 500 K, corresponding to the TPD results that CO desorbed from the Pt(111) surface at a peak temperature of 481 K. It should be noted that this vibrational mode should be associated with adsorbed CO from both the background UHV environment and the

decomposition of the reaction intermediates.

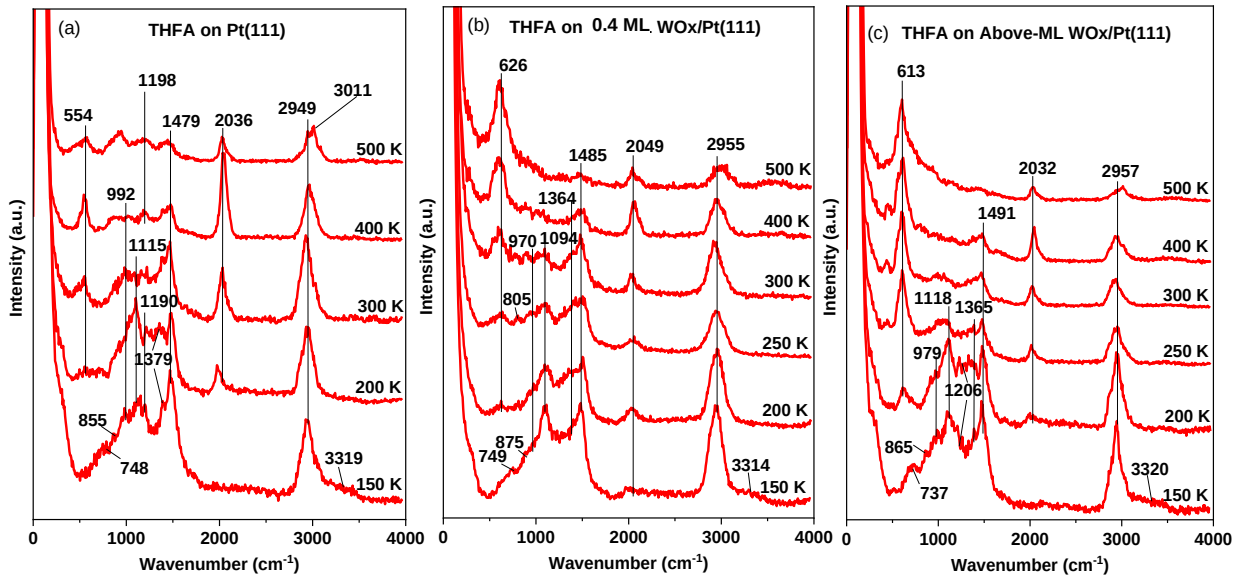

Figure 6.4 HREEL spectra of 4 L THFA on Pt(111) and WO_x-modified Pt(111) surfaces pre-dosed with 5 L H_2.

Figure 6.5(a) shows the comparison of 300 K, 400 K, and 500 K HREEL spectra of THFA and 1,5-PeD on H_2-pre-dosed Pt(111). The qualitative similarity of the HREEL spectra from these two molecules on Pt(111) suggested that the intermediate species was likely 1,5-pentanedioxy, which underwent further decomposition to produce CO and H_2 as detected in the TPD results rather than hydrogenation and desorption of the ring-opened product upon further heating of the surface. These results are consistent with those reported for the reaction of THFA and 1,5-PeD on H_2-pre-dosed Ir(111) surfaces.[185]

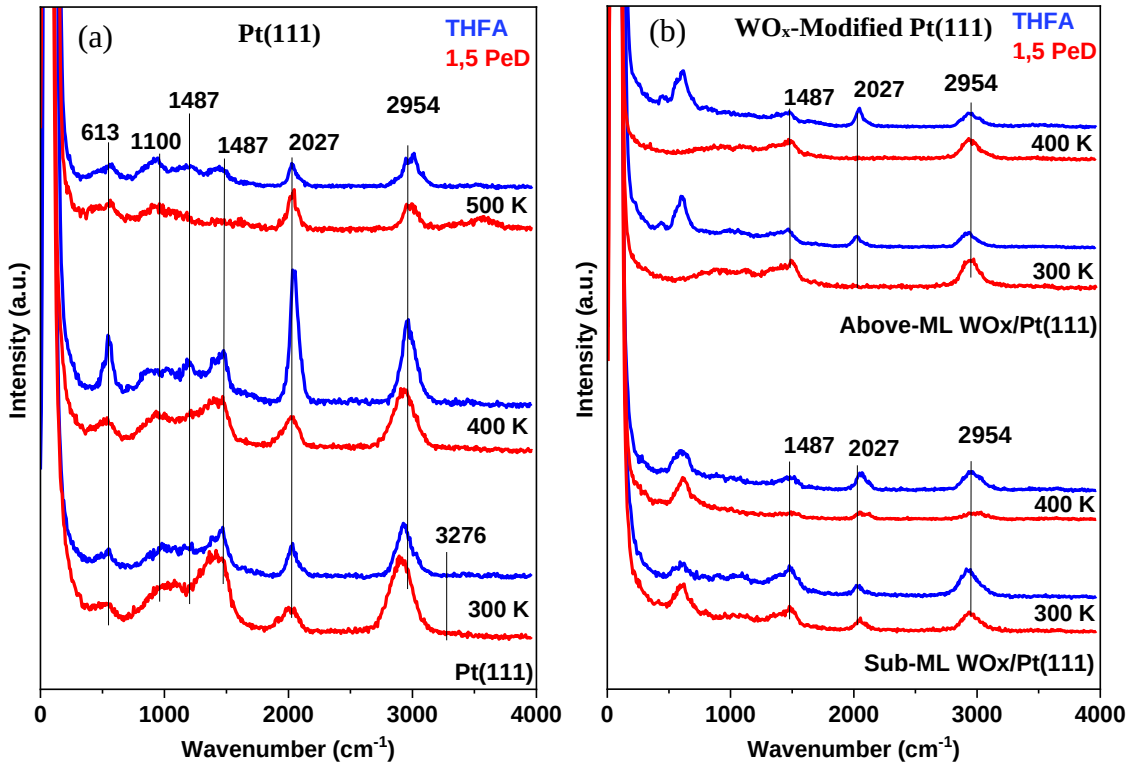

Figure 6.5 Comparison of the HREEL spectra of 4 L THFA or 4 L 1,5-PeD on WO_x-modified Pt(111) surfaces pre-dosed with 5 L H_2.

Table 6.2 Vibrational assignment of THFA and 1,5-PeD [cm^{-1}].

Tetrahydrofurfuryl Alcohol				1,5 Pentanediol			
Mode	WOx/Pt(111)[a]	Pt(111)[a]	Ir(111)[b]	Mode	WOx/Pt(111)[a]	Pt(111)[a]	Ir(111)[c]
τ(OH)	737	748	--	ρ_r(CH$_2$)	905	890	850
ν(CC)	865	855	899	ν(CO)	1047	1077	1020
ν(CO)	979	992	993	ρ_w(CH$_2$)	1331	--	1350
	1118	1115	1047	δ(CH$_2$)	1485	1504	1450
δ(CH)	1206	1190	1161	ν(CH)	2943	2918	2850
ρ(CH$_2$)	1365	1379	1295				
δ(CH$_2$)	1491	1479	1429				
ν(CH)	2955	2949	2906				
ν(OH)	3320	3319	--				

δ, deformation; ν, stretching; ρ_r, rocking; ρ_t, torsion; ρ_w, wagging.

[a]This work. [b]Ref[37]. [c]Ref[125].

In comparison to the intermediates observed on Pt(111), differences arise in the HREEL spectra for WO_x-modified Pt(111) at temperatures higher than 200 K (Figures 6.4(a) and 6.4(b)). After heating the above-ML WO_x surface to 250 K, the δ(CH) peak at 1206 cm^{-1} was no longer visible. Furthermore, at this temperature the ν(CO) mode at 979 cm^{-1} associated with the C-O bond of C_2 (Scheme 6.1) in the heterocycle was no longer present. These spectroscopic changes suggested that the tetrahydrofuran ring opened on WO_x-modified surfaces at lower temperatures than on Pt(111), which occurred between 300 K and 400 K. Upon further heating of the surface from 400 K to 500 K, the ring-opened intermediate desorbed from the above-ML WO_x/Pt(111) surface, as indicated by the disappearance of the ρ(CH_2) and δ(CH_2) modes. This finding was consistent with the TPD results, which showed the desorption of 1,5-PeD from the above-ML WO_x/Pt(111) at 474 K.

Figure 6.5(b) compares the HREEL spectra of 1,5-PeD and THFA on WO_x-modified Pt(111) surfaces at 300 K and 400 K. The sub-ML WO_x coverage was 0.5 ML WO_x/Pt(111) for the 1,5-PeD experiments, and 0.4 ML WO_x/Pt(111) for the THFA experiments. The HREEL spectra of these two molecules on WO_x-modified surfaces were qualitatively similar, which suggested that the ring-opened intermediate of THFA was likely 1,5-pentanedioxy. Based on the HREELS and TPD results, the active site-dependent THFA reaction mechanisms on Pt and WO_x are presented in Scheme 6.1. Because the HREELS results suggested that THFA molecularly adsorbed to both WO_x-modified and clean Pt(111) surfaces, and that the ring-opened dioxy intermediate also formed on these surfaces, the difference between the desorption of the gas-phase ring-opened product and further decomposition is closely related to the final step of Scheme 6.1. The combined results indicate that the addition of near-ML and above-ML coverages of WO_x to Pt(111) weakens the binding of the ring-opened intermediate to an extent

that enables hydrogenation and 1,5-PeD desorption from the WO_x site. This is contrasted by the decomposition of the ring-opened intermediate on Pt(111) and Pt(111) surfaces modified by low coverages of WO_x, where Pt is the dominant surface site.

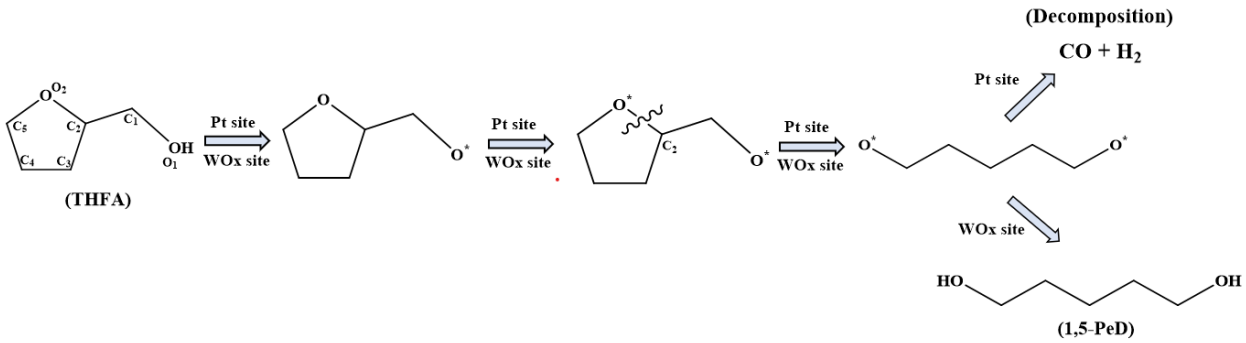

Scheme 6.1 Proposed reaction mechanism of THFA ring-opening on Pt and WO_x sites, followed by either the desorption of decomposition products (Pt site) or gas-phase 1,5-PeD (WO_x site).

6.4 Conclusions

In this work, surface science techniques were used to study the decomposition and ring-opening reactions of THFA on Pt(111) and WO_x-modified Pt(111) surfaces. The reaction that occurred at the surface was active site dependent. HREELS experiments revealed that while THFA ring-opened on Pt sites, the 1,5-pentanedioxy-like intermediate bonded strongly to the surface and characteristic vibrational modes were observed at temperatures as high as 400 K. The further decomposition of this intermediate on Pt sites was confirmed by TPD experiments, as CO and H_2 were the only products to desorb from the Pt(111) surface. In contrast, on WO_x sites THFA underwent selective hydrogenolysis, and the ring-opened 1,5-pentanedioxy-like intermediate hydrogenated and desorbed as the desired 1,5-PeD reaction product. TPD experiments of THFA on near-ML and above-ML WO_x/Pt(111) surfaces pre-dosed with hydrogen resulted in the desorption of gas-phase 1,5-PeD. Parallel TPD experiments of 1,5-PeD

were also conducted on Pt(111) and WO_x-modified Pt(111) surfaces to understand the desorption of the ring-opened product. In agreement with the THFA TPD results, 1,5-PeD only desorbed from surfaces with relatively thick coverages of WO_x. HREELS results also indicated that the ring-opening of THFA occurred at lower temperatures on WO_x sites than on Pt sites, and that the desorption temperature of the 1,5-pentandioxy-like intermediate agreed with the THFA and 1,5-PeD TPD experiments. While selective scission of the C-O bond in the saturated furan ring occurred on both Pt and WO_x sites, the combined TPD and HREELS results suggest that WO_x modification weakened the interaction between the 1,5-pentandioxy-like intermediate and the surface, which allowed for the desorption of the desired ring-opened product. This work provides an understanding of two distinct active sites on the WO_x/Pt(111) inverse oxide surface, and should offer a strategy for catalyst design for the ring-opening of other relevant heterocyclic biomass-derived oxygenates.

6.5 Acknowledgements

This research was sponsored by the Catalysis Center for Energy Innovation (CCEI), an Energy Frontier Research Center (EFRC) that is funded by the Office of Basic Energy Sciences at the U.S. Department of Energy under Award Number DE-SC0001004. I acknowledge Prof. Sergey Rykov, Dr. Zhexi Lin, and William Porter for their contribution to the surface science results.

Chapter 7: Conclusion and Future Directions

7.1 Conclusions

The discovery of catalytically active, stable, and tunable earth-abundant catalysts is central to the development of electrochemical devices that convert electrical power into chemical energy, and the replacement of conventional petrochemical feedstocks with biomass-derived platform oxygenates. This work characterizes several earth-abundant and low-cost nitrogen- and oxygen-modified materials as electrocatalysts, and as catalysts for upgrading several important BDOs. TMNs as admetal-supports were shown to strategically reduce platinum group metal loading for both electrochemical and thermochemical reactions, and enable reaction pathway tunability. Fundamental studies of inverse oxides on well-defined surfaces characterized several unique active sites responsible for the selective deoxygenation and ring-opening of functionally complex, oxygen-rich BDOs. Where applicable, DFT-calculations were used to develop trends in activity by comparing experimental results with 1st principles calculations such as the binding energy of adsorbed reaction intermediates. In sum, this work provides a basis upon which future researchers may utilize nitrogen- and oxygen-modified earth-abundant materials as inexpensive catalysts for next-generation industrial chemical reactions

Chapter 3 focuses on the electrochemical characterization of two TMN materials, WN and NbN. Thin films were synthesized at the surface of parent metal foils, and characterized using XRD, GI-XRD, and XPS. The stability of WN and NbN was assessed over wide pH-potential regimes, and pseudo-Pourbaix diagrams were generated from cyclic voltammetry data of reversible and irreversible oxidation profiles. The hydrogen evolution reaction (HER) was selected as a probe reaction, where the activities of unmodified and Pt-modified WN and NbN were quantified and correlated to the DFT-calculated hydrogen binding energies and Gibbs free

energies for hydrogen adsorption. Both Pt-modified WN and NbN demonstrated Pt-like HER activity with near-monolayer (ML) Pt coverage in acid electrolyte. While this work highlights the HER activity and regimes of electrochemical stability of WN and NbN, pseudo-Pourbaix diagrams have been previously useful in selecting TMCs for specific reactions, and can be extended here to inform other electrochemical reactions where the TMN of interest should be stable.[22–24]

Chapters 4, 5, and 6 utilize surface science techniques, including temperature programmed desorption (TPD) and high resolution electron energy loss spectroscopy (HREELS), to probe nitrogen- and oxygen-modified transition metals for the reaction of several BDOs. Chapter 4 presents a study of ethanol decomposition and reforming on unmodified and Pt-modified Mo_2N, respectively. TPD experiments revealed that on Mo_2N, ethanol primarily underwent decomposition to H_2, C_{ads}, and O_{ads}. The ethanol reaction pathway shifted from decomposition to reforming on Pt-modified Mo_2N surfaces. HREELS was used to further investigate the reaction intermediates on four surfaces: Mo_2N, sub-ML Pt/Mo_2N, ML Pt/Mo_2N, and Pt(111). The HREELS results indicated that while Mo_2N decomposed the ethoxy intermediate by the scission of C-C, C-O, and C-H bonds, Pt-modification enabled the preservation of the C-O bond that resulted in ethanol reforming.

Chapters 5 and 6 study a WO_x-modified Pt(111) surface for the selective deoxygenation and ring-opening of glycerol and THFA, respectively. By studying the reaction of glycerol on WO_x/Pt(111) surfaces, Chapter 5 builds on a colleagues work that used CO and isopropanol (IPA) as probe molecules to characterize distinct Pt and WO_x active sites. While the published work on IPA reveals that WO_x sites are active for the dehydration reaction, the single hydroxyl group of the IPA probe molecule limits the study of additional deoxygenation pathways. Herein,

TPD experiments identified three distinct sites for the reaction of glycerol: Pt sites for reforming, Brønsted acid WO_x sites for dehydration, and oxygen vacancy WO_x sites for hydrodeoxygenation (HDO). HREELS identified the surface intermediates for the reactions that occurred on each type of active site and showed that glycerol bonded via its oxygen atoms to WO_x-modified surfaces. The two types of W-O bonds detected likely resulted from the two different deoxygenation pathways observed in TPD experiments. This work represents the first surface science study that demonstrates the co-existence of two types of deoxygenation active sites on WO_x/Pt(111), and in turn guides the further design and improvement of relevant catalysts for the deoxygenation of BDOs.

Chapter 6 uses the same surface science approach that is used in Chapter 5 for the study of the ring-opening reaction of THFA on WO_x/Pt(111) surfaces. Using HREELS, the ring-opened intermediate from THFA was observed on Pt(111), as well as on WO_x-modified Pt(111). Interestingly, from TPD experiments, gas-phase 1,5-PeD only desorbed from WO_x-modified surfaces, whereas THFA decomposed to H_2 and CO on the Pt(111) surface. The combined HREELS and TPD results indicated that while THFA underwent the desired ring-opening reaction on Pt(111), the dioxy intermediate bonded too strongly to the surface which led to further decomposition. In contrast, the 1,5-pentanedioxy-like intermediate hydrogenated and desorbed as 1,5-PeD on near-monolayer (ML) and above-ML WO_x/Pt(111) surfaces, suggesting that WO_x modification weakened the interaction between the ring-opened intermediate and the surface to an extent that facilitated the desorption of the desired product. This strategy can be potentially extended to the design of catalysts for the selective ring-opening of other heterocyclic BDOs.

7.2 Future Directions

7.2.1 WN and NbN as Electrocatalysts for Other Reactions

As previously stated, pseudo-Pourbaix diagrams have been used to inform the stability of materials in pH-potential regimes relevant to specific electrochemical reactions. For example, one study found that the oxidation potential of TaC in acid and alkaline electrolyte was more positive than potentials relevant to alcohol oxidation (AO).[22] This suggested that TaC would likely be stable in conditions relevant to AO. A later study by different researchers in the same group used the pseudo-Pourbaix stability data of TaC as a platform to study Pt-modified TaC for the ethanol oxidation reaction (EOR) in both acid and alkaline electrolytes.[187] Pt/TaC was active and stable for the EOR, and was more resistant to poisoning by strongly bound reaction intermediates when compared to a Pt foil control.

The pseudo-Pourbaix diagrams presented in Chapter 3 offer a similar platform to guide the selection of electrochemical reactions with operating conditions relevant to WN and NbN. WN and NbN are stable in a wide pH window up to around 1.0 V_{RHE} and 0.6 V_{RHE}, respectively. While both materials should be stable in conditions relevant to several electroreduction reactions, such as the HER and the CO_2 reduction reaction (CO_2RR), WN should also be stable in conditions relevant to methanol and ethanol oxidation (0.5 V_{RHE} to 0.9 V_{RHE}). To this end, one study of Pd-modified WC reported a 0.2 V lower onset potential for ethanol oxidation than a Pd/C benchmark in alkaline electrolyte.[188] DFT calculations also indicated that EOR intermediates bound more weakly to Pd/WC(0001) compared to a Pd(111) control, which corelated to a reduction in active site poisoning over chronoamperometry (CA) experiments. In addition to the similar advantages that PGM-modified WN may have over benchmark materials, the inherently clean nitride surface should allow for better contact between the admetal and

substrate, and avoid the detrimental effects on activity that result from carbon overlayers on TMCs.[68]

Furthermore, pseudo-Pourbaix diagrams can be generated for other TMN materials to provide a basis from which TMN electrocatalysts can be screened for potential reactions. For example, one study found that Mo_2C-supported Pt electrocatalysts were highly active and stable for EOR.[189] Pseudo-Pourbaix information of Mo_2N could guide researchers for the rational use of the carbide analogue for similar electrochemical reactions that occur at relatively positive potentials.

7.2.2 Ongoing DFT Collaborations

There are currently ongoing collaborations for the work presented in Chapters 4 and 6, specifically for DFT calculations of reaction intermediate binding energies and activation energies. One ongoing collaboration with Prof. Nongnuch Artrith aims to extend a machine-learning model and first principles-calculations to predict activity and selectivity for ethanol reforming over Mo_2N and Pt/Mo_2N surfaces. This work builds on Prof. Artirith's previous work that used a series of machine-learning models, trained on reference data from DFT calculations to predict transition-state energies and activation energies, which were then input into a second model trained on published experimental activities and selectivities to predict reforming properties.[190] This model was developed for bimetallic metal catalysts, and the ongoing work is intended to extend these predictive models to the surfaces studied in Chapter 4.

The work presented in Chapter 6 is also being further investigated via DFT calculations. A past study of the ring-opening reaction of THFA and furfural on Ir(111) and Co/Ir(111) used DFT binding energy calculations to probe the interaction of the saturated and unsaturated furan ring with the surface, which helped to explain the formation of ring-opened intermediates.[185] A

separate study of IPA dehydration on WO_x/Pt(111) used DFT to calculate dehydration activation barriers on different in situ-formed hydroxy groups on WO_x to determine the most active sites.[49] A similar opportunity exists to use DFT calculations to further investigate the binding energies of reaction intermediates and identify distinct WO_x sites relevant to the work presented in Chapters 5 and 6.

References

1. Hagen, J. *Industrial Catalysis: A Practical Approach*. vol. Chapter 1 (Wiley-VCH Verlag GmbH & Co. KGaA, 2015).
2. International Energy Agency (IEA). *World Energy Outlook 2017*. *World Energy Outlook* (2017).
3. US Energy Information Administration (EIA). *International Energy Outlook 2017*. *International Energy Outlook* (2017).
4. Beiter, P., Elchinger, M. & Tian, T. 2016 Renewable Energy Data Book. 14–18 (2016).
5. Barnhart, C. J., Dale, M., Brandt, A. R. & Benson, S. M. The energetic implications of curtailing versus storing solar- and wind-generated electricity. *Energy and Environmental Science* **6**, 2804–2810 (2013).
6. Bird, L., Cochran, J. & Wang, X. *Wind and Solar Energy Curtailment: Experience and Practices in the United States*. *National Renewable Energy Laboratory (NREL)* (2014).
7. Godula-jopek, A. *Hydrogen Production: by Electrolysis*. (Wiley-VCH Verlag GmbH & Co. KGaA, 2015).
8. Pfromm, P. H. Towards sustainable agriculture: Fossil-free ammonia. *Journal of Renewable and Sustainable Energy* **9**, (2017).
9. Rafiqul, I., Weber, C., Lehmann, B. & Voss, A. Energy efficiency improvements in ammonia production - perspectives and uncertainties. *Energy* **30**, 2487–2504 (2005).
10. Tackett, B. M., Sheng, W. & Chen, J. G. Opportunities and Challenges in Utilizing Metal-Modified Transition Metal Carbides as Low-Cost Electrocatalysts. *Joule* **1**, 253–263 (2017).
11. Chen, J. G. *et al.* Beyond fossil fuel-driven nitrogen transformations. *Science* **360**, (2018).

12. Sheng, W. *et al.* Correlating hydrogen oxidation and evolution activity on platinum at different pH with measured hydrogen binding energy. *Nature Communications* **6**, (2015).

13. Subbaraman, R. *et al.* Enhancing Hydrogen Evolution Activity in Water Splitting by Tailoring Li^+-$Ni(OH)_2$-Pt Interfaces. *Science* **334**, 1256–1260 (2011).

14. Mahmood, N. *et al.* Electrocatalysts for Hydrogen Evolution in Alkaline Electrolytes: Mechanisms, Challenges, and Prospective Solutions. *Advanced Science* **5**, (2018).

15. Bockris, J. O. M., Ammar, I. A. & Huq, A. K. M. S. The mechanism of the hydrogen evolution reaction on platinum silver and tungsten surfaces in acid solutions. *Journal of Physical Chemistry* **61**, 879–886 (1957).

16. Vesborg, P. C. K., Seger, B. & Chorkendorff, I. Recent development in hydrogen evolution reaction catalysts and their practical implementation. *Journal of Physical Chemistry Letters* **6**, 951–957 (2015).

17. J. K. Nørskov, T. Bligaard, A. Logadottir, J. R. Kitchin, J. G. Chen, S. Pandelov, and U. S. Trends in the Exchange Current for Hydrogen Evolution. *Journal of The Electrochemical Society* **152**, 150–153 (2005).

18. McCrory, C. C. L. *et al.* Benchmarking Hydrogen Evolving Reaction and Oxygen Evolving Reaction Electrocatalysts for Solar Water Splitting Devices. *Journal of the American Chemical Society* **137**, 4347–4357 (2015).

19. U.S Geological Survey. *Mineral Commodity Summaries 2020*. *U.S Department of the Interior* (2020).

20. Masel, R. *Principles of Adsorption and Reaction on Solid Surfaces*. (John Wiley & Sons, Inc., 1996).

21. Zhang, Q. *et al.* Trends and Descriptors of Metal-Modified Transition Metal Carbides for Hydrogen Evolution in Alkaline Electrolyte. *ACS Catalysis* **9**, 2415–2422 (2019).

22. Kimmel, Y. C., Xu, X., Yu, W., Yang, X. & Chen, J. G. Trends in electrochemical stability of transition metal carbides and their potential use as supports for low-cost electrocatalysts. *ACS Catalysis* **4**, 1558–1562 (2014).

23. Weidman, M. C., Esposito, D. v., Hsu, Y. C. & Chen, J. G. Comparison of electrochemical stability of transition metal carbides (WC, W_2C, Mo_2C) over a wide pH range. *Journal of Power Sources* **202**, 11–17 (2012).

24. Weidman, M. C., Esposito, D. v, Hsu, I. J. & Chen, J. G. Electrochemical Stability of Tungsten and Tungsten Monocarbide (WC) Over Wide pH and Potential Ranges. *Journal of The Electrochemical Society* **157**, 179–188 (2010).

25. Division, E. S. P. *Energy balances in the production and end-use of alcohols derived from biomass*. (1980).

26. Council, N. R. *Review of the Research Strategy for Biomass-Derived Transportation Fuels*. *Review of the Research Strategy for Biomass-Derived Transportation Fuels* (1999).

27. Lee, U., Kwon, H., Wu, M. & Wang, M. Retrospective analysis of the U.S. corn ethanol industry for 2005–2019: implications for greenhouse gas emission reductions. *Biofuels, Bioproducts and Biorefining* **15**, 1318–1331 (2021).

28. Kim, Y. H., Jun, K. W., Joo, H., Han, C. & Song, I. K. A simulation study on gas-to-liquid (natural gas to Fischer-Tropsch synthetic fuel) process optimization. *Chemical Engineering Journal* **155**, 427–432 (2009).

29. Kim, J., Park, J., Qi, M., Lee, I. & Moon, I. Process Integration of an Autothermal Reforming Hydrogen Production System with Cryogenic Air Separation and Carbon

Dioxide Capture Using Liquefied Natural Gas Cold Energy. *Industrial and Engineering Chemistry Research* **60**, 7257–7274 (2021).

30. Siang, J. Y. *et al.* Hydrogen production from steam reforming of ethanol using a ceria-supported iridium catalyst: Effect of different ceria supports. *International Journal of Hydrogen Energy* **35**, 3456–3462 (2010).

31. Tosti, S. *et al.* Pd-based membrane reactors for producing ultra pure hydrogen: Oxidative reforming of bio-ethanol. *International Journal of Hydrogen Energy* **38**, 701–707 (2013).

32. Nozawa, T., Mizukoshi, Y., Yoshida, A. & Naito, S. Aqueous phase reforming of ethanol and acetic acid over TiO_2 supported Ru catalysts. *Applied Catalysis B: Environmental* **146**, 221–226 (2014).

33. Levy, R. B. & Boudart, M. Platinum-Like Behavior of Tungsten Carbide in Surface Catalysis. *Science* **181**, 547–549 (1973).

34. Hwu, H. H. & Chen, J. G. Surface Chemistry of Transition Metal Carbides. *Chemical Reviews* **105**, 185–212 (2005).

35. Esposito, D. v. *et al.* Low-cost hydrogen-evolution catalysts based on monolayer platinum on tungsten monocarbide substrates. *Angewandte Chemie - International Edition* **49**, 9859–9862 (2010).

36. Gouy-Pailler, Ph. & Pauleau, Y. Tungsten and tungsten–carbon thin films deposited by magnetron sputtering. *Journal of Vacuum Science & Technology A: Vacuum, Surfaces, and Films* **11**, 96–102 (1993).

37. Kelly, T. G. & Chen, J. G. Controlling C-O, C-C and C-H bond scission for deoxygenation, reforming, and dehydrogenation of ethanol using metal-modified molybdenum carbide surfaces. *Green Chemistry* **16**, 777–784 (2014).

38. Kelly, T. G., Ren, H. & Chen, J. G. Decomposition pathways of C2 oxygenates on Rh-modified tungsten carbide surfaces. *Surface Science* **640**, 89–95 (2015).

39. Ren, H., Hansgen, D. A., Stottlemyer, A. L., Kelly, T. G. & Chen, J. G. Replacing platinum with tungsten carbide (WC) for reforming reactions: Similarities in ethanol decomposition on Ni/Pt and Ni/WC surfaces. *ACS Catalysis* **1**, 390–398 (2011).

40. Okoye, P. U., Abdullah, A. Z. & Hameed, B. H. A review on recent developments and progress in the kinetics and deactivation of catalytic acetylation of glycerol—A byproduct of biodiesel. *Renewable and Sustainable Energy Reviews* **74**, 387–401 (2017).

41. Administration, U. S. E. I. *Monthly Biodiesel Production Report*. (2021).

42. Foo, G. S., Wei, D., Sholl, D. S. & Sievers, C. Role of Lewis and brønsted acid sites in the dehydration of glycerol over niobia. *ACS Catalysis* **4**, 3180–3192 (2014).

43. Robinson, A. M., Hensley, J. E., Medlin, J. W. & Will Medlin, J. Bifunctional Catalysts for Upgrading of Biomass-Derived Oxygenates: A Review. *ACS Catalysis* **6**, 5026–5043 (2016).

44. Wan, W. *et al.* Controlling reaction pathways of selective C-O bond cleavage of glycerol. *Nature Communications* **9**, 1–27 (2018).

45. Bac, S., Keskin, S. & Avci, A. K. Recent advances in sustainable syngas production by catalytic CO_2 reforming of ethanol and glycerol. *Sustainable Energy and Fuels* **4**, 1029–1047 (2020).

46. Zhou, W. *et al.* WOx domain size, acid properties and mechanistic aspects of glycerol hydrogenolysis over Pt/WOx/ZrO2. *Applied Catalysis B: Environmental* **242**, 410–421 (2019).

47. You, K. *et al.* Understanding the effect of Mo_2C support on the activity of Cu for the hydrodeoxygenation of glycerol. *Journal of Catalysis* **388**, 141–153 (2020).

48. Lei, N. *et al.* Effective Hydrogenolysis of Glycerol to 1,3-Propanediol over Metal-Acid Concerted $Pt/WO_x/Al_2O_3$ Catalysts. *ChemCatChem* **11**, 3903–3912 (2019).

49. Lin, Z. *et al.* Experimental and Theoretical Insights into the Active Sites on WOx/Pt(111) Surfaces for Dehydrogenation and Dehydration Reactions. *ACS Catalysis* 8023–8032 (2021).

50. Byun, J. & Han, J. An integrated strategy for catalytic co-production of jet fuel range alkenes, tetrahydrofurfuryl alcohol, and 1,2-pentanediol from lignocellulosic biomass. *Green Chemistry* **19**, 5214–5229 (2017).

51. Davis, R. *et al. Biochemical Conversion of Lignocellulosic Biomass to Hydrocarbon Fuels and Products: 2019 State of Technology and Future Research*. *NREL Technical Report* (2020).

52. Chheda, J. N., Huber, G. W. & Dumesic, J. A. Liquid-phase catalytic processing of biomass-derived oxygenated hydrocarbons to fuels and chemicals. *Angewandte Chemie International Edition* **46**, 7164–7183 (2007).

53. Chen, K., Mori, K., Watanabe, H., Nakagawa, Y. & Tomishige, K. C-O bond hydrogenolysis of cyclic ethers with OH groups over rhenium-modified supported iridium catalysts. *Journal of Catalysis* **294**, 171–183 (2012).

54. Koso, S. *et al.* Chemoselective hydrogenolysis of tetrahydrofurfuryl alcohol to 1,5-pentanediol. *Chemical Communications* 2035–2037 (2009) doi:10.1039/b822942b.

55. Lomelí-Rodríguez, M., Corpas-Martínez, J. R., Willis, S., Mulholland, R. & Lopez-Sanchez, J. A. Synthesis and characterization of renewable polyester coil coatings from

biomass-derived isosorbide, FDCA, 1,5-pentanediol, succinic acid, and 1,3-propanediol. *Polymers* **10**, 1–19 (2018).

56. *1,6-Hexanediol Market by Application (Polyurethanes, Coatings, Acrylates, Adhesives, Polyester Resins, and Plasticizers), and Region (Europe, APAC, North America, South America, and Middle East & Africa) - Global Forecast to 2025*. *Markets and Markets* (2019).

57. Wang, C. *et al.* A Study of Tetrahydrofurfuryl Alcohol to 1,5-Pentanediol Over Pt–WOx/C. *Catalysis Letters* **148**, 1047–1054 (2018).

58. Feng, S., Nagao, A., Aihara, T., Miura, H. & Shishido, T. Selective hydrogenolysis of tetrahydrofurfuryl alcohol on $Pt/WO_3/ZrO_2$ catalysts: Effect of WO_3 loading amount on activity. *Catalysis Today* **303**, 207–212 (2018).

59. Tomishige, K., Nakagawa, Y. & Tamura, M. Selective hydrogenolysis and hydrogenation using metal catalysts directly modified with metal oxide species. *Green Chemistry* **19**, 2876–2924 (2017).

60. Chen, J. G. Carbide and nitride overlayers on early transition metal surfaces: Preparation, characterization, and reactivities. *Chemical Reviews* **96**, 1477–1498 (1996).

61. Xiong, K., Yu, W. & Chen, J. G. Selective deoxygenation of aldehydes and alcohols on molybdenum carbide (Mo_2C) surfaces. *Applied Surface Science* **323**, 88–95 (2014).

62. Gleichweit, C. *et al.* Comparative study of the carbide-modified surfaces C/Mo(110) and C/Mo(100) using high-resolution x-ray photoelectron spectroscopy. *Physical Review B* **92**, 1–13 (2015).

63. Hwu, H. H., Chen, J. G., Kourtakis, K. & Lavin, J. G. Potential Application of Tungsten Carbides as Electrocatalysts. 1. Decomposition of Methanol over Carbide-Modified W(111). *Journal of Physical Chemistry B* **105**, 10037–10044 (2001).

64. Bachmann, M., Bikaljevic, D., Memmel, N. & Bertel, E. Adsorption and Reactions of Carbon Monoxide and Oxygen on Bare and Au-Decorated Carburized W(110). *Journal of Physical Chemistry C* **117**, 17024–17032 (2013).

65. Mirkarimi, P. B., Shinn, M. & Barnett, S. A. An ultrahigh vacuum, magnetron sputtering system for the growth and analysis of nitride superlattices. *Journal of Vacuum Science & Technology A: Vacuum, Surfaces, and Films* **10**, 75–81 (1992).

66. Xi, S., Lin, G., Jin, L., Li, H. & Xie, K. Metallic porous nitride single crystals at two-centimeter scale delivering enhanced pseudocapacitance. *Nature Communications* **10**, 1–9 (2019).

67. Ren, H., Chen, Y., Huang, Y., Deng, W. & Vlachos, G. Tungsten carbides as selective deoxygenation catalysts: experimental and computational studies of converting C3 oxygenates to propene. 761–769 (2014).

68. Kimmel, Y. C., Esposito, D. v., Birkmire, R. W. & Chen, J. G. Effect of surface carbon on the hydrogen evolution reactivity of tungsten carbide (WC) and Pt-modified WC electrocatalysts. *International Journal of Hydrogen Energy* **37**, 3019–3024 (2012).

69. Zhang, Q., Tackett, B. M., Wu, Q. & Chen, J. G. Trends in Hydrogen Evolution Activity of Metal-Modified Molybdenum Carbides in Alkaline and Acid Electrolytes. *ChemElectroChem* **3**, 1686–1693 (2016).

70. Denny, S. R., Tackett, B. M., Tian, D., Sasaki, K. & Chen, J. G. Exploring electrocatalytic stability and activity of unmodified and platinum-modified tungsten and niobium nitrides. *International Journal of Hydrogen Energy* **45**, 22883–22892 (2020).

71. Hübler, R. Transition metal nitrides thin films deposition using a dynamically controlled magnetron sputtering apparatus. *Surface and Coatings Technology* **158–159**, 680–684 (2002).

72. Wu, J. D., Wu, C. Z., Song, Z. M., Wu, L. H. & Li, F. M. Synthesis of molybdenum nitride γ-Mo_2N by multipulse laser irradiation of molybdenum in nitrogen. *Applied Surface Science* **90**, 81–87 (1995).

73. Wu, J. D., Wu, C. Z., Song, Z. M., Wu, L. H. & Li, F. M. Synthesis of molybdenum nitride γ-Mo_2N by multipulse laser irradiation of molybdenum in nitrogen. *Applied Surface Science* **90**, 81–87 (1995).

74. Decker, S., Löfberg, A., Bastin, J. M. & Frennet, A. Study of the preparation of bulk tungsten carbide catalysts with C_2H_6 /H_2 and C_2H_4/H_2 carburizing mixtures. *Catalysis Letters* **44**, 229–239 (1997).

75. Xiao, T., Wang, H., Da, J., Coleman, K. & Green, M. Study of the Preparation and Catalytic Performance of Molybdenum Carbide Catalysts Prepared with C_2H_2/H_2 Carburizing Mixture. *Journal of Catalysis* **211**, 183–191 (2002).

76. Xiao, T. C. *et al.* Preparation and characterisation of bimetallic cobalt and molybdenum carbides. *Journal of Catalysis* **202**, 100–109 (2001).

77. Xiao, T. C. *et al.* Preparation of molybdenum carbide-based catalysts for deep HDN. *Comptes Rendus de l'Academie des Sciences - Series IIc: Chemistry* **3**, 451–458 (2000).

78. Oyama, S. T. Preparation and Catalytic Properties of Transition Metal Carbides and Nitrides. *Catalysis Today* **15**, 179–200 (1992).

79. Decker, S., Lofberg, A., Bastin, J. & Frennet, A. Ã. Study of the preparation of bulk tungsten carbide catalysts with C_2H_6/H_2 and C_2H_4/H_2 carburizing mixtures. **44**, 229–239 (1997).

80. Volpe, L. E. O. & Boudart, M. Compounds of Molybdenum Surface Area and Tungsten with High Specific. **347**, 332–347 (1985).

81. Cairns, A. G. *et al.* The influence of precursor source and thermal parameters upon the formation of beta-phase molybdenum nitride. *Journal of Alloys and Compounds* **479**, 851–854 (2009).

82. Dongil, A. *et al.* Effect of Cu and Cs in the β-Mo_2C System for CO_2 Hydrogenation to Methanol. *Catalysts* **10**, 1–9 (2020).

83. Baddour, F. G. *et al.* An Exceptionally Mild and Scalable Solution-Phase Synthesis of Molybdenum Carbide Nanoparticles for Thermocatalytic CO_2 Hydrogenation. (2020).

84. Chen, Y., Choi, S. & Thompson, L. T. Low temperature CO_2 hydrogenation to alcohols and hydrocarbons over Mo_2C supported metal catalysts. *Journal of Catalysis* **343**, 147–156 (2016).

85. Porosoff, M. D., Baldwin, J. W., Peng, X., Mpourmpakis, G. & Willauer, H. D. Potassium-Promoted Molybdenum Carbide as a Highly Active and Selective Catalyst for CO_2 Conversion to CO. *ChemSusChem* **10**, 2408–2415 (2017).

86. Wang, H., Liu, S. & Smith, K. J. Understanding selectivity changes during hydrodesulfurization of dibenzothiophene on Mo_2C/carbon catalysts. *Journal of Catalysis* **369**, 427–439 (2019).

87. Diaz, B. *et al.* Hydrodesulfurization over supported monometallic, bimetallic and promoted carbide and nitride catalysts. *Catalysis Today* **86**, 191–209 (2003).

88. Ren, H. *et al.* Selective hydrodeoxygenation of biomass-derived oxygenates to unsaturated hydrocarbons using molybdenum carbide catalysts. *ChemSusChem* **6**, 798–801 (2013).

89. Dhandapani, B., st. Clair, T. & Oyama, S. T. Simultaneous hydrodesulfurization, hydrodeoxygenation, and hydrogenation with molybdenum carbide. *Applied Catalysis A: General* **168**, 219–228 (1998).

90. Tackett, B. M. *et al.* Reducing Iridium Loading in Oxygen Evolution Reaction Electrocatalysts Using Core-Shell Particles with Nitride Cores. *ACS Catalysis* **8**, 2615–2621 (2018).

91. Yao, S. *et al.* Exploring Metal − Support Interactions To Immobilize Subnanometer Co Clusters on γ − Mo_2N: A Highly Selective and Stable Catalyst for CO_2 Activation. (2019).

92. Bordet, A. *et al.* Magnetically Induced Continuous CO_2 Hydrogenation Using Composite Iron Carbide Nanoparticles of Exceptionally High Heating Power. *Angewandte Chemie - International Edition* **55**, 15894–15898 (2016).

93. Lu, Q. *et al.* Ordered Mesoporous Metal Carbides with Enhanced Anisole Hydrodeoxygenation Selectivity. (2016).

94. Cumpson, P. J. & Seah, M. P. Elastic scattering corrections in AES and XPS. II. Estimating attenuation lengths and conditions required for their valid use in overlayer/substrate experiments. *Surface and Interface Analysis* **25**, 430–446 (1997).

95. Moulder, J., Stickle, W., Sobol, P. & Bomben, K. *Handbook of X-ray Photoelectron Spectroscopy*. (Physical Electronics, Inc., 1995).

96. Ohring, M. *Materials Science of Thin Films: Deposition & Structure*. (Academic Press, 2001).

97. Wagner, C. D. *et al.* Empirical atomic sensitivity factors for quantitative analysis by electron spectroscopy for chemical analysis. *Surface and Interface Analysis* **3**, 211–225 (1981).

98. Colombi, P. *et al.* Glancing-incidence X-ray diffraction for depth profiling of polycrystalline layers. *Journal of Applied Crystallography* **39**, 176–179 (2006).

99. Bunaciu, A. A., Udriştioiu, E. gabriela & Aboul-Enein, H. Y. X-Ray Diffraction: Instrumentation and Applications. *Critical Reviews in Analytical Chemistry* **45**, 289–299 (2015).

100. Ibach, H. & Mills, D. L. *Energy Loss Spectroscopy and Surface Vibration*. (Academic Press, 1982).

101. Wang, J. *et al.* Enhancing Activity and Reducing Cost for Electrochemical Reduction of CO_2 by Supporting Palladium on Metal Carbides. *Angewandte Chemie - International Edition* **58**, 6271–6275 (2019).

102. Chen, Y., Zheng, Y., Yue, X. & Huang, S. Hydrogen evolution reaction in full pH range on nickel doped tungsten carbide nanocubes as efficient and durable non-precious metal electrocatalysts. *International Journal of Hydrogen Energy* **45**, 8695–8702 (2020).

103. Shakibi Nia, N. *et al.* W_2C-Supported PtAuSn - A Catalyst with the Earliest Ethanol Oxidation Onset Potential and the Highest Ethanol Conversion Efficiency to CO_2 Known till Date. *ACS Catalysis* **10**, 1113–1122 (2020).

104. Li, T. *et al.* Palladium nanoparticles grown on β-Mo_2C nanotubes as dual functional electrocatalysts for both oxygen reduction reaction and hydrogen evolution reaction. *International Journal of Hydrogen Energy* **43**, 4932–4941 (2018).

105. Zhang, S. *et al.* Highly graphitic carbon shell on molybdenum carbide nanosheets by iron doping for stable hydrogen evolution. *International Journal of Hydrogen Energy* **45**, 14368–14374 (2020).

106. Garg, A. *et al.* Impact of Transition Metal Carbide and Nitride Supports on the Electronic Structure of Thin Platinum Overlayers. *ACS Catalysis* **9**, 7090–7098 (2019).

107. Byun, J., Ahn, S. H. & Kim, J. J. Self-terminated electrodeposition of platinum on titanium nitride for methanol oxidation reaction in acidic electrolyte. *International Journal of Hydrogen Energy* **45**, 9603–9611 (2020).

108. Craig, J. *In Practical Surface Analysis, Auger and X-Ray Photoelectron Spectroscopy*. (Elsevier, 1991).

109. Hohenberg, P. & Kohn, W. Inhomogeneous Electron Gas. *Physical Review* **136**, B864–B871 (1964).

110. Kohn, W. & Sham, L. J. Self-Consistent Equations Including Exchange and Correlation Effects. *Physical Review* **140**, 289–295 (1965).

111. Blöchl, P. E. Projector augmented-wave method. *Physical Review B* **50**, 17953–17979 (1994).

112. Perdew, J. P. *et al.* Atoms, molecules, solids, and surfaces: Applications of the generalized gradient approximation for exchange and correlation. *Physical Review B* **48**, 4978 (1993).

113. Kresse, G. & Furthmüller, J. Efficiency of ab-initio total energy calculations for metals and semiconductors using a plane-wave basis set. *Computational Materials Science* **6**, 15–50 (1996).

114. Kresse, G. & Hafner, J. Ab initio molecular dynamics for open-shell transition metals. *Physical Review B* **48**, 13115–13118 (1993).

115. Nørskov, J. K. *et al.* Origin of the overpotential for oxygen reduction at a fuel-cell cathode. *Journal of Physical Chemistry B* **108**, 17886–17892 (2004).

116. Sheng, W. *et al.* Electrochemical reduction of CO_2 to synthesis gas with controlled CO/H_2 ratios. *Energy Environ. Sci.* **10**, 1180–1185 (2017).

117. Harnisch, F., Schroder, U., Quaas, M. & Scholz, F. Electrocatalytic and corrosion behaviour of tungsten carbide in near-neutral pH electrolytes. *Applied Catalysis B: Environmental* **87**, 63–69 (2009).

118. Andersson, K. M. & Bergström, L. Oxidation and dissolution of tungsten carbide powder in water. *International Journal of Refractory Metals and Hard Materials* **18**, 121–129 (2000).

119. Ortiz, P. I., Giordano, M. C. & Teijelo, M. L. Electrochemical behaviour of tungsten in alkaline media. Part II. Sodium carbonate solutions. *Journal of Electroanalytical Chemistry* **251**, 379–391 (1988).

120. Sheng, W., Gasteiger, H. A. & Shao-Horn, Y. Hydrogen Oxidation and Evolution Reaction Kinetics on Platinum: Acid vs Alkaline Electrolytes. *Journal of The Electrochemical Society* **157**, B1529 (2010).

121. Houtman, C. J. & Barteau, M. A. Divergent pathways of acetaldehyde and ethanol decarbonylation on the Rh(111) surface. *Journal of Catalysis* **130**, 528–546 (1991).

122. Davis, J. L. & Barteau, M. A. Decarbonylation and decomposition pathways of alcohol's on Pd(111). *Surface Science* **187**, 387–406 (1987).

123. Shekhar, R. & Barteau, M. A. Structure sensitivity of alcohol reactions on (110) and (111) palladium surfaces. *Catalysis Letters* **31**, 221–237 (1995).

124. Skoplyak, O., Barteau, M. A. & Chen, J. G. Reforming of oxygenates for H_2 production: Correlating reactivity of ethylene glycol and ethanol on Pt(111) and Ni/Pt(111) with surface d-band center. *Journal of Physical Chemistry B* **110**, 1686–1694 (2006).

125. Skoplyak, O., Barteau, M. A. & Chen, J. G. Ethanol and ethylene glycol on Ni/Pt(111) bimetallic surfaces: A DFT and HREELS study. *Surface Science* **602**, 3578–3587 (2008).

126. Lee, A. F., Gawthrope, D. E., Hart, N. J. & Wilson, K. A Fast XPS study of the surface chemistry of ethanol over Pt(111). *Surface Science* **548**, 200–208 (2004).

127. Sexton, B. A., Rendulic, K. D. & Huges, A. E. Decomposition pathways of C1-C4 alcohols adsorbed on platinum (111). *Surface Science* **121**, 181–198 (1982).

128. Kelly, T. G., Stottlemyer, A. L., Yang, X. & Chen, J. G. Theoretical and Experimental Studies of Ethanol Decomposition and Electrooxidation over Pt-Modified Tungsten Carbide. *Journal of the Electrochemical Society* **161**, E3165–E3170 (2014).

129. Bullock, R. M. *et al.* Using nature's blueprint to expand catalysis with Earth-abundant metals. *Science* **369**, (2020).

130. Esposito, D. v. & Chen, J. G. Monolayer platinum supported on tungsten carbides as low-cost electrocatalysts: Opportunities and limitations. *Energy and Environmental Science* (2011).

131. Johansson, L. I. Electronic and structural properties of transition-metal carbide and nitride surfaces. *Surface Science Reports* **21**, 177–250 (1995).

132. Setthapun, W., Bej, S. K. & Thompson, L. T. Carbide and nitride supported methanol steam reforming catalysts: Parallel synthesis and high throughput screening. *Topics in Catalysis* **49**, 73–80 (2008).

133. Eklund, P., Kerdsongpanya, S. & Alling, B. Transition-metal-nitride-based thin films as novel energy harvesting materials. *Journal of Materials Chemistry C* **4**, 3905–3914 (2016).

134. Liu, F., Dang, D. & Tian, X. Platinum-decorated three dimensional titanium copper nitride architectures with durable methanol oxidation reaction activity. *International Journal of Hydrogen Energy* **44**, 8415–8424 (2019).

135. Yang, X. *et al.* Mechanistic Insights into Electrochemical Nitrogen Reduction Reaction on Vanadium Nitride Nanoparticles. *Journal of the American Chemical Society* **140**, 13387–13391 (2018).

136. Chen, W. F. *et al.* Hydrogen-evolution catalysts based on non-noble metal nickel-molybdenum nitride nanosheets. *Angewandte Chemie - International Edition* **51**, 6131–6135 (2012).

137. Cao, B., Veith, G. M., Neuefeind, J. C., Adzic, R. R. & Khalifah, P. G. Mixed close-packed cobalt molybdenum nitrides as non-noble metal electrocatalysts for the hydrogen evolution reaction. *Journal of the American Chemical Society* **135**, 19186–19192 (2013).

138. Wyvratt, B. M. *et al.* Reactivity of Hydrogen on and in Nanostructured Molybdenum Nitride: Crotonaldehyde Hydrogenation. *ACS Catalysis* **6**, 5797–5806 (2016).

139. Lin, Z. *et al.* Unraveling unique surface chemistry of metal nitrides in controlling selective C-O bond scission pathways of glycerol. *In Preparation*.

140. Chen, J. G., Menning, C. A. & Zellner, M. B. Monolayer bimetallic surfaces: Experimental and theoretical studies of trends in electronic and chemical properties. *Surface Science Reports* **63**, 201–254 (2008).

141. Hwu, H. H. & Chen, J. G. Substrate-Dependent Reaction Pathways of Ethylene on Clean and Carbide-Modified W(110) and W(111). *The Journal of Physical Chemistry B* **107**, 11467–11474 (2003).

142. Wan, W. *et al.* Controlling reaction pathways of selective C–O bond cleavage of glycerol. *Nature Communications* **9**, 1–10 (2018).

143. Barnes, A. J., Evans, M. L. & Hallam, H. E. Infrared cryogenic studies. *Journal of Molecular Structure* **99**, 235–245 (1983).

144. Ruddy, D. A. *et al.* Recent advances in heterogeneous catalysts for bio-oil upgrading via "ex situ catalytic fast pyrolysis": Catalyst development through the study of model compounds. *Green Chemistry* **16**, 454–490 (2014).

145. Li, X., Jia, P. & Wang, T. Furfural: A Promising Platform Compound for Sustainable Production of C4 and C5 Chemicals. *ACS Catalysis* **6**, 7621–7640 (2016).

146. Xiong, K., Yu, W., Vlachos, D. G. & Chen, J. G. Reaction Pathways of Biomass-Derived Oxygenates over Metals and Carbides: From Model Surfaces to Supported Catalysts. 1402–1421 (2015) doi:10.1002/cctc.201403067.

147. Dodekatos, G., Schünemann, S. & Tüysüz, H. Recent Advances in Thermo-, Photo-, and Electrocatalytic Glycerol Oxidation. *ACS Catalysis* **8**, 6301–6333 (2018).

148. Lin, Z., Chen, R., Qu, Z. & Chen, J. G. Hydrodeoxygenation of biomass-derived oxygenates over metal carbides: From model surfaces to powder catalysts. *Green Chemistry* **20**, 2679–2696 (2018).

149. Motagamwala, A. H. *et al.* Toward biomass-derived renewable plastics: Production of 2,5-furandicarboxylic acid from fructose. *Science Advances* **4**, 1–9 (2018).

150. Xing, R., Qi, W. & Huber, G. W. Production of furfural and carboxylic acids from waste aqueous hemicellulose solutions from the pulp and paper and cellulosic ethanol industries. *Energy and Environmental Science* **4**, 2193–2205 (2011).

151. Davda, R. R., Shabaker, J. W., Huber, G. W., Cortright, R. D. & Dumesic, J. A. A review of catalytic issues and process conditions for renewable hydrogen and alkanes by aqueous-phase reforming of oxygenated hydrocarbons over supported metal catalysts. *Applied Catalysis B: Environmental* **56**, 171–186 (2005).

152. Gosselink, R. W., Stellwagen, D. R. & Bitter, J. H. Tungsten-based catalysts for selective deoxygenation. *Angewandte Chemie - International Edition* **52**, 5089–5092 (2013).

153. Kostestkyy, P., Yu, J., Gorte, R. J. & Mpourmpakis, G. Structure-activity relationships on metal-oxides: Alcohol dehydration. *Catalysis Science and Technology* **4**, 3861–3869 (2014).

154. Raju, S., Moret, M. E. & Klein Gebbink, R. J. M. Rhenium-Catalyzed Dehydration and Deoxydehydration of Alcohols and Polyols: Opportunities for the Formation of Olefins from Biomass. *ACS Catalysis* **5**, 281–300 (2015).

155. Zhong, J., Guo, Y. & Chen, J. Protonated and layered transition metal oxides as solid acids for dehydration of biomass-based fructose into 5-hydroxymethylfurfural. *Journal of Energy Chemistry* **26**, 147–154 (2017).

156. Yu, W., Xiong, K., Ji, N., Porosoff, M. D. & Chen, J. G. Theoretical and experimental studies of the adsorption geometry and reaction pathways of furfural over FeNi bimetallic model surfaces and supported catalysts. *Journal of Catalysis* **317**, 253–262 (2014).

157. Jiang, Z., Wan, W., Lin, Z., Xie, J. & Chen, J. G. Understanding the Role of M/Pt(111) (M = Fe, Co, Ni, Cu) Bimetallic Surfaces for Selective Hydrodeoxygenation of Furfural. *ACS Catalysis* **7**, 5758–5765 (2017).

158. Luo, J. *et al.* Base metal-Pt alloys: A general route to high selectivity and stability in the production of biofuels from HMF. *Applied Catalysis B: Environmental* **199**, 439–446 (2016).

159. Luo, J. *et al.* Mechanisms for High Selectivity in the Hydrodeoxygenation of 5-Hydroxymethylfurfural over PtCo Nanocrystals. *ACS Catalysis* **6**, 4095–4104 (2016).

160. Lin, Z., Wan, W., Yao, S. & Chen, J. G. Cobalt-modified molybdenum carbide as a selective catalyst for hydrodeoxygenation of furfural. *Applied Catalysis B: Environmental* **233**, 160–166 (2018).

161. Wang, C. *et al.* Mechanistic Study of the Direct Hydrodeoxygenation of m-Cresol over WOx-Decorated Pt/C Catalysts. *ACS Catalysis* **8**, 7749–7759 (2018).

162. Zhu, S., Gao, X., Zhu, Y. & Li, Y. Promoting effect of WOx on selective hydrogenolysis of glycerol to 1,3-propanediol over bifunctional Pt-WOx/Al_2O_3 catalysts. *Journal of Molecular Catalysis A: Chemical* **398**, 391–398 (2015).

163. Zhu, S. *et al.* SiO_2 promoted Pt/WOx/ZrO_2 catalysts for the selective hydrogenolysis of glycerol to 1,3-propanediol. *Applied Catalysis B: Environmental* **158–159**, 391–399 (2014).

164. García-Fernández, S. *et al.* New approaches to the Pt/WOx/Al_2O_3 catalytic system behavior for the selective glycerol hydrogenolysis to 1,3-propanediol. *Journal of Catalysis* **323**, 65–75 (2015).

165. Zhou, W. *et al.* Insight into the nature of Brönsted acidity of Pt-$(WO_x)_n$-H model catalysts in glycerol hydrogenolysis. *Journal of Catalysis* **388**, 154–163 (2020).

166. Zhou, W., Zhao, Y., Wang, Y., Wang, S. & Ma, X. Glycerol Hydrogenolysis to 1,3-Propanediol on Tungstate/Zirconia-Supported Platinum: Hydrogen Spillover Facilitated by Pt(111) Formation. *ChemCatChem* **8**, 3663–3671 (2016).

167. Zhao, X. *et al.* Selective Hydrogenolysis of Glycerol to 1,3-Propanediol: Manipulating the Frustrated Lewis Pairs by Introducing Gold to Pt/WOx. *ChemSusChem* **10**, 819–824 (2017).

168. Wang, J. *et al.* Hydrogenolysis of Glycerol to 1,3-propanediol under Low Hydrogen Pressure over WOx-Supported Single/Pseudo-Single Atom Pt Catalyst. *ChemSusChem* **9**, 784–790 (2016).

169. Chen, T. & Vohs, J. M. Active sites for the selective hydrodeoxygenation of m-cresol on WOx-modified Pt. *Surface Science* **689**, 121457 (2019).

170. Chu, S. & Majumdar, A. Opportunities and challenges for a sustainable energy future. *Nature* **488**, 294–303 (2012).

171. Biddy, M. J., Scarlata, C. J. & Kinchin, C. M. *Chemicals from biomass: A market assessment of bioproducts with near-term potential*. *NREL Technical Report* (2016).

172. Lin, L., Cunshan, Z., Vittayapadung, S., Xiangqian, S. & Mingdong, D. Opportunities and challenges for biodiesel fuel. *Applied Energy* **88**, 1020–1031 (2011).

173. Huber, G. W., Iborra, S. & Corma, A. Synthesis of Transportation Fuels from Biomass: Chemistry, Catalysts, and Engineering. *Chemical Reviews* **106**, 4044–4098 (2006).

174. McCormick, R. L. *et al.* Properties of oxygenates found in upgraded biomass pyrolysis oil as components of spark and compression ignition engine fuels. *Energy and Fuels* **29**, 2453–2461 (2015).

175. Wilson, A. N. *et al.* Valorization of aqueous waste streams from thermochemical biorefineries. *Green Chemistry* **21**, 4217–4230 (2019).

176. Kim, S. *et al.* Recent advances in hydrodeoxygenation of biomass-derived oxygenates over heterogeneous catalysts. *Green Chemistry* **21**, 3715–3743 (2019).

177. Huang, K. *et al.* Conversion of Furfural to 1,5-Pentanediol: Process Synthesis and Analysis. *ACS Sustainable Chemistry and Engineering* **5**, 4699–4706 (2017).

178. Koso, S. *et al.* Chemoselective hydrogenolysis of tetrahydrofurfuryl alcohol to 1,5-pentanediol. *Chemical Communications* 2035–2037 (2009).

179. Brentzel, Z. J. *et al.* Chemicals from Biomass: Combining Ring-Opening Tautomerization and Hydrogenation Reactions to Produce 1,5-Pentanediol from Furfural. *ChemSusChem* **10**, 1351–1355 (2017).

180. Koso, S., Nakagawa, Y. & Tomishige, K. Mechanism of the hydrogenolysis of ethers over silica-supported rhodium catalyst modified with rhenium oxide. *Journal of Catalysis* **280**, 221–229 (2011).

181. Koso, S. *et al.* Promoting effect of Mo on the hydrogenolysis of tetrahydrofurfuryl alcohol. *Journal of Catalysis* **267**, 89–92 (2009).

182. Liu, L., Asano, T., Nakagawa, Y., Tamura, M. & Tomishige, K. One-pot synthesis of 1,3-butanediol by 1,4-anhydroerythritol hydrogenolysis over a tungsten-modified platinum on silica catalyst. *Green Chemistry* **22**, 2375–2380 (2020).

183. Chia, M. *et al.* Selective hydrogenolysis of polyols and cyclic ethers over bifunctional surface sites on rhodium-rhenium catalysts. *Journal of the American Chemical Society* **133**, 12675–12689 (2011).

184. Soghrati, E. *et al.* C-O Hydrogenolysis of Tetrahydrofurfuryl Alcohol to Catalysts. *ChemCatChem* **10**, 4652–4664 (2018).

185. Wan, W., Jenness, G. R., Xiong, K., Vlachos, D. G. & Chen, J. G. Ring-Opening Reaction of Furfural and Tetrahydrofurfuryl Alcohol on Hydrogen-Predosed Iridium(111) and Cobalt/ Iridium(111) Surfaces. **9**, 1701–1707 (2017).

186. Lin, Z., Wan, W. & Chen, J. G. 1,2-Propanediol as a Surrogate Molecule of Glycerol for Mechanistic Studies of Selective Hydrodeoxygenation Reactions over Mo_2C and Cu/Mo_2C Surfaces. *ACS Sustainable Chemistry and Engineering* **7**, 8077–8082 (2019).

187. Jiang, Z., Zhang, Q., Liang, Z. & Chen, J. G. Pt-modified TaC as an efficient electrocatalyst for ethanol oxidation in acid and alkaline electrolytes. *Applied Catalysis B: Environmental* **234**, 329–336 (2018).

188. Zhang, Q. *et al.* Palladium-Modified Tungsten Carbide for Ethanol Electrooxidation: From Surface Science Studies to Electrochemical Evaluation. *Journal of The Electrochemical Society* **165**, J3031–J3038 (2018).

189. Lin, L., Sheng, W., Yao, S., Ma, D. & Chen, J. G. Pt/Mo_2C/C-cp as a highly active and stable catalyst for ethanol electrooxidation. *Journal of Power Sources* **345**, 182–189 (2017).

190. Artrith, N., Lin, Z. & Chen, J. G. Predicting the activity and selectivity of bimetallic metal catalysts for ethanol reforming using machine learning. *ACS Catalysis* **10**, 9438–9444 (2020).